FEDERAL UNIVERSITY OF SANTA CATARINA
SCHOOL OF TECHNOLOGY
MATERIALS SCIENCE AND ENGINEERING GRADUATE PROGRAM

Marcelo Demetrio de Magalhães

On the quantification of CMCs damage mechanisms by acoustic emission and machine learning

Florianópolis
2022

Marcelo Demetrio de Magalhães

On the quantification of CMCs damage mechanisms by acoustic emission and machine learning

Thesis presented to the Materials Science and Engineering Graduate Program of the Federal University of Santa Catarina to obtain the Master of Science degree in Materials Science and Engineering.
Supervisor: Márcio Celso Fredel, Prof. Dr.-Ing.
Co-supervisor: Renato Saint Martin Almeida, Dr.-Ing.

Florianópolis
2022

Ficha de identificação da obra elaborada pelo autor,
através do Programa de Geração automática da Biblioteca Universitária da UFSC.

de Magalhães, Marcelo Demetrio
On the quantification of CMCs damage mechanisms by acoustic emission and machine learning / Marcelo Demetrio de Magalhães ; orientador, Márcio Celso Fredel, coorientador, Renato Saint Martin Almeida, 2022.
123 p.

Dissertação (mestrado) - Universidade Federal de Santa Catarina, Centro Tecnológico, Programa de Pós-Graduação em Ciência e Engenharia de Materiais, Florianópolis, 2022.

Inclui referências.

1. Ciência e Engenharia de Materiais. 2. Compósitos de Matriz Cerâmica. 3. Mecanismos de Tenacificação. 4. Emissão Acústica. 5. Aprendizagem de Máquina. I. Fredel, Márcio Celso. II. Almeida, Renato Saint Martin. III. Universidade Federal de Santa Catarina. Programa de Pós Graduação em Ciência e Engenharia de Materiais. IV. Título.

Marcelo Demetrio de Magalhães

On the quantification of CMCs damage mechanisms by acoustic emission and machine learning

This Master's Degree thesis was evaluated and approved by the examining board, here composed of:

Prof. Márcio Celso Fredel, Dr.
EMC/UFSC (president)

Prof. Dachamir Hotza, Dr.
EQA/UFSC

Prof. Leandro Neckel, Dr.
UNESC (external member)

We certify that this is the original and final version of this thesis, which was deemed adequate for the obtaining of the degree of Master of Science in Materials Science and Engineering.

Documento assinado digitalmente
Joao Batista Rodrigues Neto
Data: 23/02/2022 10:45:35-0300
CPF: 645.810.989-04
Verifique as assinaturas em https://v.ufsc.br

Prof. João Batista Rodrigues Neto, Dr.
PGMAT/UFSC (coordinator)

Documento assinado digitalmente
Marcio Celso Fredel
Data: 23/02/2022 11:02:23-0300
CPF: 466.706.459-53
Verifique as assinaturas em https://v.ufsc.br

Prof. Márcio Celso Fredel, Dr.
PGMAT/UFSC (supervisor)

Florianópolis, 2022.

Dedicated to my grandfather Natalino Leal Demetrio, for his life teachings, and for being the kind of person I look forward to being in the future.

ACKNOWLEDGEMENTS

My first and utmost thanks goes to my father, mother, and brother, who were always there for me, even in my most selfish moments.

To the Federal University of Santa Catarina, and its Graduation Program of Materials Science and Engineering for the opportunity. Specially Rogério Campos, for his helpfulness and support to the students.

To the Advanced Ceramics Group at Universität Bremen, particularly to professor Kurosch Rezwan, responsible for the Advanced Ceramics Group, and Kamen Tushtev, leader of the CMC group, who assisted to continue this project.

To professor Márcio Celso Fredel for accepting to be my supervisor and supporting this master's research.

To Renato Saint Martin Almeida, for advising and aiding with data analysis; for the friendship; and for answering my many e-mails, long video calls, and even longer phone audio messages.

To my professors involved in this project and that bought the idea, and have ever since been helping to envision the next steps in this adventure.

To my friends, who even during the pandemic managed to keep contact, hearing my joys, grumblings, and general life updates.

Finally, my sincere thanks to everyone who heard me talk excitedly about this project, and has helped me in any way, shape, or form since this academic journey started. As the motto from a great friend says, "*confia!*".

“I always do that, get into something and see how far I can go.”

(Richard P. Feynman)

RESUMO

Compósitos de matriz cerâmica (CMCs) destacam-se devido a sua baixa densidade e marcantes propriedades mecânicas. Os constituintes que os formam podem ser todos não óxidos (NOx-CMCs), todos óxidos (Ox-CMCs) ou uma mistura de ambos. Em geral, o primeiro apresenta propriedades mecânicas mais desejáveis, enquanto o segundo se destaca em ambientes agressivos devido à sua resistência à oxidação. Uma mistura pode ser usada dependendo das condições de aplicação. Esses materiais são reconhecidos por não apresentarem comportamento frágil, mas *quasi*-dúctil. A tolerância a danos dos CMCs é possível devido a vários mecanismos de deflexão de trincas, como: trincamento (*matrix cracking*), desplacamento (*interface debonding*) e arrancamento (*pull-out*). Portanto, entender como esses mecanismos de tenacificação funcionam é crucial para o desenvolvimento posterior desses compósitos. Neste trabalho, testes mecânicos em conjunto com monitoramento por emissões acústicas (AE) foram realizados para estudar o desenvolvimento de danos durante o carregamento de CMCs. Testes mecânicos específicos forneceram meios para simular os mecanismos de tenacificação. Os sinais de AE foram relacionados a cada mecanismo e usados para obter um conjunto de dados de treinamento, utilizado para criar um modelo de aprendizado de máquina supervisionado. O modelo foi então usado para classificar sinais de AE medidos durante o carregamento de compósitos de matriz de carbeto de silício reforçada com fibras de carbono, e matriz de alumina reforçada com fibras de alumina (C_f/SiC e Al_2O_{3f}/Al_2O_3 respectivamente). Os resultados obtidos mostraram que o modelo pode ser aplicado com sucesso para identificar os mecanismos de tenacificação. A quantidade de mecanismos acionados, e energia dissipada por eles durante o carregamento mecânico é representada em percentuais totais de ocorrência.

Amostras de placas compósitas de C_f/SiC foram previamente fadigadas, e as mudanças promovidas pelos ciclos de fadiga puderam ser avaliadas. Os ciclos de fadiga promoveram um aumento de eventos de arrancamento, desplacamento, e ruptura de fibras (*fiber break*). Amostras de minicompósitos e placas compósitas de Al_2O_{3f}/Al_2O_3 apresentaram desenvolvimento de falha distinto. Em geral, minicompósitos apresentaram a maior parte de sua energia dissipada pela ruptura de fibras (~86%), enquanto as placas compósitas apresentaram a maior parte de sua energia dissipada pelos mecanismos de deflexão (~57%).

Palavras-Chave: compósitos de matriz cerâmica; mecanismos de tenacificação; emissão acústica; aprendizagem de máquina.

RESUMO EXPANDIDO

Introdução

A procura de materiais tolerantes a danos ganha cada vez mais atenção para aplicações estruturais nos últimos anos. Em específico, componentes leves e resistência à oxidação, aliados à elevadas propriedades mecânicas são de grande interesse para essas aplicações. Compósitos de matriz cerâmica (CMC) são fortes candidatos para suprir estas necessidades. A capacidade de obter estruturas com configurações distintas (com fibras longas/curtas, alteração na orientação das fibras, e ordem de empilhamento das camadas) permite o desenvolvimento de compósitos para uma várias funções, inclusive na indústria aeroespacial. Além disso, esses compósitos possuem a vantagem de combinar propriedades de cerâmicas monolíticas, com um comportamento *quasi*-dúctil.

A tolerância a danos pode ser obtida através da atividade de múltiplos mecanismos de tenacificação, como trincamento (*matrix cracking*), desplacamento (*interface debonding*) e arrancamento (*pull-out*). Esses mecanismos dissipam a energia de propagação de trincas nucleadas durante um carregamento mecânico. Assim, um comportamento *quasi*-dúctil pode ser alcançado. Entretanto, a compreensão desses mecanismos é complexa, e outros eventos também podem ser promovidos, como a ruptura da fibra (*fiber break*) e fricção das interfaces (*friction*). A atividade dos mecanismos pode ser avaliada por meio de análises de imagem, como microscopia eletrônica de varredura (MEV), e tomografia computadorizada (CT). Todavia, essas análises não permitem avaliar quando os danos são gerados na estrutura do compósito. Outra análise que ganhou destaque nos últimos anos é o monitoramento por emissão acústica (AE). A técnica de AE permite a análise do desenvolvimento dos danos por meio da medição de sinais de onda, mensurados por sensores a partir da vibração que os danos na estrutura do compósito promovem. Os dados mensurados podem ser relacionados com o tipo de mecanismo promovido. No entanto, ainda é complexo discriminar entre cada mecanismo apenas por estes dados. Para ajudar nesta tarefa, podem ser utilizados algoritmos de aprendizagem de máquina, tais como a aprendizagem supervisionada, para dar uma visão simples e automatizada do desempenho do material.

Para realizar isso, o monitoramento por AE pode ser utilizado para mensurar os dados referentes a cada mecanismo de tenacificação, e obter um conjunto de dados de treinamento. Esse conjunto de dados pode ser aplicado em um algoritmo de aprendizagem de máquina, adquirindo um modelo capaz de fazer novas classificações a partir da informação previamente conhecida. Dessa maneira é possível inserir novos dados de AE neste modelo, e obter a classificação desses dados.

Logo, este trabalho visa avaliar a evolução dos danos em CMCs, combinando o monitoramento por AE com uma abordagem de aprendizagem supervisionada. Ensaios mecânicos específicos em conjunto com AE foram conduzidos em amostras designadas como pré-testes, de maneira a adquirir dados que representassem cada mecanismo de tenacificação. Esses dados foram utilizados para criar um conjunto de dados de treinamento, aplicado para ensinar um algoritmo supervisionado (algoritmo k-nearest neighbor, KNN) e obter o modelo supervisionado de aprendizagem de máquina. O modelo foi usado para classificar sinais de AE medidos durante ensaios mecânicos de tração e flexão de compósitos de matriz de carbeto de silício reforçada com fibras de carbono, e matriz de alumina reforçada com fibras de alumina (C_f/SiC e Al_2O_{3f}/Al_2O_3 respectivamente).

Objetivos

O principal objetivo deste trabalho é quantificar os mecanismos de tenacificação em CMCs que ocorrem durante o carregamento mecânico. Para atingir este objetivo, três objetivos específicos

devem ser atingidos: (1) Analisar cada mecanismo separadamente, de maneira a obter os dados experimentais através do monitoramento por AE combinados a ensaios mecânicos distintos. Espera-se que cada ensaio mecânico promova sinais relacionados a ruptura da fibra, trincamento da matriz, ou mecanismos interfaciais (desplacamento ou arrancamento); (2) criar um modelo de aprendizagem de máquina supervisionado utilizando os dados de AE respectivos de cada mecanismo como uma base de dados de treinamento; (3) utilizar o modelo para classificar os sinais de AE quanto a um dos tipos de mecanismo, realizando a quantificação e avaliação do desenvolvimento do dano.

Metodologia

Ensaios mecânicos em amostras designadas como pré-testes foram conduzidos em conjunto com monitoramento por AE, como meio de obter a base de dados de treinamento a ser aplicada no modelo supervisionado. Para isso, corpos de prova foram preparados a partir de fibras de Al_2O_3 Nextel 610, e matrizes de Al_2O_3 (obtidas por gelificação ionotrópica). Os seguintes corpos de prova foram preparados: filamentos de fibra (1-filamento, 10-filamentos, e 750-filamentos); matrizes (com e sem entalhe); arrancamento de fibra; e placas compósitas. Os corpos de prova foram submetidos respectivamente aos seguintes ensaios mecânicos, onde é destacado o tipo de informação (mensurada por AE) ao qual esperava-se adquirir: ensaio de tração (ruptura de fibra, fricção); ensaio de flexão a 3 e 4 pontos (trincamento); ensaio de tração (arrancamento); e ensaio de cisalhamento de feixe curto (desplacamento).

Em seguida, ensaios mecânicos em amostras designadas como testes finais foram conduzidos para coletar os sinais de AE a serem utilizados para avaliar a performance do modelo supervisionado, i.e. realizar a classificação e quantificação desses sinais. Para isso, foram preparados compósitos de Al_2O_{3f}/Al_2O_3 a partir dos mesmos constituintes das amostras de pré-testes. Dois tipos de compósitos foram preparados: minicompósitos (compósitos com fibras unidirecionais), e placas compósitas (compósitos com orientação das fibras em 0/90º). O primeiro foi ensaiado em tração, enquanto o segundo foi ensaiado em flexão a 4 pontos. Em adição a isso, sinais de AE de compósitos em 2.5 dimensões (2.5D) de C_f/SiC, preparados em um trabalho prévio (Almeida et al, 2019b) a partir de uma pré-forma com fibras de carbono T700G com orientação em 0/90º, e fibras curtas na direção da altura também foram utilizados no modelo supervisionado.

Para criar o modelo de aprendizagem de máquina supervisionado, os sinais de AE medidos a partir dos pré-testes foram rotulados de acordo com os respectivos tipos de dano e dispostos em um arquivo .csv. Para criar o modelo de classificação, primeiro é necessário selecionar os descritores, e o algoritmo. Para selecionar os descritores (identificadores responsáveis por distinguir os tipos de eventos), foi utilizada uma matriz de correlação baseada na correlação de Kendall's Tau. Após preparar a base de dados de treinamento, esta foi utilizada para ensinar o modelo supervisionado no qual o algoritmo KNN (biblioteca scikit-learn) foi aplicado. O algoritmo KNN foi escolhido devido à sua simples aplicação. Como este algoritmo mede a distância entre pontos, a distância Euclidiana foi utilizada. Além disso, os valores dos dados foram normalizados utilizando uma função min-max, de modo que os dados apresentassem todos os valores entre -1 e 1. A precisão do modelo foi medida utilizando o método de validação cruzada *k-fold*, onde os dados foram distribuídos em 10 partições. Neste método, todas as partições são utilizadas uma vez para testar o modelo, enquanto as partições restantes são utilizadas para treiná-lo. Ao fim, um valor de precisão médio é obtido.

Para quantificar quais mecanismos de tenacificação são promovidos ao longo dos ensaios mecânicos, os sinais de AE coletados das amostras de testes finais – Al_2O_{3f}/Al_2O_3 e C_f/SiC – foram inseridos como dados de entrada no modelo supervisionado obtido. Como resposta, o

modelo entrega os dados rotulados quanto a qual tipo de evento o sinal de AE está associado (ruptura de fibra, trincamento, arrancamento, desplacamento, ou fricção).

Resultados e Discussões

Os resultados estão divididos em três tópicos e estão dispostos de acordo com as etapas necessárias para atingir os objetivos deste trabalho.

O primeiro diz respeito aos ensaios mecânicos designados como pré-testes. Deve-se enfatizar que os ensaios mecânicos foram conduzidos de maneira a isolar os tipos de mudanças estruturais que poderiam ser promovidas. Ainda assim, esta não é uma técnica com total eficiência. Em ensaios de amostras de arrancamento e placa compósita, além do tipo de sinais de AE "alvo" ao qual almejava-se mensurar (arrancamento e desplacamento respectivamente), sinais de trincamento e ruptura de fibra também foram promovidos. Para contornar isso, a ordem dos ensaios foi efetiva para discriminar entre os eventos. Por meio da comparação das informações prévias, pode-se distinguir quais sinais de AE estavam associados a um tipo específico de evento. Em geral, eventos de trincamento e fricção estão associados a baixas amplitudes (30~50 dB), seguidos pelos mecanismos interfaciais com amplitudes médias (50~70 dB), e ruptura de fibra associada a valores maiores (70~90 dB). A partir das informações de AE coletadas de cada ensaio, uma base de dados de treinamento para o modelo supervisionado foi elaborada.

O segundo está associado a criação do modelo supervisionado. Após avaliar a matriz de correlação de Kendall's Tau, os descritores selecionados para descrever o modelo foram amplitude (A), energia (E), e frequência média (F) devido ao seu maior valor de correlação. Em seguida, o modelo supervisionado foi treinado a partir dessa base de dados, e a precisão foi avaliada pelo método de validação cruzada. A precisão de identificação obtida do modelo foi de a 88%. Isto significa que o modelo pode reconhecer e discriminar entre os sinais que são fornecidos a ele. A precisão de identificação individual de cada evento foi a seguinte: trincamento (59%), desplacamento (97%), ruptura de fibra (84%), arrancamento (34%), e fricção (96%). Deve-se enfatizar que os eventos de trincamento e arrancamento apresentaram uma precisão de identificação reduzida se comparado aos outros. Uma das razões pelas quais isto ocorreu é devido à semelhança entre os valores de A, E, e F que os descrevem. Observou-se que ambos desplacamento e arrancamento possuem valores semelhantes. Isso ocorre pois ambos são mecanismos interfaciais. Um comportamento semelhante foi observado para eventos de trincamento e fricção. Essas similaridades podem dificultar a identificação dos eventos de menor precisão.

O último tópico de resultados aborda a avaliação do desenvolvimento da falha, e quantificação dos mecanismos em compósitos de $Al_2O_{3f}/Al2O_3$ e C_f/SiC. Os parâmetros de AE *hits* cumulativos (CHIT), e energia (E) foram utilizados para avaliar da quantidade de eventos promovidos, e a energia dissipada por cada um deles. Primeiramente, em relação aos compósitos de (1) $Al_2O_{3f}/Al2O_3$, estes são divididos em dois tipos: minicompósitos, ensaiados em tração, e placas compósitas, ensaiadas em flexão a 4-pontos. A classificação dos sinais de AE do primeiro demonstrou-se condizente com a literatura, onde os tipos de dano foram acionados próximos a seguinte ordem: trincamento, desplacamento, ruptura de fibra, e arrancamento. A fricção entre as interfaces pode ser observada em vários estágios ao longo do ensaio. Para a amostra avaliada, os seguintes valores de CHIT e E foram observados para cada tipo de evento: trincamento (CHIT = 22,5%, E = 1,2%), desplacamento (CHIT = 31,6%, E = 8,7%), ruptura de fibra (CHIT = 25,5%, E = 86,1%), arrancamento (CHIT = 12,7%, E = 3,9%), e fricção (CHIT = 7,7%, E = <0,1%). Em contrapartida, as placas compósitas de $Al_2O_{3f}/Al2O_3$ apresentaram um desenvolvimento da falha distinto, comportamento que foi associado ao estado de tensões promovido pelo ensaio de flexão. Por conta disso, uma maior quantidade de

eventos de trincamento e fricção das interfaces foi promovida, diminuindo a contribuição de eventos relacionado a ruptura de fibra, onde: trincamento (CHIT = 39,6%, E = 8,7%), desplacamento (CHIT = 26,4%, E = 35,2%), ruptura de fibra (CHIT = 4,6%, E = 42,4%), arrancamento (CHIT = 15,0%, E = 13,1%), e fricção (CHIT = 14,4%, E = 0,6%). Por último, os compósitos de C_f/SiC foram avaliados. Conforme descrito anteriormente, placas compósitas 2.5D C_f/SiC foram previamente fadigadas, e posteriormente submetidas a ensaios de tração até a falha (com monitoramento por AE). A classificação dos sinais de AE pelo modelo supervisionado permitiu avaliar as mudanças no desenvolvimento da falha promovidas pelos ensaios de fadiga. Em geral, os principais resultados estão associados a um alívio de tensões para as amostras que foram fadigadas. O alívio de tensões foi associado a uma redução dos eventos de fricção identificados pelo modelo (de 43,8% para amostra virgem, para 11,4~22,9% para amostras fadigadas), e é corroborado por uma tendência ao aumento na tensão de resistência do compósito para essas amostras. Em contrapartida, o módulo elástico diminui por conta do acúmulo de danos promovido durante os ensaios de fadiga. Outro resultado importante está relacionado a deterioração da interface. As amostras previamente fadigadas apresentaram um aumento na quantidade de eventos identificados como ruptura de fibra, arrancamento, e desplacamento, se comparadas a amostra virgem. Isso foi relacionado à deterioração da interface promovida pelos carregamentos cíclicos, que facilitam a atividade desses eventos. Isso é corroborado pela análise da superfície da amostra carregada por 2.000.000 de ciclos, que apresenta sinais de deterioração, como a ruptura de fibras individuais.

Considerações Finais

Contemplando o objetivo deste trabalho, foram propostos três pontos principais: (1) A análise de cada mecanismo separadamente; (2) a obtenção de um modelo de aprendizagem de máquina supervisionado; e (3) quantificação e avaliação dos danos em Al_2O_{3f}/Al_2O_3 e C_f/SiC CMCs. Os resultados apresentados no anterior trazem as seguintes conclusões:

(1) O procedimento para isolar os sinais de AE associados a cada mecanismo de tenacificação foi bem sucedido e permitiu a obtenção de um conjunto de dados de treinamento.

(2) As semelhanças entre os parâmetros de AE afetaram a precisão de identificação dos eventos de trincamento e arrancamento. Ainda assim, uma precisão de 88% foi obtida para o modelo, o que significa que podemos utilizá-lo para discernir entre os sinais de AE, mas erros de classificação precisam ser considerados para eventos de menor precisão.

(3) Comparadas à literatura, as análises demonstraram um bom desempenho para o modelo supervisionado, onde foi possível quantificar o tipo de dano promovido, e obter informações acerca da contribuição de energia dissipada por cada um, tanto em compósitos de Al_2O_{3f}/Al_2O_3 quanto C_f/SiC. Além disso, as mudanças promovidas pelos ensaios de fadiga puderam ser avaliadas para os compósitos de C_f/SiC, como o alívio de tensões e deterioração da interface. Os resultados mecânicos e MEV dão suporte aos resultados observados com a utilização do modelo supervisionado.

Palavras-chave: compósitos de matriz cerâmica; mecanismos de tenacificação; emissão acústica; aprendizagem de máquina.

ABSTRACT

Ceramic matrix composites (CMCs) stand out due to their low density and remarkable mechanical properties. The constituents that form them can be either all non-oxide (NOx-CMCs), all-oxide (Ox-CMCs), or a mixture of both. In general, the former has more desirable mechanical properties, while the second stands out in aggressive environments due to their oxidation resistance. A mixture can be used depending on the application and environment conditions. Unlike monolithic ceramics, these materials are known for presenting a non-brittle fracture. The damage tolerance of CMCs is possible due to several crack deflection mechanisms, such as matrix cracking, interface debonding, and fiber pull-out. Hence, understanding how these damage mechanisms work is crucial for the further development of these composites. In this work, mechanical tests jointly with acoustic emission (AE) monitoring were performed to study the damage development during the loading of CMCs. Specific mechanical tests provided means for simulating the damage mechanism. AE signals were related to each mechanism and used to obtain a training dataset for a supervised machine learning model. This approach is advantageous since each damage mechanism was analyzed individually. The model was then used to classify AE signals measured during mechanical tests of carbon fiber-reinforced silicon carbide matrix and alumina fiber-reinforced alumina matrix composites (C_f/SiC and Al_2O_{3f}/Al_2O_3 respectively). The results obtained have shown that the model can be successfully applied to identify the damage mechanisms. Furthermore, through this technique it is possible to evaluate the amount of mechanisms triggered, and energy dissipated by them during mechanical loading. These results are represented in total percentages of occurrence.

C_f/SiC composite plate samples were previously fatigued, and the changes promoted by fatigue cycles could be evaluated. The fatigue cycles promoted an increase in pullout, debonding, and fiber break events. Al_2O_{3f}/Al_2O_3 minicomposite and composite plate samples showed distinct failure development. In general, minicomposites showed most of their energy dissipated by fiber break (~86%), while composite plates showed most of their energy dissipated by deflection mechanisms (~57%).

Keywords: ceramic matrix composites; damage mechanisms; acoustic emission; machine learning.

LIST OF FIGURES

LIST OF TABLES

LIST OF ACRONYMS, SYMBOLS, AND ABBREVIATIONS

A	Amplitude
AE	Acoustic emission
CHIT	Cumulative hit count
CMC	Ceramic matrix composite
CVI	Chemical vapor infiltration
C_f/SiC	Carbon fiber-reinforced silicon carbide matrix
D	Duration
d_{50}	Average particle size
DDT	Duration discrimination time
E	Energy of an AE event
F	Average frequency
FEM	Finite element method
K_{IC}	Fracture toughness
KNN	k-nearest neighbor
LSI	Liquid silicon infiltration
ML	Machine learning
MMC	Metal matrix composite
NOx-CMCs	Non-oxide ceramic matrix composites
Ox-CMCs	Oxide ceramic matrix composites
PMC	Polymer matrix composite
R	Rise time
RT	Rearm time
SBB	Short-beam bending tests
SD	Standard deviation
SEM	Scanning electron microscopy
SENB	Single-edge notched bending tests
SGD	Stochastic gradient descent
TCC	Threshold crossing counts
V_F	Fiber ratio (%vol)
V_P	Pore ratio (%vol)
WIC	Weak interface composite
WMC	Weak matrix composite
Γ_F	Fiber fracture energy
Γ_I	Interface fracture energy

SUMMARY

1. INTRODUCTION AND OBJECTIVES

1.1. INTRODUCTION

Ceramic matrix composites (CMCs) have been developed to improve the low damage tolerance of monolithic ceramics. This group of materials can be categorized according to the constituents that manufacture them: All non-oxide (NOx-CMCs) and all-oxide (Ox-CMCs). Mixtures of oxide and non-oxide constituents are also possible depending on the application. While non-oxide constituents were the first developed to obtain high-temperature composites for structural applications, CMCs based on all-oxide materials have gained more attention due to their chemical stability, since they are oxide by nature.

The high fracture toughness and, consequently, damage tolerance of these composites is normally achieved with the use of either a weak fiber/matrix interface or a porous matrix. This allows for several crack deflection mechanisms to take place before fiber break, which later leads to composite failure. These mechanisms are matrix cracking, fiber debonding, and fiber pull-out.

Even though CMCs show high strength and toughness, crack propagation and deflection during loading of CMCs is still not fully understood. Understanding those mechanisms is pivotal for the development of these materials, but more experimental data is needed. With the development of data acquisition techniques, acoustic emission (AE) monitoring emerged as a way to acquire the necessary experimental data. This acquisition method enables the recording of acoustic waves emitted by testing specimens under mechanical load. The wave parameters have the potential to locate and identify the damage source. To do that, different approaches have been used for correlating the information recorded with each damage mechanism, e.g., numerical modeling, signal processing, and computed tomography (SAUSE, 2013; SUZUKI et al., 1996; VAN STEEN et al., 2019). However, these approaches lacked specificity, the results obtained were still very hypothetical. More recently, machine learning (ML) approaches improved the potential for identifying the damage source. Such approaches can be based on unsupervised and supervised ML models. The first is related to data clustering and needs less human input. Some works already used this approach (KOSTOPOULOS et al., 2003; LI et al., 2014; MOEVUS et al., 2008a; XU et al., 2019). However, it can be hard to associate the clusters to a specific damage mechanism, and other techniques may be needed to assist in it (BANSAL;

LAMON, 2015). Different from the first approach, the second learns from a training dataset. The supervised model is capable of learning from this previous input data, and then perform the classification of new encoded data. Then, a high accuracy for source identification may be achieved if a training dataset that represents each of the damage mechanisms is provided. Hence, this works aimed to use the supervised approach.

This work is a continuation of the student's diploma thesis, and a collaboration project between the Advanced Ceramics Group at Universität Bremen and the Federal University of Santa Catarina (UFSC). Since the work first started, improvements were made on the analyses methods, enabling the obtention of new results and the evaluation of other materials. The focus was to analyze each damage mechanism separately to create a training dataset. To this purpose, each damage mechanism was analyzed on samples made of alumina (Al_2O_3) fibers Nextel 610, and Al_2O_3 matrices. Several mechanical tests were utilized to promote specific damage mechanisms, in which acoustic waves were recorded by acoustic emission monitoring. This acoustic emission data was used to create a supervised ML model based on the k-nearest neighbor algorithm. In the end, this model was applied for identifying which mechanisms occurred in carbon fiber-reinforced silicon carbide matrix and alumina fiber-reinforced alumina matrix CMCs. The first, known as C_f/SiC, is composed of all non-oxide constituents, while the latter is an all-oxide CMC, referred to as Al_2O_{3f}/Al_2O_3.

1.2. OBJECTIVES

Contemplating the work context, the main objective is to quantify the damage mechanisms of CMCs that take place during mechanical loading. To achieve this objective, the following specific objectives must be achieved:

- Analyze each damage mechanism separately to obtain the experimental data through AE monitoring and mechanical tests (e.g., fibers tensile tests, matrix 4-point bending tests, fiber pull-out tensile tests). Each mechanical test is expected to promote either fiber, matrix, and/or interface related mechanisms;
- Create a supervised ML model using the encoded AE data respective to each damage mechanism as a training dataset;
- Use the obtained model to associate the damage source to a specific damage mechanism, performing quantification and assessing the damage development.

2. LITERATURE REVIEW

To properly introduce the reader to the subject of this work, this section covers a quick review of composites and their properties as well as the structure of CMCs, group of materials analyzed in this work. Towards understanding crack deflection, the roles of the fiber, matrix, and interface on the composite performance are also covered here. Lastly, failure mechanisms are described along with acoustic emission analysis and signal characterization.

2.1. CERAMIC MATRIX COMPOSITES

A composite material is defined as a macroscopic combination of two or more distinct materials, commonly referred to as constituents, having a recognizable interface between them. A composite aims to achieve unique properties, having a balance that is superior to either constituent material alone. Their desired properties will depend on which field they are aimed for, be that structural, electrical, thermal, tribological, or environmental applications. (ASM INTERNATIONAL HANDBOOK COMMITTEE, 2001). As the focus of this work is on structural composites, their mechanical properties will be further explained.

The two constituents of a structural composite are normally a reinforcement phase and a matrix. The reinforcement phase can be found in different shapes, such as fibers, whiskers, and particles. Its primary role is to sustain the load and provide strength and stiffness. As for the matrices, besides holding the reinforcements in their proper position and protecting them from the external environment, they are also responsible to transfer the load between them (BRIGANTE, 2014; CAMPBELL, 2004). Concerning the composite final properties, they are related to the properties of their constituents, such as geometry, distribution, orientation, the concentration of the reinforcement material, and also on the nature of the matrix-reinforcement interface (CAMPBELL, 2004).

There are different manners to categorize composites. One of these manners is according to the nature of the matrix (CHAWLA, 1993; MATHEWS; RAWLINGS, 1994). The main ones are:

- Metal-matrix composites (MMCs) – A metal composes the matrix, such as aluminum, magnesium, and titanium; and another material as the reinforcing phase, e.g., ceramic particles, whiskers, and fibers.
- Polymer-matrix composites (PMCs) – Polymers can be divided into three sub-types: thermoset, thermoplastic, or rubber. PMCs consist of a polymer matrix combined with a reinforcing phase, such as fibers or particulates composed of carbon, glass, or aramid.
- Ceramic-matrix composites (CMCs) – Designed to overcome major disadvantages such as low fracture toughness and brittleness of traditional ceramics. Examples of CMCs can be oxide/oxide composites such as alumina fiber-reinforced alumina matrix (Al_2O_{3f}/Al_2O_3), non-oxide/non-oxide such as carbon fiber-reinforced silicon carbide matrix (C_f/SiC), or a mixture of both. For instance, an example of the latter could be SiC whiskers-reinforced alumina matrix (SiC_w/Al_2O_3).

From those classes, MMCs have some applications in the aerospace, automotive, and electrical fields, mainly due to their high melting point, elastic, and electrical properties. Despite that, the drawbacks are their relatively high processing temperatures and higher densities when compared to other composite classes (MATHEWS; RAWLINGS, 1994). PMCs are known for their low cost and simple fabrication methods. Although those materials applications have increased in the naval and automotive industry, which can be attributed to PMCs low density and good mechanical properties, they are still limited due to their low thermal resistance (MATHEWS; RAWLINGS, 1994). CMCs are still considered new and present big potential in industries such as aerospace and automotive. This is justified with certain properties. For instance, properties already present on monolithic ceramics, such as high-temperature capability and low density, when allied with the high toughness of CMCs, make the interest in this class of materials increase for a vast range of applications (CHAWLA, 1993; PARK; SEO, 2011). In specific, although ceramic materials are known as having high strength, they also show brittle fracture that can be seen by their unexpected failure without plastic deformation. On this matter, studies were made to improve their low damage tolerance. Those studies resulted in the production of CMCs, materials that provide toughness to an otherwise brittle ceramic matrix, as seen in Figure 1.

Figure 1 – Mechanical behavior of monolithic ceramics and ceramic matrix composites.

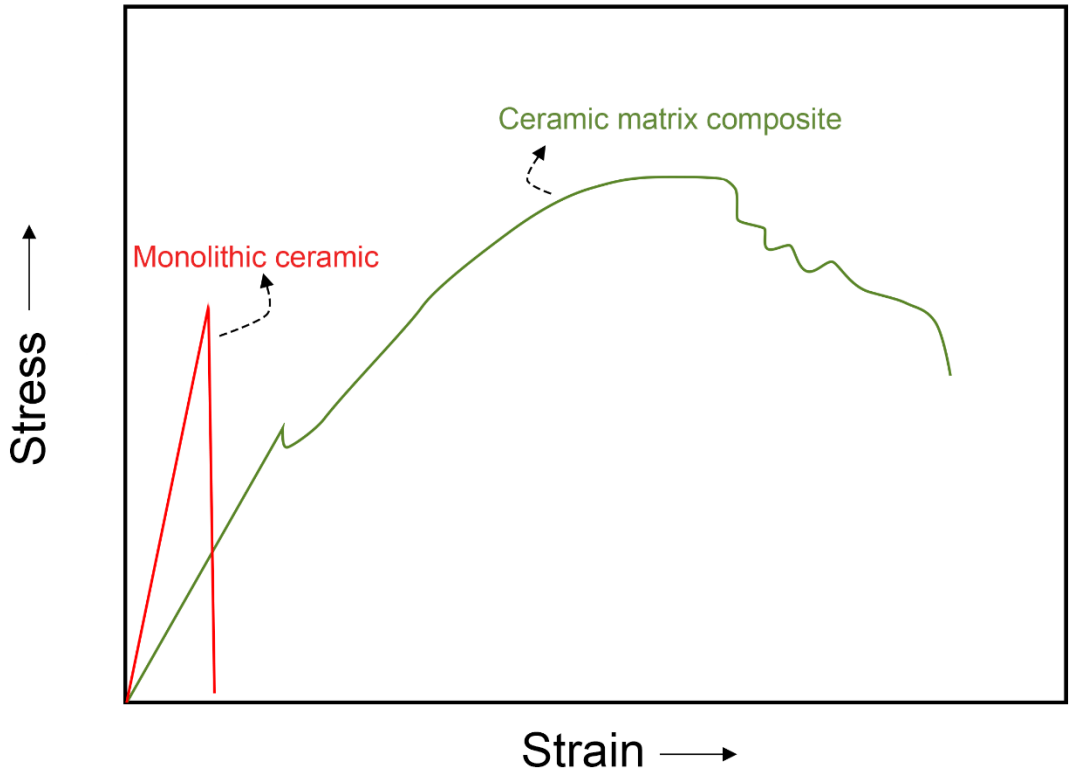

Source: Adapted from PARK; SEO (2011, p. 612)

To achieve this higher damage tolerance, understanding the interactions between fiber, matrix, and the interface between them is crucial. The proper combination of both fibers and matrix allows crack-deflection mechanisms to happen. Thus, damage tolerance is enabled, and an overall *quasi*-ductile behavior is observed (KOCH et al., 2006). This behavior is a measurable non-linear deformation before failure, which can be recognized by the decrease of inclination seen in Figure 1. The general approach for this is that failure processes in the matrix do not induce fiber failure. Therefore, the fibers can bridge the matrix cracks preventing catastrophic failure (KOCH et al., 2006).

Aligning this intrinsic property of CMCs with other interesting properties of traditional monolithic ceramics, for example, high strength, thermal and chemical stability, improves the range of applications of CMCs (TUSHTEV; MARTIN ALMEIDA, 2018). Due to their higher temperature and thermal shock resistance, when compared to metals and monolithic ceramics, components based on CMCs can be used to increase gas turbine efficiency and on brake systems of aeronautical and automotive vehicles (KRENKEL, 2008; STEIBEL, 2019).

Concerning their constituents, the fibers used in CMCs offer higher strength and stiffness compared to the matrices. The matrices, in contrast, are characterized by inferior properties, exhibiting microcracks, residual pores, or inhomogeneities caused by the fabrication process (KOCH; TUSHTEV; GRATHWOHL, 2008). The main task of the ceramic matrix in a CMC is to distribute and transfer the applied loads to the fibers, ensuring the structural stability of the composite. Besides, they also contribute to physical properties such as thermal conductivity, thermal expansion, and permeability. Thus, the choice of the matrix is also important. Hence, CMCs can be categorized according to the nature of their constituents. In this work, all non-oxide and all-oxide CMCs will be covered.

2.1.1. Non-oxide Ceramic Matrix Composites

In this subgroup, silicon carbide-based materials are the most prevalent (SHINAVSKI, 2018). The applications are primarily related to high temperatures or tribological applications, such as carbon-fiber-reinforced silicon carbide (C_f/SiC) for rocket thrusters and brake systems, and silicon carbide fiber-reinforced silicon carbide matrix (SiC_f/SiC) for jet engine hot-section combustor, turbine, and exhaust components (SHINAVSKI, 2018).

Since these materials are non-oxide and that most applications are related to higher temperatures, susceptibility to oxidation exists in environments containing oxygen and water vapor. The degree and nature of oxidation depend on the composite constituents and if the composite is damaged in a region exposed to oxidizing conditions (MORSCHER; PARTHASARATHY; CINIBULK, 2018). For this reason, there is a trend towards producing NOx-CMCs with improved temperature capability. The optimal selection of constituents and the processing methods to produce these composites govern the resulting properties for these applications. The key points for that are having matrix structures capable of protecting the fibers from the environment, as well as fiber coatings. Aside from providing additional protection, fiber coatings are responsible for enabling a weakly bonded interphase, which is essential to their crack deflection (SHINAVSKI, 2018).

Concerning the reinforcements, SiC-based fibers are the most common. These fibers can be categorized according to their composition (SHINAVSKI, 2018). Higher grade fibers, such as Hi-Nicalon Type S (Nippon Carbon, Tokyo, Japan) and Tyranno SA1-3 (Ube

Industries, Tokyo, Japan) present a near stoichiometric composition ($C/Si \cong 1$), with higher modulus ($E > 350\,GPa$) and temperature stability due to their crystalline structure (DICARLO; YUN, 2005; SHINAVSKI, 2018). Intermediate and lower grades possess reduced properties ($E \cong 220 - 270\,GPa$) and temperature stability, but with smaller costs, e.g., Nicalon and Tyranno ZMI (DICARLO; YUN, 2005). Aside from SiC-based fibers, other options are available. For instance, polyacrylonitrile (PAN)-based carbon fibers, such as T300 and T700 (Toray Industries, Tokyo, Japan), with an elastic modulus of 230 and 240 GPa respectively. Table 1 summarizes the properties of SiC-based NOx-CMCs where the aforementioned fibers were employed, highlighting the fiber (V_F) and closed porosity (V_P) volume ratios, tensile strength, and elastic modulus.

Table 1 – Room temperature properties of 2D carbon-based NOx-CMCs with 0/90 degrees fiber reinforcement.

Composite (Fiber/Matrix)	V_F (%)	V_P (%)	Tensile Strength (MPa)	Elastic Modulus (GPa)
Nicalon/SiC	40	10	200	230
Hi-Nicalon type S/SiC	35	--	341-412	232-262
Tyranno-SA3/SiC	53	0.6	408	358
T300/SiC	40	13	312	111

Source: Adapted from LAMON (2012); WANG et al. (2008)

2.1.2. Oxide Ceramic Matrix Composites

To find further suitable options for oxidizing environment applications, research interests turned to the development of oxidation-resistant ceramic composites. Although NOx-CMCs usually present higher mechanical properties and thermal stability when compared to Ox-CMCs, they are limited in lifetime by oxidation and are subjected to faster degradation in combustion environments (KELLER; JEFFERSON; KERANS, 2005). With the sacrifice of some mechanical performance, superior environmental stability can be achieved by using all oxide composites (CHAWLA, 1993; KELLER; JEFFERSON; KERANS, 2005). For this reason, Ox-CMCs are interesting in the production of components for gas turbine engines on aircrafts, aerospace propulsion, and power generation (DICARLO; VAN ROODE, 2006; MOMSON; KAUTH, 2010; SZWEDA et al., 2005).

The development of oxide fibers is dated to 1970. Still, those were not intended for mechanical applications. Only in 1993 that suitable alumina fibers were produced by the American Company 3M, known as Nextel 610. Their strength is 31000 MPa, according to their producer, and is considered the strongest oxide fiber available. Later on, 3M presented the Nextel 720, which has a strength of 2100 MPa, but better performance at temperatures above 1000 ºC (TUSHTEV; MARTIN ALMEIDA, 2018). Nowadays, those two fibers are the ones typically used in commercial applications (RÜDINGER; NÖTH; PRITZKOW, 2015). The matrices used are normally based on either pure or mixtures of alumina, silica, mullite, and zirconia (CHAWLA, 2000; TUSHTEV; MARTIN ALMEIDA, 2018).

The properties of Ox-CMCs are dependent on the constituents and manufacturing processes. Normally, they present a V_F ranging from 30 to 50 vol%. Therefore, most of the composite volume is composed of the matrix, which is much weaker than the fibers (VOLKMANN et al., 2015). Matrices normally demonstrate V_P around 25-40 vol%. Thus, matrix-dominating properties are typically low. When compared to monolithic ceramics, the fracture toughness, in terms of stress intensity factor, is two to three times higher for composites (TUSHTEV; MARTIN ALMEIDA, 2018). Because of the different possibilities of constituents for manufacturing Ox-CMCs, the fracture toughness is commonly observed in the range of 2-10 $MPa\sqrt{m}$ (TUSHTEV; MARTIN ALMEIDA, 2018; VOLKMANN et al., 2014). As for their thermal properties, the thermal expansion coefficient is in the order of 4 ppm/ºC, and conductivity is around 4 W/mK (KELLER; JEFFERSON; KERANS, 2005).

Currently, Ox-CMCs are commonly 2D reinforced with 0/90 degrees, or other usually symmetrical ($+\propto$ / $-\propto$ degrees) fiber orientations (TUSHTEV; MARTIN ALMEIDA, 2018). Considering that the fiber and matrix have rather different properties, the mechanical properties of those materials are considered orthotropic, presenting higher strength and stiffness in the direction of the fibers when loaded. Some works have already reported tensile strengths for Ox-CMCs close to 400 MPa (HALVERSON; CURTIN, 2002). Even so, generally the values reported are in the range of 120-300 MPa (TUSHTEV; MARTIN ALMEIDA, 2018). Table 2 summarizes the mechanical properties of some Ox-CMCs based on either pure or a mixture of alumina, mullite, and silica matrices.

Table 2 – Room temperature properties of 2D of Ox-CMCs with 0/90 degrees fiber reinforcement. A, alumina; S, Silica; M, Mullite. Fibers manufactured by [1]COI, Ceramics Inc., United States; [2]General Electric, United States.

Composite (Fiber/Matrix)	V_F (%)	V_P (%)	Tensile Strength (MPa)	Elastic Modulus (GPa)
[1]N610/AS	30	25	205	70
[2]N610/AS	51	25	366	124
[1]N720/A	44	24	169	60
[1]N720/AM	40	27	165	67.5
[1]N720/AS	48	22	179	77
[1]N720/AS	37	22	173	71

Source: Adapted from TUSHTEV; ALMEIDA (2018)

2.2. CONCEPTS FOR CRACK DEFLECTION

The deflection of matrix cracks at the fiber/matrix interfaces, and within matrix porosity, is the initial mechanism required for obtaining enhanced toughness in CMCs (AHN et al., 1998). From a mechanical standpoint, if a composite is loaded in tensile mode, because of the higher strength of the fibers, the crack propagation begins on the matrix. Following, the matrix crack propagates through the composite, being bridged by the strong fibers that should remain intact. In turn, high strength and toughness are provided. As the stress concentration at the interface does not induce fiber failure, interfacial debonding between fiber and matrix, and fiber pull-out start until ultimate failure when load locally exceeds the fiber strength (KOCH et al., 2006).

In Figure 2, the plot proposed by He and Hutchinson is shown. This plot shows a visual way to explain the requirements for crack deflection in CMCs in terms of the fracture energy ratio of fiber and interface ($\Gamma_I/\Gamma F$) and the difference in elastic modulus of fiber and matrix (E_F – E_M). In the case that fiber and matrix have similar properties ($E_F \approx E_M$), then the surface energy ratio should remain at $\Gamma_I/\Gamma F =\leq 0.25$ for crack deflection. Meaning that the maximum surface energy ratio to guarantee a weak interface, and consequently obtain a non-brittle behavior, is 0.25. However, if the elastic properties are rather different, a non-brittle behavior can still be achieved even if $\Gamma_I/\Gamma F > 0.25$ (HE; HUTCHINSON, 1989; KOCH et al., 2006). Thus, based on these requirements, two concepts can be used for enabling crack deflection:

Weak Interface Composites (WIC) and Weak Matrix Composites (WMC), both represented in Figure 2.

Figure 2 – Boundary curve according to He and Hutchinson for crack deflection/propagation taking into consideration the critical relative fracture energy dependent and the stiffness ratio of fiber and matrix. Displays both the weak interface composite (WIC) and weak matrix composite (WMC) concepts, necessary for crack deflection. Additional effects of oxidation and matrix densification through reinfiltration on the failure behavior are shown.

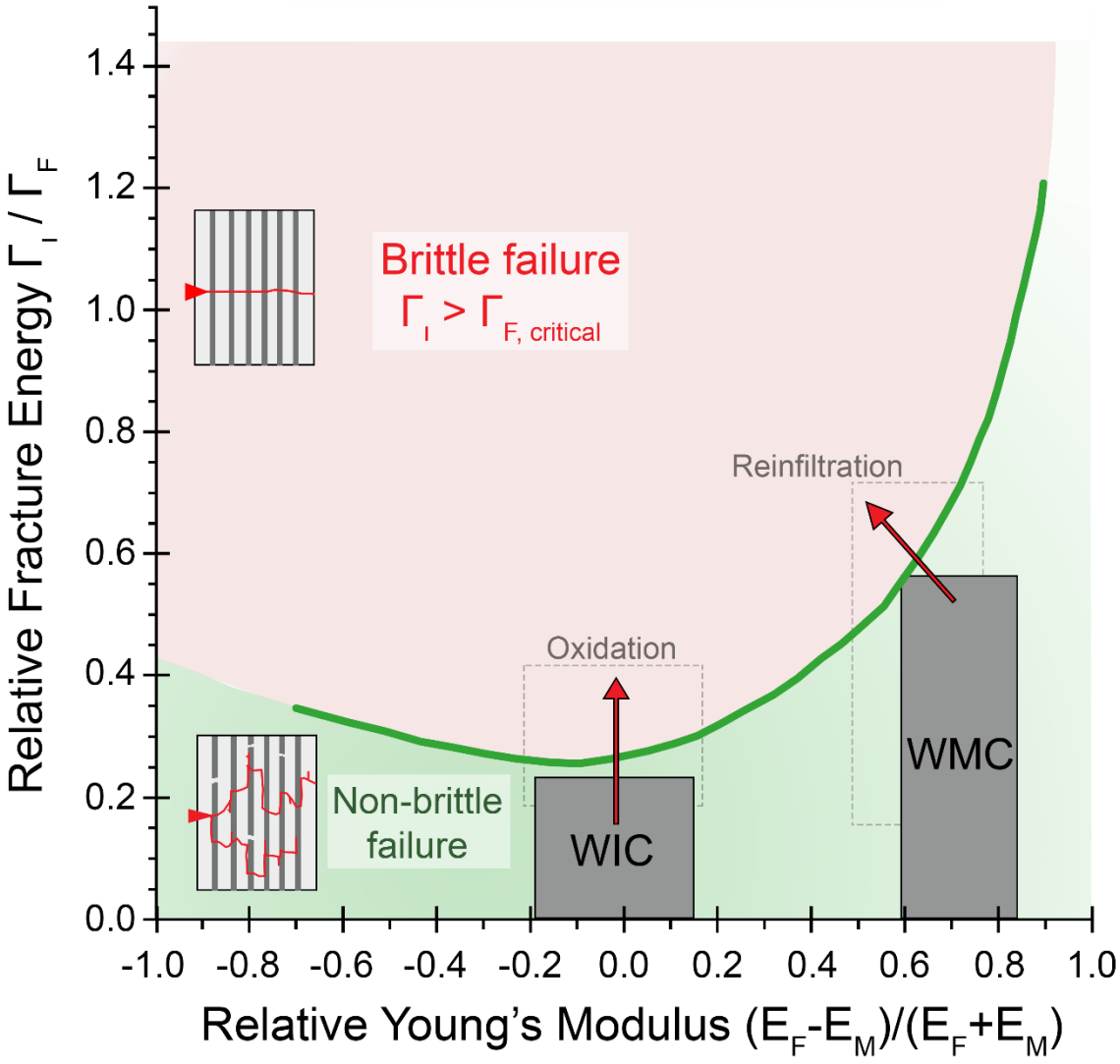

Source: Adapted from KOCH; TUSHTEV; GRATHWOHL (2008, p. 1166)

The more conventional approach is the WIC, which involves the use of fiber coatings to promote crack deflection along the fiber/matrix interfaces (Figure 3), causing debonding and frictional sliding. As the crack propagates through the matrix, fiber break occurs at higher loads, resulting in fiber pull-out and further sliding. The coating is applied before the composite processing, inducing a “sufficiently weak” interface that enables the deflection mechanisms.

Besides providing a weak bonding, they can also protect the fibers from interactions with the matrix and environmental attacks at service (TUSHTEV; MARTIN ALMEIDA, 2018).

Figure 3 – Schematics weak interface composite (WIC) concept, exhibiting the crack propagation with the activity of crack deflection mechanisms for achieving a non-brittle behavior.

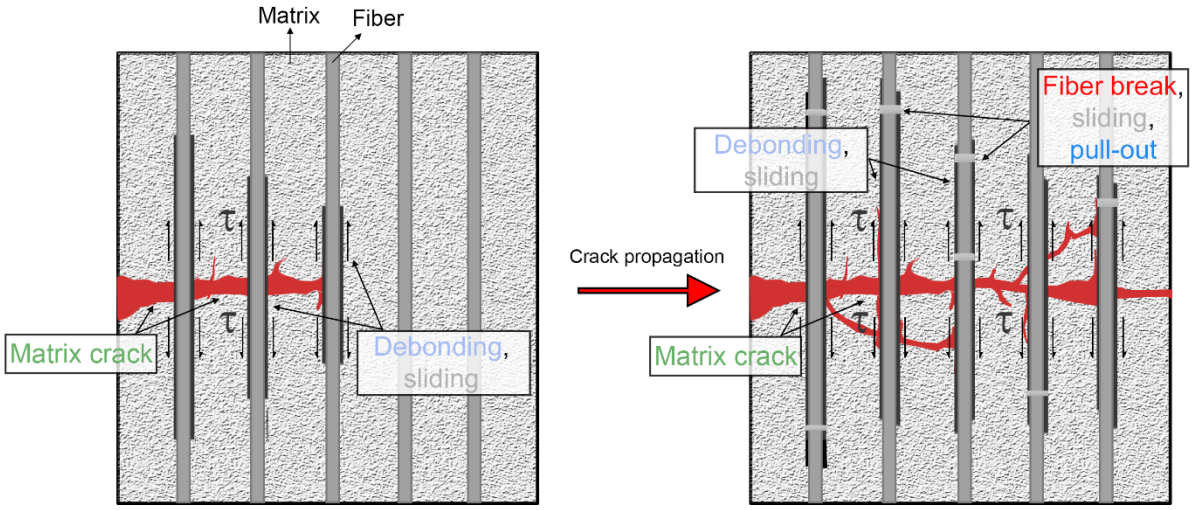

Source: Adapted from ZOK; LEVI (2001, p. 15)

The second approach, WMC, while also applied for NOx-CMCs, was primarily developed in the context of oxide-based composites. When it was first introduced, even though several coating technologies were already available at that time, they were not suitable for oxide fibers (TUSHTEV; MARTIN ALMEIDA, 2018). In the absence of fiber coatings, different means for crack deflection needed to be applied. Considering that the matrix should be sufficiently weak, the use of a controlled amount of distributed porosity on the matrix was a way to achieve that. Thus, micro-cracks are allowed to propagate and enable an energy dissipation during loading (PARLIER; RITTI; JANKOWIAK, 2011; ZOK; LEVI, 2001).

Mechanically speaking, the finely distributed porosity of WMCs enables matrix micro-cracking and a combination of crack deflection mechanisms close to the fiber/matrix interface, promoting fiber/matrix debonding and fiber pull-out later (Figure 4). Hence, the total level of porosity of these composites is very important (ZOK; LEVI, 2001). Generally, these levels are around 25-40%. Furthermore, since the matrix is weaker than the fibers, the mechanical performance of WMCs is strongly dominated by the properties of the fiber, their volume fraction, and orientation, as pointed in the previous sections.

Figure 4 – Schematics of weak matrix composite (WMC) concept, illustrating the crack propagation and the activity of damage mechanisms. The pores are highlighted for obtaining a weak enough matrix and achieve crack deflection.

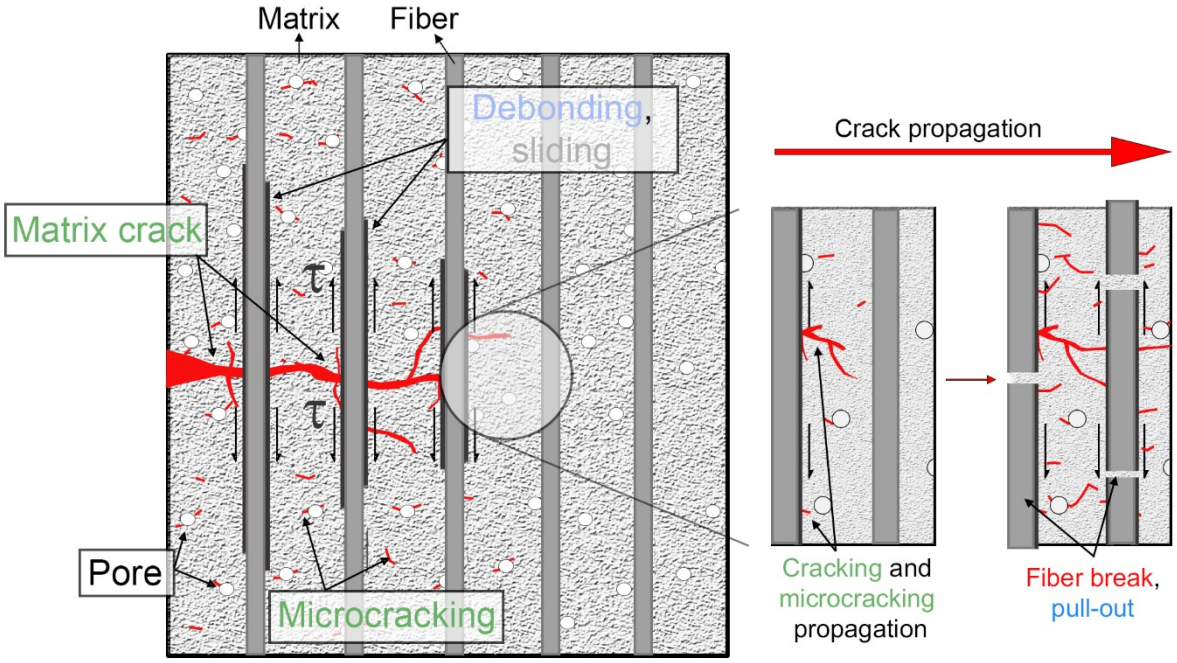

Source: Adapted from Adapted from ZOK; LEVI (2001, p. 15)

There are a few points that should be highlighted for both concepts. First, when WICs are applied at high temperatures and oxidative atmospheres, the fiber coatings may be attacked. If oxidation of the interphase layers occurs, the mechanical properties can be affected and change the relative fracture energy (Γ_I/Γ_F). Then, the failure changes from non-brittle to brittle. For WMCs, if the matrix density is increased to enhance the mechanical properties e.g., by reinfiltration steps, then brittle behavior might occur (ZOK; LEVI, 2001).

2.2.1. Damage Mechanisms

The enhanced damage resistance and increased toughness of CMCs are due to their inherent ability to effectively redistribute stresses around holes, notches, and cracks. The inelastic deformation at these sites is crucial to alleviate the elastic stress concentrations, by locally redistributing stress. As mentioned before, the basic phenomena for inelastic strains are crack deflections at the fiber/matrix interface, such as interface debonding and fiber pull-out (EVANS; ZOK, 1994). Each of those phenomena, also called damage mechanisms, takes place

during different times and places as the load progresses. Therefore, a quasi-ductile behavior is attained. Figure 5a exemplifies the fundamental structural changes occurring on CMCs as a crack propagates through the matrix (EVANS; ZOK, 1994; KOSTOPOULOS; LOUTAS; DASSIOS, 2007).

Figure 5 – Fundamental structural changes that occur in CMCs as a crack extends through the matrix. (a) Shows the main mechanisms and structural characteristics, while (b) the expected onset of each type of damage along a stress-strain curve.

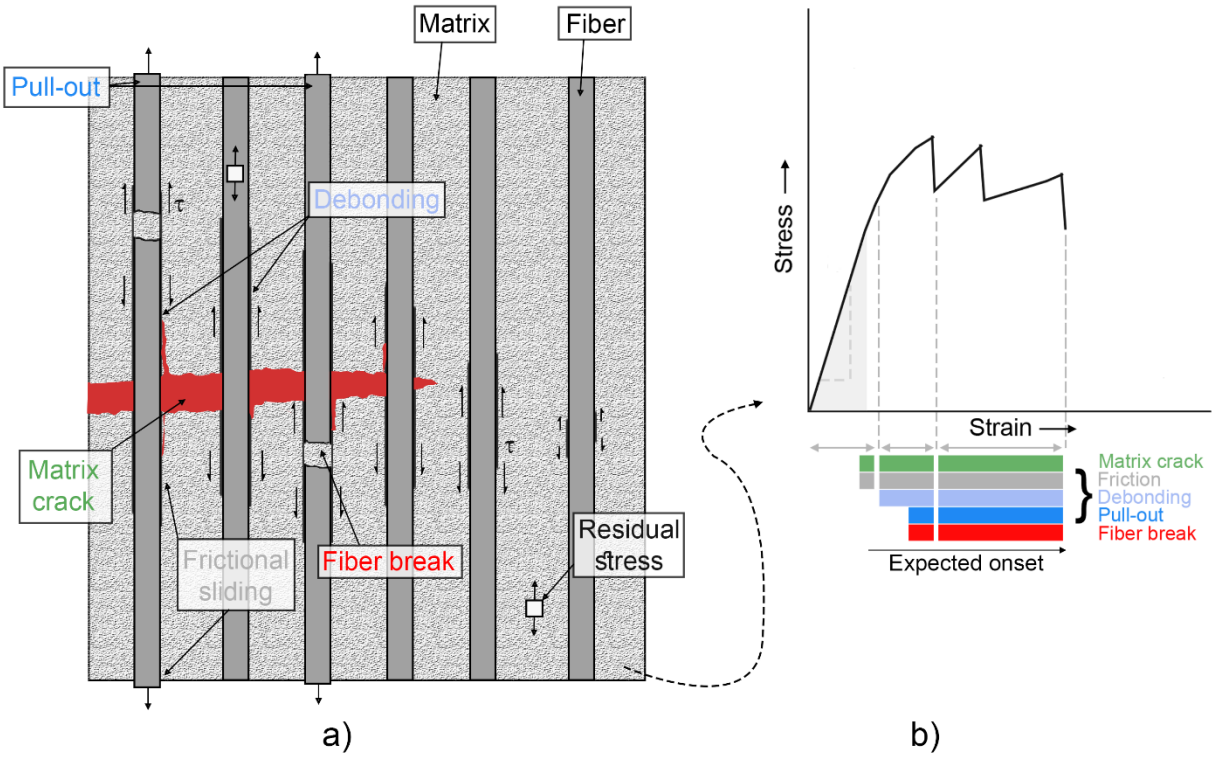

Source: Adapted from EVANS; ZOK (1994, p. 3859)

When the material is stressed, it is difficult to quantify the mechanisms acting. It is expected that as the load increases, the matrix is prominent to fail first due to its lower strength. If the properties of the composite are properly adjusted to allow crack deflection, interface debonding and fiber pull-out take place next. Subsequently, when the load is high enough, fiber break happens. After that, multiple damage mechanisms take place, leading to the failure of the composite (EVANS; ZOK, 1994; ZOK; LEVI, 2001). Additionally, friction and residual stress inherent to the manufacturing process can also be present. Since friction exists between all the composite interfaces (fiber/fiber, fiber/matrix), it can occur at all stages, as highlighted in Figure 5b. Because both friction and residual stresses are dependent on composite characteristics and properties, their levels might change the composite behavior. The three main crack deflection

mechanisms – matrix crack, interface debonding, fiber pull-out – are described next in addition to fiber break.

- Matrix Crack – The matrix cracks cause a redistribution of stress from the matrix to the fibers and a release of thermal residual stresses. The fibers elongate under the increased loads, and so the composite strain increases beyond the value given by Hooke's law;
- Interface Debonding – Fiber and matrix interface stops adhering to each other when a physical, chemical, or mechanical force that holds the bond together is broken. On ceramic matrix composites, this mechanism acts to promote higher fracture toughness, as a way to ensure the non-brittle failure of the composite through crack deflection;
- Fiber Pull-out – Consists of a fiber that debonds from the adjacent microstructure and is pulled out as the crack opens. The energy that would normally cause crack propagation is partially expended by debonding and friction, as the fiber slides against the bordering structures. It is normally associated with fiber break, that facilitates debonding;
- Fiber Break – The fiber breaks into two or more pieces along its length when the axial tensile stress in it exceeds the axial strength. Usually, fiber breaks are seen to occur close to the ultimate failure of the composite.

2.3. ACOUSTIC EMISSION AND MACHINE LEARNING

2.3.1. Acoustic Emission

The use of acoustic emission (AE) is a relatively new technique for non-destructive evaluation. AE can be defined as part of the energy dissipated and emitted because of changes in the material microstructure, which generates stress waves (GHOLIZADEH et al., 2018). When propagated to the surface, these stress waves cause the material to vibrate. Then, the vibration can be measured by several types of transducers, such as piezoelectric, capacitance, electromagnetic and optical. The last two have the advantage of being non-contact but are considered less sensitive than piezoelectric transducers, which are the most popular (UNNORSSON, 2013). The information recorded can be transformed into a voltage output and analyzed. Ultimately, to analyze the damage inside the material, AE can be used to detect

defects by monitoring the acoustic wave that is emitted from a testing sample (MOURITZ, 2012). Figure 6 shows the operating principles of acoustic emission monitoring.

Figure 6 – Principles of acoustic emission monitoring.

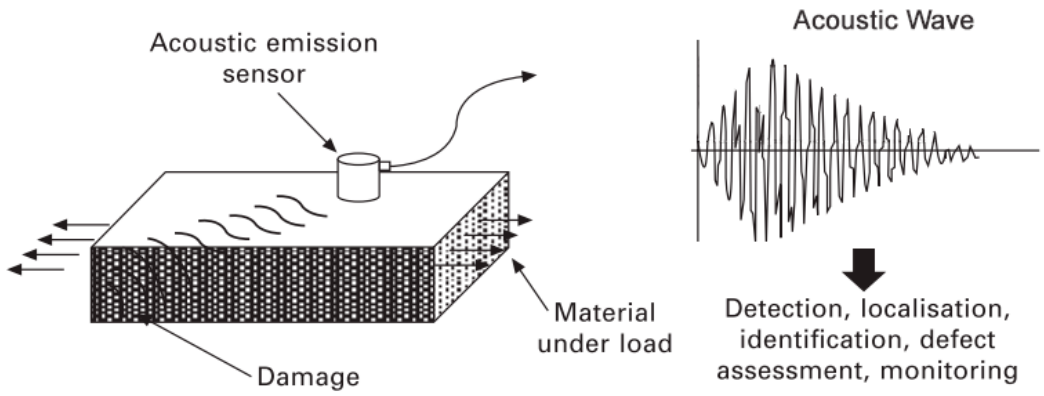

Source: Adapted from MOURITZ (2012, p. 548)

The AE events detected are known as hits. To analyze them, a method to automatically detect the hits is used. The most frequently used technique is the threshold method. This method compares the obtained electrical signal against a pre-defined voltage threshold level; whenever the signal rises above this threshold, a hit is detected (UNNORSSON, 2013). Aside from that, different user inputs can be changed. Besides the threshold, other main inputs are duration discrimination time (DDT), a time parameter related to the period without threshold crossings that defines a hit; and rearm time (RT), which defines the time for the machine to trigger a new hit evaluation. If threshold crossings occur inside RT, the hit is registered as a cascaded hit. In that case, it is implied that one hit generated other hits. If no threshold crossing occurs during this time, a single hit is confirmed. A typical AE wave is illustrated in Figure 7, with two separate AE events happening (EGGERT, 2014; UNNORSSON, 2013).

Figure 7 – Typical acoustic emission wave, highlighting features and user-input parameters.

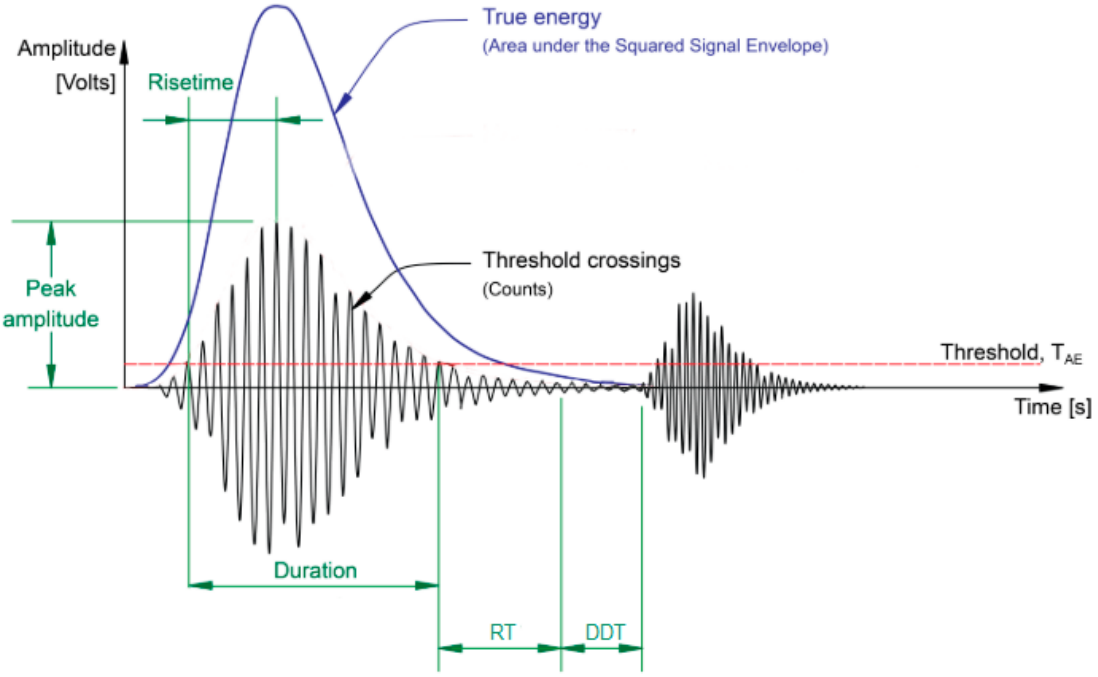

Source: Adapted from UNNORSSON (2013, p. 4)

Once a set of AE hits has been detected, hit-based features can be extracted. Since each wave recorded is presumably different, common hit-based features such as amplitude, rise time, energy, duration, and threshold crossing counts and frequency can be used to differentiate one another. This way, the AE event can be assigned to a specific change inside the material (BANSAL; LAMON, 2015). The amplitude is associated with the measured voltage in a waveform and is measured in decibels (dB). The time interval between the first threshold crossing and the signal peak characterizes the rise time, related to the source in which the wave is propagated. The energy is associated with the released energy for the specific acoustic emission event. The duration is the time difference between the first and last threshold crossings that define a hit. Lastly, the number of counts refers to the number of pulses emitted if the signal amplitude is greater than the threshold. Depending on the magnitude of the AE event and the characteristics of the material, one hit may produce one or more counts.

Acoustic emission analysis has been successfully used in a wide range of applications over the years. Those include detecting and locating faults in pressure vessels and leakage in storage tanks or piping systems, (SHEHADEH; STEEL; REUBEN, 2006); health monitoring of aerospace structures (GIURGIUTIU, 2016; MOURITZ, 2012); or even in real-time control of welding processes, where cracking can continue even after the weld has been completed

(ZHANG et al., 2018). In such cases, AE arises as a versatile technique to gather information about the material or structure. Because of its versatility, AE serves as a tool to analyze several structural changes in materials research (ONO, 2011).

2.3.2. Machine Learning

Machine learning (ML) is a captivating interdisciplinary tool that has high versatility and is based around algorithms and statistics. It can be understood as a tool where machines are able to learn from a particular set of information, and then employ this information to fulfill a specific task, such as regression analysis, pattern classification, and predictions (MOULOODI et al., 2021). In materials science, it can be used to accelerate the comprehension of materials through learning from observations (MOULOODI et al., 2021). Because of its versatility, the employment of ML has observed a fast growth in recent years (HONG et al., 2020). Frequent applications seen in the literature are related to the discovery of new compounds and prediction of material's properties and phase equilibria (RAMPRASAD et al., 2017).

Common ML algorithms can be divided in two categories, supervised and unsupervised. Supervised algorithms are associated with classification and regression problems. In these algorithms, a training dataset with labeled data is used as input, and the algorithm learns from this data. The main idea concerns building a relationship between input and output data to predict the latter from the former (MOULOODI et al., 2021). In contrast, unsupervised algorithms are usually used for data clustering. This is because no labeled data is provided beforehand. The algorithm mathematically groups a set of input data into clusters, and the clusters are then labeled manually.

2.3.3. CMCs Characterization Through Machine Learning and Acoustic Emission

Over the years, AE monitoring has been used as a way to study the fracture behavior of CMCs under quasi-static and dynamic loadings. Various works have already been published in this area (KOSTOPOULOS et al., 2003; KOSTOPOULOS; LOUTAS; DASSIOS, 2007; MAILLET et al., 2019; SAUSE, 2013).

Multiple damage mechanisms are present in CMCs, as described in subsection 2.2.1. During testing of these materials, a large quantity of AE signals is acquired. Because of that, the difficulty to quantify the source mechanism increases. Since certain defects have a characteristic sound frequency value, this parameter is often used to determine the type of damage present in the material (MOURITZ, 2012). Other than that, different works have used features such as the wave amplitude (ADDIN et al., 2007) or a combination of various wave features, such as amplitude, hits, and frequency (GHOLIZADEH et al., 2018; SHIWA et al., 1995). Still, correlating the acoustic wave signals with their respective damage mechanism is one of the challenges for using AE. Previous works used methods such as the finite element method (FEM) and scanning electron microscopy (SEM) to assist the labeling of a signal to a corresponding mechanism (KOSTOPOULOS et al., 2003; MOEVUS et al., 2008b; SAUSE, 2013). Yet, there is still room for improvement in this matter.

With the improvement in computer technology, software development, and sorting techniques, AE was enabled to become an even more powerful technique for monitoring damage and also quantifying the mechanisms (BANSAL; LAMON, 2015). One of those improvements is related to ML, which can be further used for data analysis, applying methods such as unsupervised and supervised pattern recognition algorithms. The algorithms interpret data, learn from it, and then find patterns from new data based on what they learned (GOODFELLOW; BENGIO; COURVILLE, 2016). For combining AE with ML Figure 8 emphasizes that damage mechanisms all emit different sound waves when they occur. For illustration, different crack types, debonding, and fiber break are highlighted as having specific wave patterns. Thus, through learning these patterns, ML can be applied for recognizing the source mechanism that can be measured through AE data.

Figure 8 – Schematic diagram illustrating the damage mechanisms involved in CMCs and their respective AE signals.

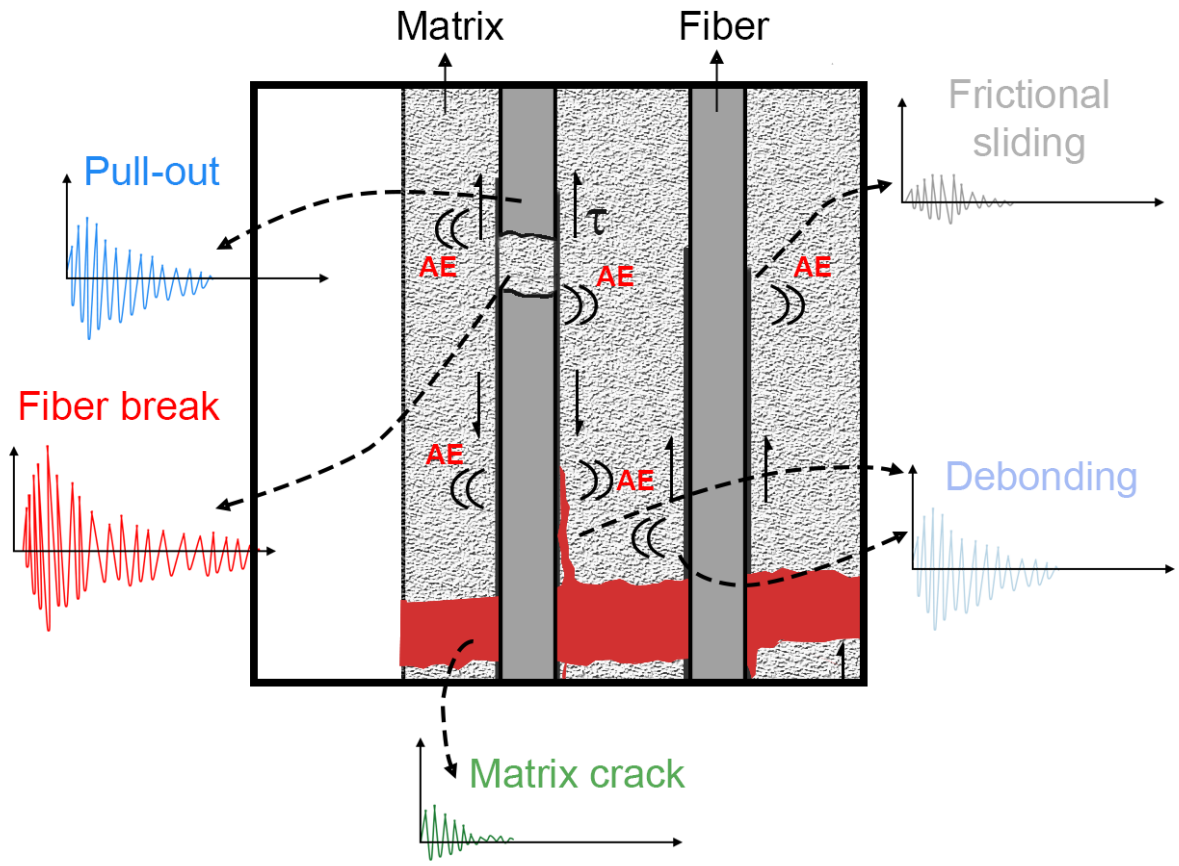

Source: author

On these lines, a ML algorithm can be applied. If no labeled data is available, an unsupervised methodology is one approach to perform an exploratory pattern analysis. With this approach, an unsupervised algorithm is selected, and the following steps are performed in order: data analysis; clustering; validation; and cluster labeling. After the clustering, which is performed by the unsupervised algorithm, labeling is done manually. More recently, MUIR et al. (2021) applied a similar approach for the damage mechanism identification in SiC_f/SiC composites. Despite that, the assistance of other methods might still be needed to confirm which damage mechanisms occurred and assign the mechanisms to each cluster (BANSAL; LAMON, 2015). Figure 9 shows a flow chart representation of this method.

Figure 9 – Flowchart representation of unsupervised pattern recognition method for the analysis of AE data.

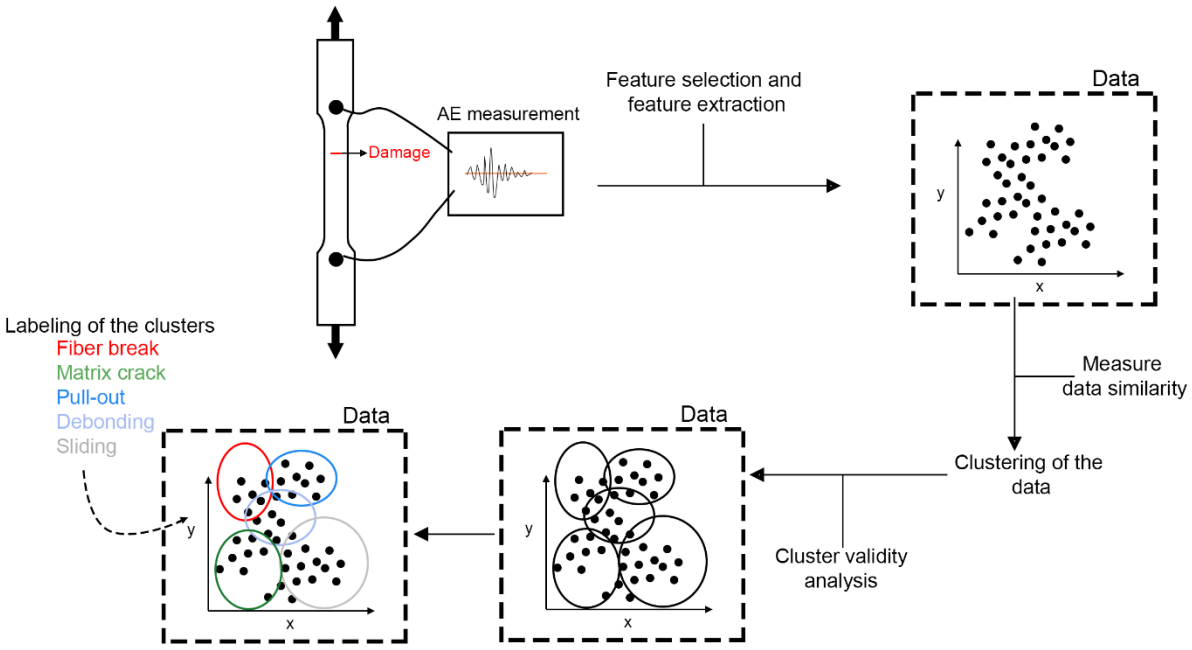

Source: Adapted from BANSAL; LAMON (2015, p. 583)

Another approach is a supervised pattern recognition methodology. As addressed before in subsection 2.3.2, this method requires a database of signals that have been manually labeled beforehand and used as a training dataset (BANSAL; LAMON, 2015). The classification is made by comparing the features of unlabeled data to previous features whose source is known. The known source comes from the training set that has labeled data, also called targets. From the algorithms that are commonly used for classification, some of them are the k-nearest neighbor (KNN), Naive Bayes, and the Stochastic Gradient Descent (SGD), which are available in the open-source scikit-learn python library (PEDREGOSA et al., 2011). The first one classifies an AE signal by finding the “k-closest” signals in the training set and then predicts the class by majority vote (BANSAL; LAMON, 2015; PEDREGOSA et al., 2011). The second is a probabilistic classifier inspired by the Bayes theorem. This algorithm assumes that the feature in a class is unrelated to any other. The last one works by drawing a straight line between two classes, creating a hyperplane to divide and categorize the data. Based on the distance between the two nearest points, known as margin, the objective is to select a hyperplane with the maximum possible margin between the two points (ALPAYDIN, 2007).

Choosing which approach to use is going to be related to the type of problem one has. Unsupervised learning can give information from unknown data. In spite that it does not need that much human input, the specificity of the problem may be affected, as the input data is not

known and not labeled by people in advance. Unsupervised clustering was applied on cases that lacked prior knowledge of different signal classes in CMCs (KOSTOPOULOS et al., 2003; KOSTOPOULOS; LOUTAS; DASSIOS, 2007; MOEVUS et al., 2008b; PAPPAS; MARKOPOULOS; KOSTOPOULOS, 1998). A combination of unsupervised and supervised learning, reviewing the accuracy of the methods, was also used before (TRIPATHI et al., 2019).

Meanwhile, supervised learning approaches can allow a higher specificity due to an already labeled dataset. As the input data is well known, the answers in the analysis and the output of the chosen algorithm are understood without difficulty (ALPAYDIN, 2007). If a dataset is made, based on the information obtained from mechanical tests which are easily correlated with a specific mechanism, a supervised learning algorithm can be helpful. This way, using signals that their source is known to belong to a specific damage mechanism, an output answer with higher accuracy may be obtained. However, creating a dataset with information respective to each mechanism can be complex. Thus, there is still a gap in the literature for works using only this approach.

2.4. MACHINE LEARNING MODEL EVALUATION

While creating a ML model capable of giving an expected output, certain actions need to be taken before involving the dataset used. Such actions are related to estimating the accuracy of a ML model, which is pivotal to verifying its performance (PEDREGOSA et al., 2011). Other than that, observing how the model learns the input data is also important to avoid problems such as overfitting and underfitting (AL-MASRI, 2019). The model performance can be estimated/measured based on the training set, using its skill score. For this, different methods can be used, such as holdout and k-fold cross validation (ALPAYDIN, 2007). The first splits the data into partitions of training and testing sets; the ratio of the partition can be changed. The second randomly divides the data into k "folds". The first fold is treated as a validation set, and the remaining folds are used to train the model. Each fold is allowed to be used in the hold-out set one time and to train the model "*k-1*" times (PEDREGOSA et al., 2011). Figure 10 illustrates how this validation method works. K-fold cross validation is usually the preferred method over holdout, as it allows the model to train on multiple train-test splits. This gives a better indication of how well the model performs on unseen data. Holdout, on the other hand, is dependent on

just one train-test split, which makes the skill score dependent on the ratio of the partition sets (BROWNLEE, 2019).

Figure 10 – Illustration of how k-fold cross validation works.

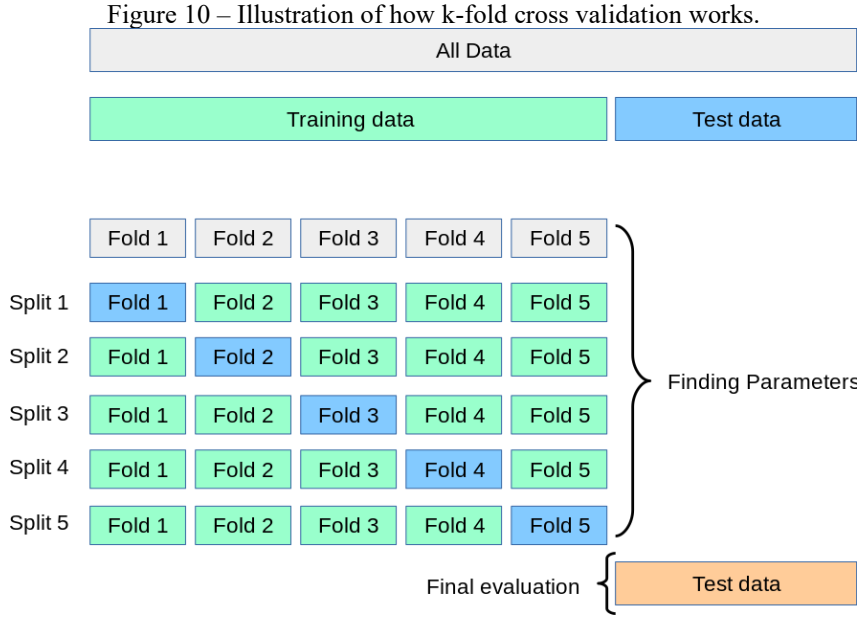

Source: PEDREGOSA et al. (2011)

Regarding how the data is learned, underfitting and overfitting should be highlighted, since they can show tendencies that do not exist. Underfitting happens when the model does not fit the training data nor generalize to new data. Overfitting occurs when the model fits exactly the training data (AL-MASRI, 2019). As an example, overfitting may be happening when a model scores a prediction of 90% for the training set, but 50% for a testing set. Because of that, the prediction of additional data can be compromised and not reliable. To avoid these problems, methodologies such as cross validation can be used (GOODFELLOW; BENGIO; COURVILLE, 2016). For understanding these problems, a simple linear regression model is used as an example below.

In Figure 11a, a model that fits well the data is illustrated. Even though that there are deviations from the datapoints, the line fits within the trend, making the model reliable to describe it, and perform generalization for new predictions (AL-MASRI, 2019). However, in cases where not enough data is available, or an adequate number of features to train the model is not chosen, overfitting and underfitting may occur. Overfitting is illustrated in Figure 11b, where a model which perfectly fits the data but does not follow a trend is seen. Underfitting is shown in Figure 11c. Here, a model that could not understand the relationship between the

datapoints during the training stage can be observed. In both cases, the model is not reliable for predicting new datapoints, i.e., cannot generalize for unseen events (AL-MASRI, 2019).

Figure 11 – Model fitting examples on a simple linear regression model.

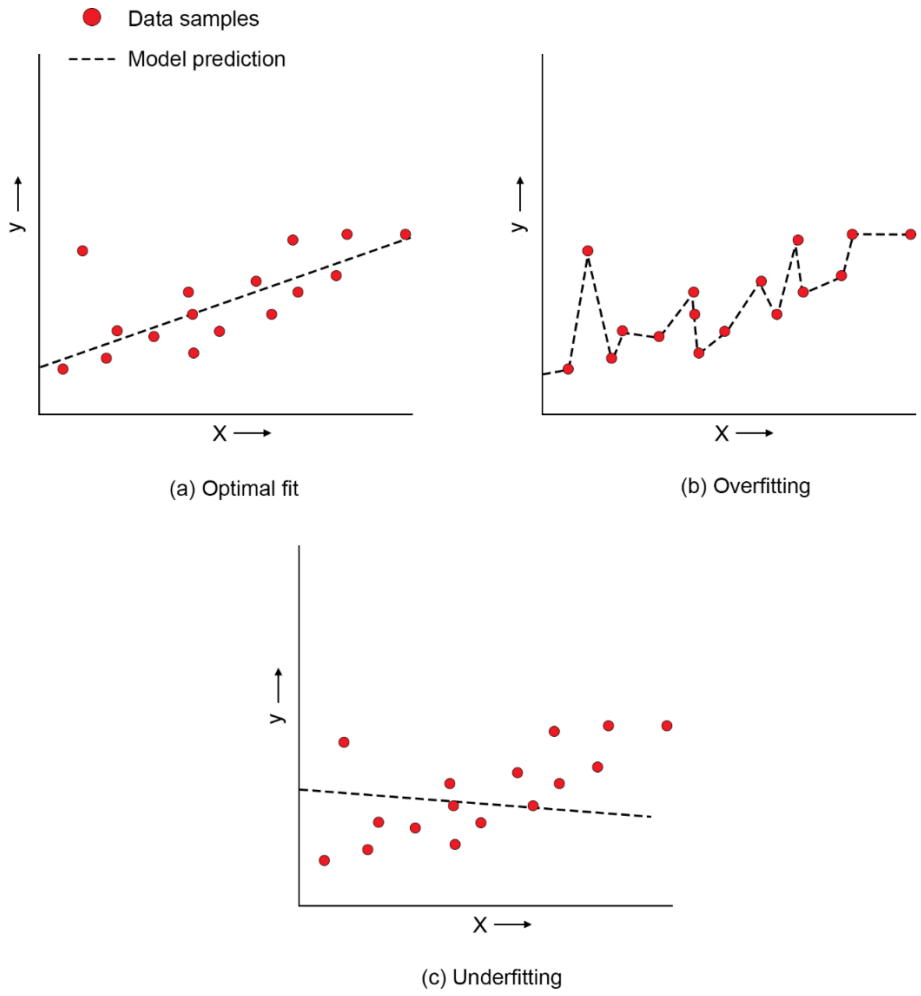

Source: Adapted from AL-MASRI (2019)

3. MATERIALS AND METHODS

Considering that this work is a collaboration between the Advanced Ceramics Group at Universität Bremen, and the Federal University of Santa Catarina (UFSC), the materials were manufactured and tested at the former, while the data was analyzed at both institutions.

During this project, different mechanical tests were conducted to gather data about the damage mechanisms of CMCs. Jointly to acoustic emission monitoring, those tests were able to give information about fiber break, matrix cracking, fiber pull-out, and interface debonding. For this step, Al_2O_3 fibers and matrices were used. The tests were performed in a way to obtain unique signals through acoustic emission analysis from each test. Next, the entire data was pre-processed and grouped to formulate the training dataset. The dataset was used to create a ML model for classifying the damage mechanisms of unseen data. The classified data was used to evaluate the damage development when a CMC is subjected to mechanical loads. Two sorts of composites were used to evaluate the damage development: Al_2O_{3f}/Al_2O_3 and C_f/SiC. The first is from the same base material used to assemble the training dataset. Thus, enables the evaluation of the model performance for the same material. The second act in a way to assess the model's response to other CMCs. In the following sections, a description of the experiments is made, and the methodologies used are explained.

3.1. MATERIALS

3.1.1. Nextel 610 Ceramic Fibers

Two different configurations of the Nextel 610 fibers were used. One was a unidirectional strand with 3000 denier, corresponding to 750 fiber filaments in each bundle. It was used for producing single filament, 10-filament, fiber bundle, fiber pull-out, and minicomposite samples. The former three are samples where only fibers were used, while the latter two are obtained by combining the Al_2O_3 fibers in an Al_2O_3 matrix. The second configuration was the Nextel 610 fiber fabric commercially known as DF-11, applied to produce composite plates. This fabric has a denier of 1500 (400 filaments each) and is weaved in an 8 harness-satin configuration. This configuration is shown in Figure 12, which involves a

warp yarn (runs lengthwise) passing under 7 fill yarn (runs crosswise) and repeating. The fill yarn does the same with the warp yarn.

Figure 12 – Representation of fabric 8-harness satin configuration.

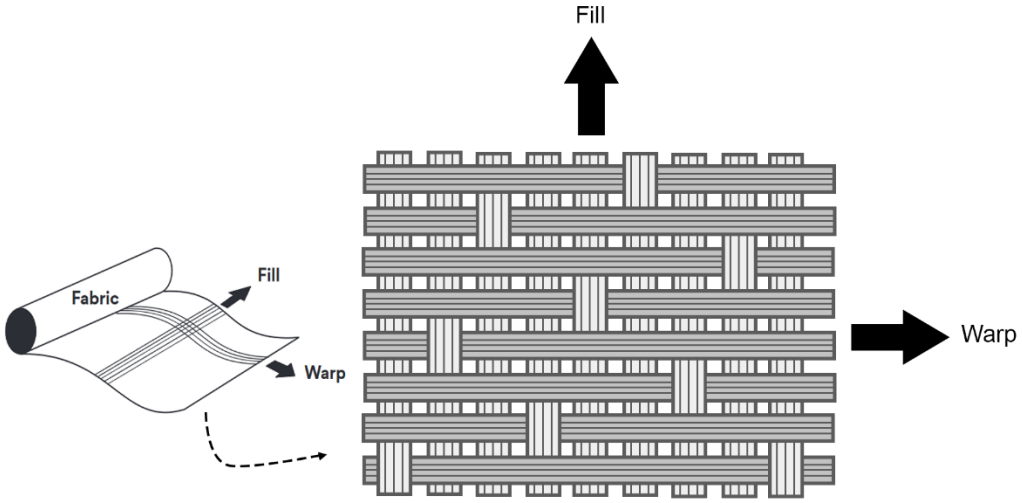

Source: author

These alumina fibers are commonly utilized for producing Ox-CMC components for industrial purposes. Each fiber filament has a diameter ranging from 11-13 μm (3M COMPANY, 2021). Regarding their applications, it is popularly used as a structural grade fiber, designed for load-bearing components because of their high strength and modulus. It should be noted that these fibers have a fine-grained (<500 nm) single-phase microstructure, with the composition of α-Al_2O_3, illustrated in Figure 13. Their key physical properties, as well as the manufacturing process, are shown in Table 3.

Figure 13 – SEM image of Nextel 610 fiber showing the small grain size microstructure.

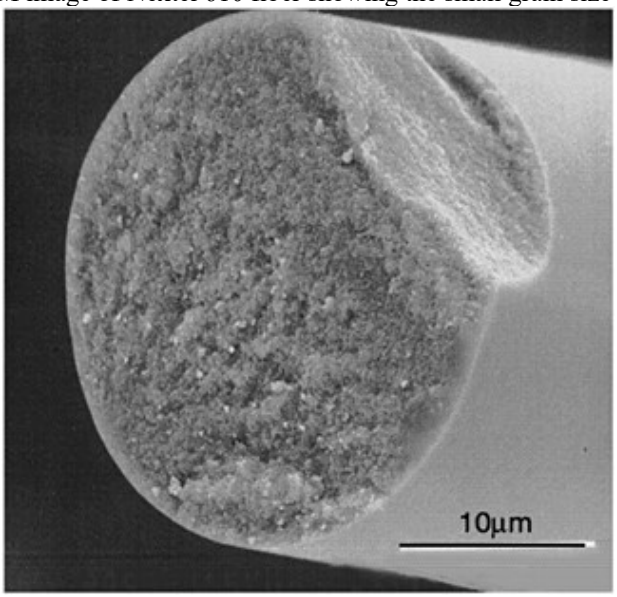

Source: 3M Company

Table 3 – Physical properties of Nextel 610 fiber.

Property	Nextel 610
Density (g/cm³)	3.9
Tensile Strength (MPa)	2800
Elastic Modulus (GPa)	370
Manufacturing Process	Sol-Gel
Composition (%)	>99 Al_2O_3

Source: 3M COMPANY (2021)

To provide better environment resistance and assist in handling, the as-received fibers come with polymeric sizing composed of polyvinyl alcohol (PVA) and additives such as plasticizers and lubricants (3M COMPANY, 2021). Thus, before the material can be used for samples preparation, eliminating the sizing is needed. For this, the Nextel 610 fibers were heated up to 700ºC in an oven for 2 hours. The heating and cooling rates used were of 100ºC/hour and 300ºC/hour, respectively.

3.1.2. Al_2O_3 Matrix

The Al_2O_3 ceramic matrices were fabricated for several samples: matrix, fiber pull-out, minicomposites, and composite plates. All Al_2O_3 samples were produced with the same slurry composition and parameters described below. The differences between the samples (matrix and composites) are on the specific casting steps.

The matrix produced is based on a water-based slurry using alginate polymeric binders. For producing it, the ionotropic gelation method was used. This method is based on the ability of metallic cations to interact with polysaccharide chains. When containing such polysaccharide chains, the ceramic suspension can be slowly gelled with the addition of metallic ions that start a cross-link reaction. In the meantime, the green body can be shaped until complete consolidation (ALMEIDA et al., 2019a).

For the matrix consolidation, two types of alginates (polysaccharides) were used to get a better viscosity: Protanal LFR5/60 (FMC Corporation, Philadelphia, PA, USA) and Alginic acid sodium salt from brown algae (Sigma-Aldrich Chemie GmbH, Steinheim, Germany). When dissolved in water, the alginates form reticulated chains. These chains are responsible for the later gelation of the green body. Using an overhead stirrer RW20DZN.n (IKA®-Werke GmbH KG, Staufen, Germany), both alginates were dissolved into demineralized water with pH adjusted to 9 and stirred in an ice-water bath at 300 rpm for 30 minutes. The pH was adjusted with the addition of an NH_4OH solution (25% NH_3 in H_2O). This is done to get higher stability of the ceramic particles in the suspension and better interaction with the alginate chains. Afterward, two alumina ceramic powders were incorporated into the suspension, CT1200 (d_{50} = 1200 nm; Almatis GmbH, Ludwigshafen, Germany) and TM-Dar (d_{50} = 200 nm; Taimed Chemicals, Tokyo, Japan). To avoid agglomeration, 5-sulfosalicylic acid dehydrate ReagentPlus® (Sigma-Aldrich Chemie GmbH) was used as the dispersant. The mixture was stirred for 1 hour at 1500 rpm. In the end, the slurry was stored in a refrigerator at approximately 5 ºC for at least 24 hours. The quantity of raw materials used to obtain the slurry is shown in Table 4.

Table 4 – Quantity of materials used to obtain the slurry.

Material	Quantity
Water (mL)	45
NH_4OH (mL)	5
FMC-BIO Alginate (g)	0.6
Sigma Low Brown Alginate (g)	0.6
CT1200 (g)	135.5
TM-Dar (g)	58
5-sulfosalicylic acid dehydrate (g)	1

Source: author

After 24 hours, the slurry was transferred to a mixer device Dispermat LC2 (VMA-GETZMANN GmbH, Germany) with a vacuum chamber. The slurry was stirred at low pressure (60~100 mbar) for 5 minutes at 2000 rpm. Following, aluminum acetate (Honeywell Specialty Chemicals Seelze GmbH, Seelze, Germany) was added in the amount equivalent to 0.3 wt% of the suspension. The mixture was stirred once again at low pressures for 10 seconds at 6000 rpm. The goal of the aluminum acetate is to release Al^{3+} ions and start the cross-link reaction with the alginate chains.

After cross-linking, sample's assembling was possible. As already raised, four sorts of samples used the water-based slurry: matrix, fiber pull-out, minicomposites, and composite plates. Because the latter three were obtained by infiltrating the Al_2O_3 fibers with the slurry. Before the infiltration (permeation of the fibers with the slurry), the Nextel 610 fibers were placed on a Femto low-pressure plasma system (Diener Electronics) to perform oxygen plasma deposition over them. Then, the samples were assembled. The O_2 atoms on the surface of the fibers are expected to increase the wettability of the fibers by decreasing the contact angle. Hence, this procedure has the purpose to improve the fiber-slurry infiltration. For the device parameters, a gas pressure between 2-4 mbar, power of 50 watts, and a dwell time of 2 minutes were used. The equipment is shown in Figure 14.

Figure 14 – Plasma surface treatment performed on fibers of composite samples.

Source: author

Regarding the differences in casting for each sample type, matrix samples were produced using rectangular shape molds. For this sample, the molds were filled with slurry and put on a climate chamber at 50ºC and 80% humidity for 1 hour. This allows an increased crosslinking rate of the slurry due to the temperature while avoiding fast drying because of the humidity. In the case of fiber pull-out, the slurry was placed in cylindrical molds to obtain the matrix part of the composite. Then, infiltrated fiber bundles were inserted into the filled mold. For minicomposites, infiltrated fiber bundles were fitted inside paper tubes, which were used to give the sample a cylindrical shape. Lastly, composite plates were produced by stacking infiltrated ceramic fabric layers above each other. The specific steps for the sample's assembling are explained in section 3.2.

After assembling, all samples were put in a climate chamber for 48 hours at 20 ºC and 80% humidity, followed by 24 hours at room temperature for drying. Then, samples were sintered in a high-temperature chamber furnace LHT 04/17 (Nabertherm GmbH, Lilienthal, Germany). The samples were sintered at 1200ºC with 1 hour of dwell time. A heating rate of 100ºC/hour and a cooling rate of 300ºC/hour was used. The main steps for slurry preparation and sample's obtaining are illustrated in a flowchart format in Figure 15.

Figure 15 – Flowchart exhibiting the main steps and materials necessary for preparing the water-based slurry, followed by samples obtention.

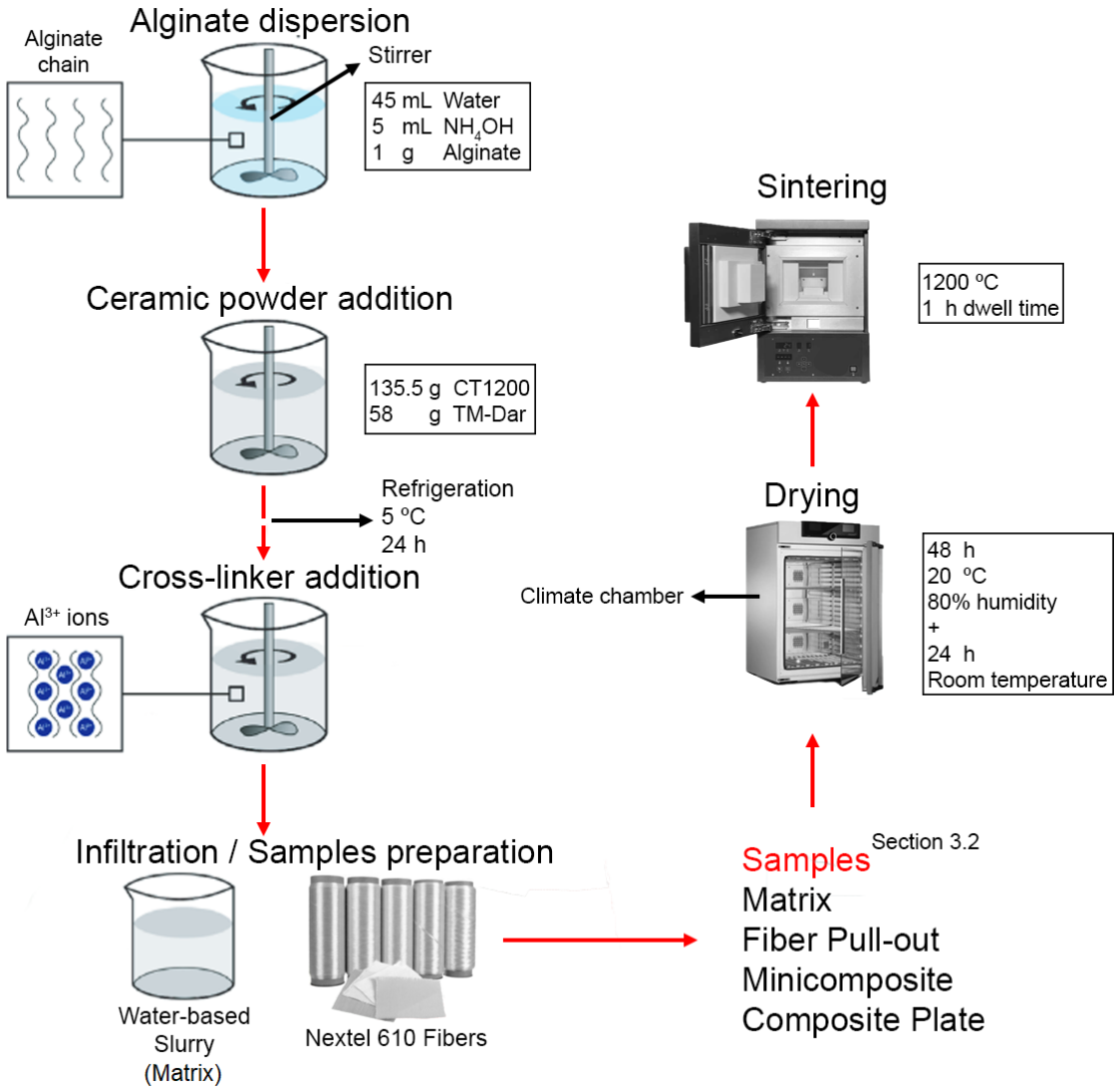

Source: Adapted from ALMEIDA et al. (2019a, p. 55)

3.1.3. C_f/SiC Composites

Carbon fiber reinforced silicon carbide composites were selected to further assess the model behavior. It should be highlighted that these samples were not produced nor tested within this master's thesis. The samples were produced at the Powder Metallurgy Research Institute (Central South University, China), and were analyzed at the Advanced Ceramics Group (Universität Bremen, Germany). The results were published in an article by Almeida et al. (2019b), and the AE data measured was utilized here for quantifying the damage mechanisms.

The composites in question used a 2.5-dimensional carbon fiber preform in a silicon carbide matrix (2.5D C_f/SiC) to obtain composite plates. The geometrical architecture of these fibers is the reason these composites are known as 2.5D. The manufacturing process is described in a previous work by Almeida et al. (2019b). First, the fiber preform was prepared by stacking short-cut fiber webs (non-woven) and unidirectional fiber cloths that are later needle-punched together. The fibers used were polyacrylonitrile-based carbon fibers T700G with a filament count of 12k. These fibers have a filament diameter of 7 μm, used for applications such as aircrafts and high-performance sports applications (TORAY INDUSTRIES, 2018). A schematic representation of the fiber preform is shown in Figure 16. The physical properties of the fiber are shown in Table 5.

Figure 16 – Schematic representation of the 2.5D reinforcement preform.

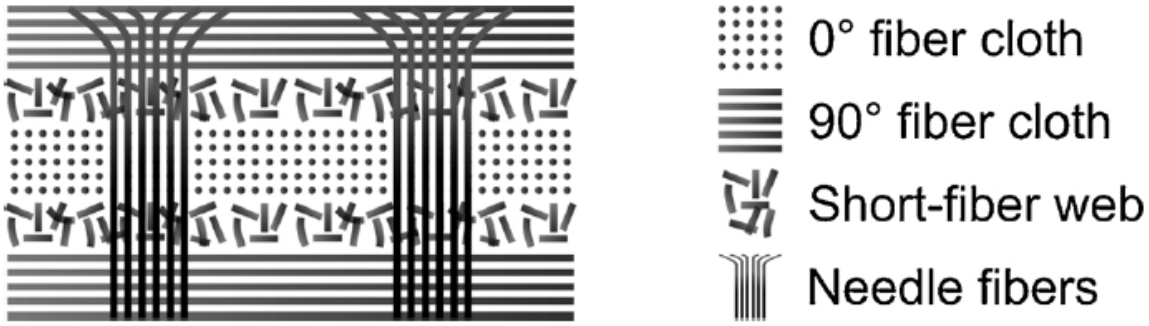

Source: ALMEIDA et al. (2019b, p. 2245)

Table 5 – Physical properties of T700G fiber.

Property	T700G
Density (g/cm³)	1.8
Tensile Strength (MPa)	4900
Elastic Modulus (GPa)	240
Manufacturing Process	Sol-Gel
Composition (%)	>99 Al_2O_3

Source: TORAY INDUSTRIES (2018)

Following, a porous C/C composite was made through chemical vapor infiltration (CVI) on the 2.5D fiber preforms. The CVI process parameters were temperature of 1000 ºC, with a dwell time of 100 h and absolute pressure of 0.1 MPa under argon atmosphere. The precursor used was C_3H_6. H_2 was applied as a carrier and diluting gas. For obtaining the 2.5D

C_f/SiC composite, the porous C/C composite was impregnated via liquid silicon infiltration (LSI) for further densification. The LSI process was performed at 1650 ºC, with a dwell time of 0.5 h under vacuum with absolute pressure < 1 Pa. The main steps for obtaining the C_f/SiC composites are shown in the flowchart of Figure 17.

Figure 17 – Flowchart exhibiting the main steps necessary for preparing the Cf/SiC composites.

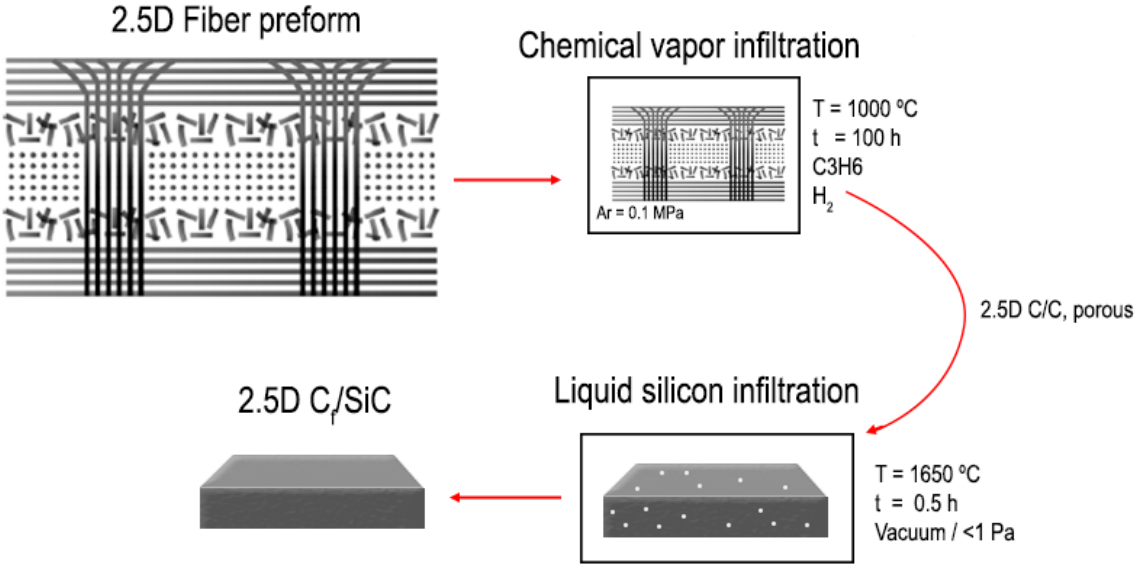

Source: Adapted from Almeida et al. (2019b)

3.2. SAMPLE PREPARATION AND CHARACTERIZATION

To fully characterize the CMC and collect data from its damage mechanisms, mechanical tests were performed jointly to acoustic emission monitoring. At first, tensile tests on Nextel 610 fibers were executed to obtain fiber break signals. Later, 4-point bending tests and single-edge notched bending tests (SENB) were performed in matrix samples, enabling the recording of matrix crack signals. Then, fiber pull-out signals were obtained through fiber pull-out tensile tests. For recording interface debonding signals, short-beam bending tests (SBB) were performed on composite plates. For testing the classification performance of the ML model, tensile and 4-point bending tests were performed on Al_2O_3 minicomposites and composite plates, respectively. Additionally, the AE data measured by Almeida et al. (2019b) from C_f/SiC that undergone tensile tests was also used for this intent. Each of the tests

conducted, and their purposes are represented in Figure 18. The samples are divided into two categories, pre-tests, and final tests. The first was used to acquire the specific damage mechanisms signals with AE, while the second was to test the ML model classification.

Figure 18 – Flowchart of the sample's characterization, highlighting the mechanical tests and expected information to be obtained from recorded acoustic emission signals. Pre-test samples are used for formulating the training dataset by measuring the AE signals from each sample. Final test samples are used to perform the model evaluation.

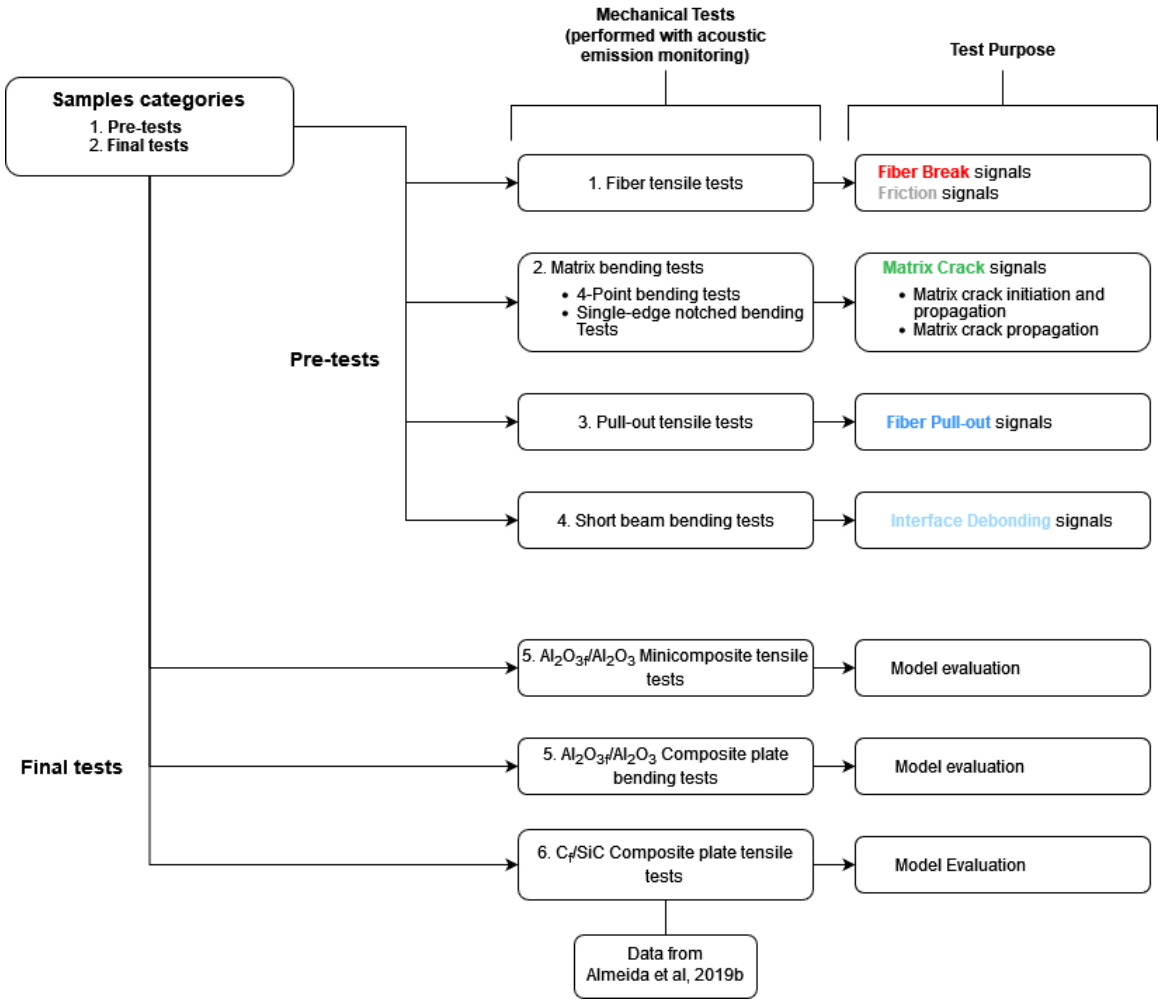

Source: author

3.2.1. Fiber Samples

The fiber samples were subjected to tensile tests on a universal testing machine model Zwick Z005 (ZwickRoell GmbH & Co. KG, Erbach, Germany), capable of loading through tensile, compression, and torsion modes, with a load cell of 5 kN. To prepare the samples for

testing, the desized fibers were glued with a two-component epoxy glue UHU Plus Endfest (UHU Vertrieb GmbH, Bühl, Germany) to a paper frame, which is used for stability of the fibers and better grip on the tensile testing machine. Figure 19 exemplifies the paper frame used to hold the fibers.

Figure 19 – Illustration of the paper frame used for fiber tensile tests.

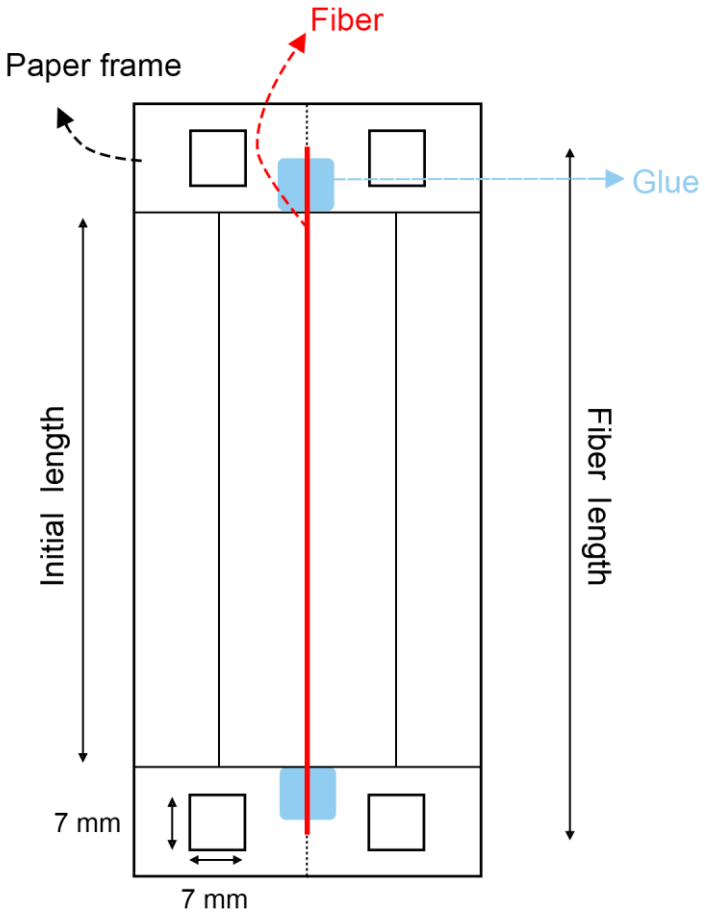

Source: author.

Different sample sizes were tested. Recorded signals are based on the acoustic wave that propagates in the material; meaning that this acoustic wave travels inside the material to the surface from the point that it was generated. Hence, the sample dimension may change the signal parameters acquired, as the travel distance of the signal changes. So, two different initial length samples were used to acquire a broader range of AE signals: 25 mm and 70 mm. Bundle, single filament, and 10-filaments fiber tensile tests were conducted for each size. It should be noted that, for single and 10-filament fiber tests, a much smaller quantity of material is tested if compared to the bundle tests. Therefore, fewer AE signals are recorded, which are only

related to fiber break signals. Later, during bundle tests, the information obtained provided means to differentiate fiber break signals from others that may be recorded, such as friction between the fibers.

For the bundle tests, the entire bundle was glued to the paper frames. As for the single and 10-filaments fiber tests, each fiber was glued to the paper frame one by one. To ensure that the data acquired was reliable, the numbers of samples tested were as suggested by the standard DIN EN 1007-5 (2004) for bundle tests and DIN EN 1007-4 (2003) for single-filament tests and are shown in Table 6.

Table 6 – Number of fiber samples tested for each size.

Number of Samples	25 mm	70 mm
Bundle	5	5
Single Filament	20	20
10-filaments	5	5

Source: author

Upon sample preparation, each sample was placed on the tensile testing machine, where the frames used to hold the fibers were clamped between metal plates and secured with screws. The acoustic emission sensors were placed on both ends of the metal plates. Following, the paper frame was cut on both sides, ensuring that the fiber was the one being tested during the data acquisition. The tensile tests were carried out with a travel speed of 0.1 mm/min. The sample ready for the test can be seen in Figure 20.

Figure 20 – Example of bundle fibers ready for testing.

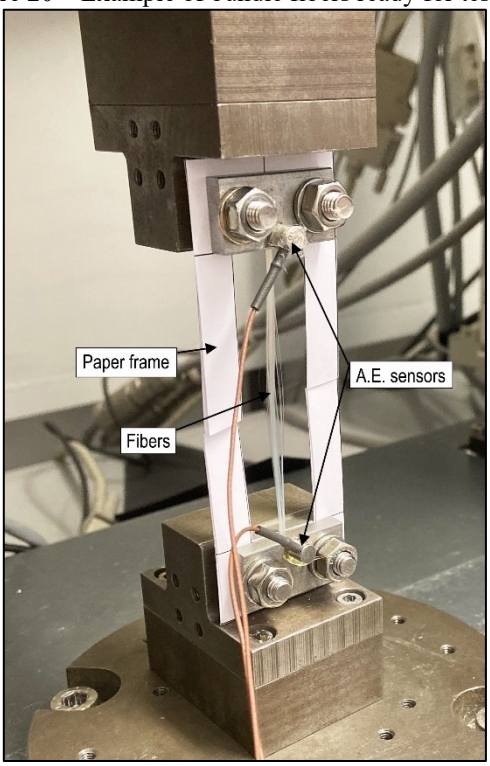

Source: author

.

For calculating the stress, the following equation can be used:

$$\sigma = \frac{F}{A} \tag{3.1}$$

For the area determination, a simple approach relating the density of the material was used:

$$A = \frac{m}{\rho\, l} \tag{3.2}$$

So

$$\sigma = \frac{F\rho l}{m} \tag{3.3}$$

To calculate the stress of single filament tests, the following equation was used. The diameter value used was based on values used for previous works, corresponding to 12.55 µm.

$$\sigma = \frac{F}{A} = \frac{4F}{\pi D^2} \tag{3.4}$$

While for 10-filament, the area is multiplied by 10:

$$\sigma = \frac{F}{10A} = \frac{2F}{5\pi D^2} \tag{3.5}$$

Where σ is the specific stress, A is the initial area of the sample material, F is the force applied to the sample, ρ is the density of the material, l is the total length of the sample, m is the total mass of the sample, and D is the diameter of the fiber filament.

3.2.2. Matrix Samples

Matrix samples were tested using 4-point bending tests and SENB tests. While the first was used to measure matrix crack initiation and propagation signals, the latter was used to simulate just the crack propagation. For the same reason as fiber samples, two different sizes of matrix samples were produced. The dimensions for each size were approximately 45 x 4 x 3 mm and 70 x 6 x 5 mm. For performing the SENB tests, the notch size made corresponds to a third of the sample width, following the DIN EN ISO-15732 (2004) guidelines. The samples are illustrated in Figure 21.

Figure 21 – Matrix bending test samples: a) unnotched samples and b) notched samples.

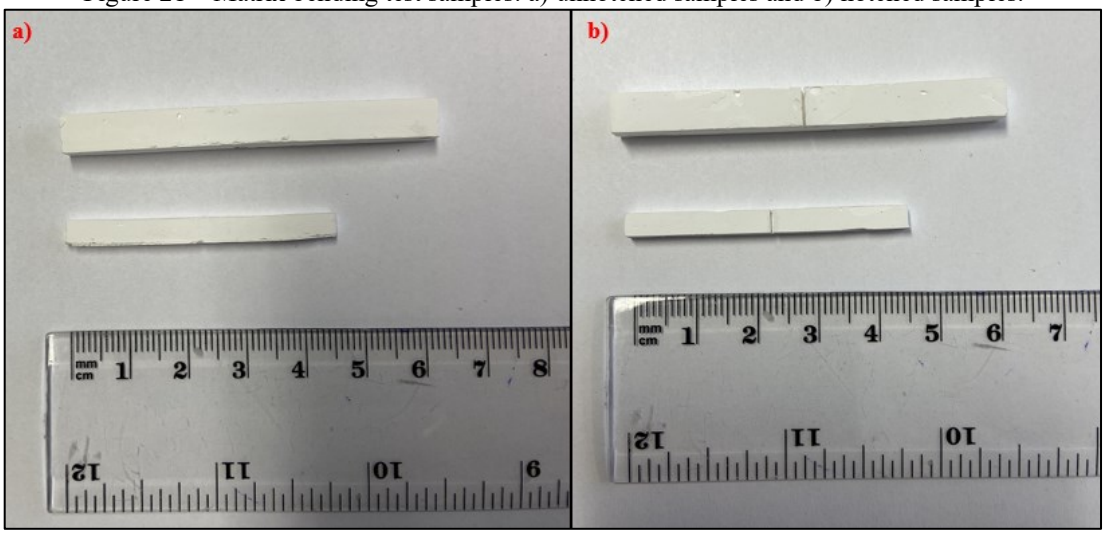

Source: author

The bending tests were performed according to the standard DIN EN 843-1 (2008) on the universal testing machine model Zwick Z005. As for the number of tests, 20 samples were evaluated for each type of test and sample size. The distance between the outer spans was 40 mm and 60 mm for the smaller and bigger samples, respectively, while the inner span distance was 20 mm for both. Before starting the test, a pre-load of 5 N was applied. Test traveling speed used was 0.5 mm/min. For the acoustic emission evaluation, the piezoelectric sensors were fixated on each end of the samples. A matrix sample placed on the testing setup is shown in Figure 22.

Figure 22 – Matrix 4-point bending test set-up.

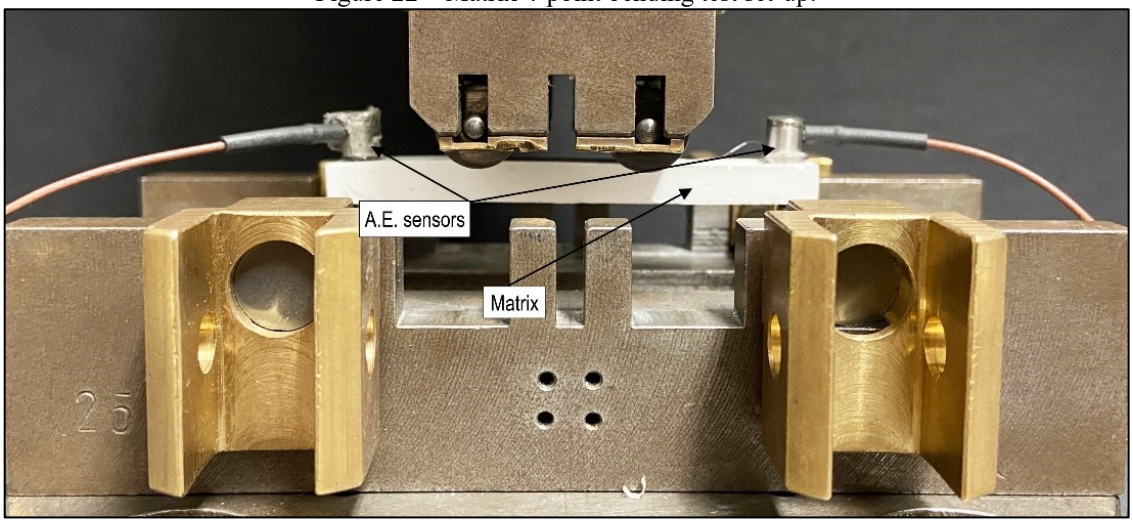

Source: author

To evaluate the flexural strength of the 4-point bending test, the following equations were used:

When the lengths of the inner and outer span (L_i and L respectively) are $L_i = 1/2L$, which is the case for the shorter samples:

$$\sigma = \frac{3FL}{4wb^2} \tag{3.6}$$

On the case of the longer samples, where $L_i = 1/3L$:

$$\sigma = \frac{3FL}{wb^2} \tag{3.7}$$

Where F is break force, L is the outer (support) span distance, w is the sample width, and b is the sample thickness.

For measuring the fracture toughness (K_{IC}) of the notched matrix samples, the equation is as follows:

$$K_{1C} = \frac{F}{b\sqrt{w}}Y \tag{3.8}$$

Where Y is the geometrical factor, which is calculated using the following equation:

$$\mathrm{Y} = \frac{\mathrm{L}-1}{\mathrm{w}} * \frac{3\sqrt{\propto}}{2(1-\propto)^{\frac{3}{2}}}[1.9887 - 1.326 \propto - \frac{(3.49 - 0.68 \propto + 1.35 \propto^2) \propto (1-\propto)}{(1+\propto)^2} \tag{3.9}$$

Being $\propto$ the relative notch length, given by the ratio between the notch length (a) and the sample width (w).

$$\propto = \frac{\mathrm{a}}{\mathrm{w}} \tag{3.10}$$

3.2.3. Fiber Pull-out Samples

To assemble the fiber pull-out samples, first the fiber bundles cut with a length of approximately 150 mm were fitted into paper tubes of 75 mm in length. Just half of the bundle length was infiltrated with the alumina slurry, leaving the other end of the sample free. Following, the fiber bundle infiltrated part was cut so that only 3 mm was infiltrated. Then, the infiltrated portion was inserted into cylindrical shape molds filled with slurry. Only the infiltrated part is combined with the matrix to ensure that the signal source obtained from the test is from fiber pull-out. If the length of fibers that are inside the matrix is too long, the fibers may break first. Figure 23 illustrates the fiber pull-out sample.

Figure 23 – Fiber pull-out test sample.

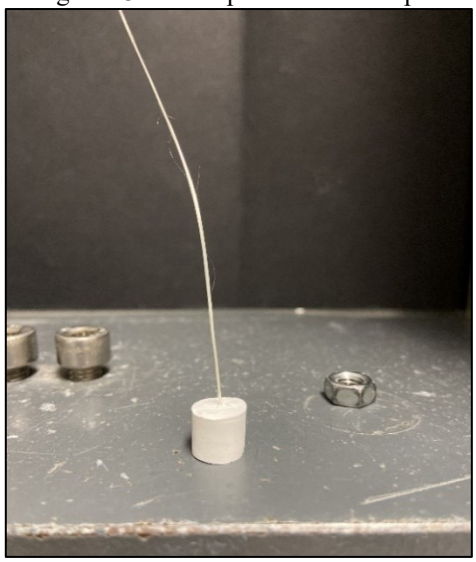

Source: author

After preparing the fiber pull-out samples, uniaxial tensile tests were performed. The equipment used was a universal testing machine model Zwick Z005. A traveling speed of 0.1 mm/min was used for testing. To prepare the test setup, the exposed fibers were passed through the hole of a metal lid, which held the infiltrated part of the fibers in place. Then, the fibers were glued to a paper frame using a two-component epoxy glue from UHU Plus Endfest (UHU Vertrieb GmbH, Bühl, Germany). Subsequently, the metal lid was fixated on the testing machine. The matrix was locked in the lower part of the metal lid, ensuring that the fibers were the ones being stressed and pulled. A metal plate clamped the paper frame and secured the exposed fiber bundle. The acoustic emission sensors were placed on the metal plate and the top

of the metal lid. However, just signals recorded from the metal plate sensor were used. The metal lid surface was not directly in contact with the fibers being pulled. Because of that, the AE sensor could record signals that were not related to fiber pull-out, e.g., the matrix being pulled against the lid and cracking. To acquire enough signals from the fiber pull-out mechanism, 14 samples were tested. Figure 24 illustrates the sample being prepared on the left, and the setup to perform the tests on the right.

Figure 24 – Sample preparation (left) and pull-out test setup (right).

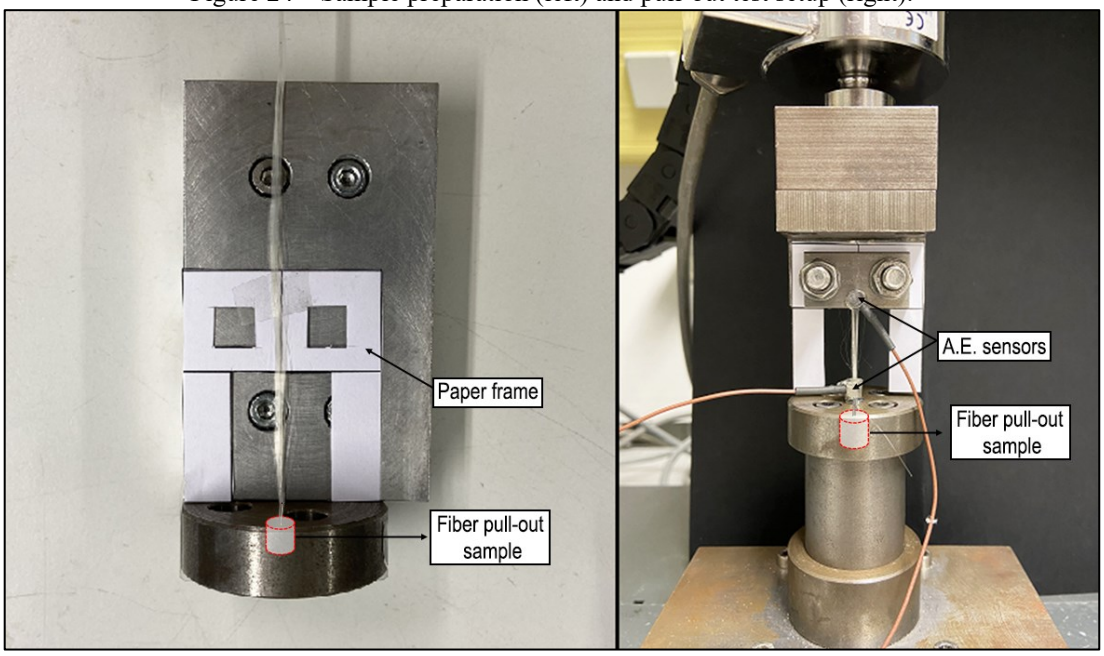

Source: author

For evaluating the pull-out shear stress, considering the case of a single filament fiber pull-out:

$$\tau = \frac{F}{A} = \frac{F}{h\pi D} \tag{3.11}$$

As the tests were performed utilizing Nextel 610 fiber bundles with a dernier of 3000, containing 750 filaments. The equation is modified to:

$$\tau_b = \frac{F}{750h\pi D} \tag{3.12}$$

Where F is the break force, A is the initial area of the sample material being tested, h is the height of the fibers inserted in the matrix, and D is the fiber diameter.

It should be noted that h is the height at which the fibers are inserted inside the matrix part. As h was not measured, but estimated during the sample preparation, its value is prone to variations between samples. Hence, the shear stress should be used just as a reference.

3.2.4. Al_2O_{3f}/Al_2O_3 Minicomposite Samples

To assemble the minicomposite samples, fiber bundles were cut into segments of 300 mm in length. Six bundles were used to achieve an approximate fiber content of approximately 20 vol%. The bundles were inserted into a paper tube of approximately 150 mm in length and 1.8 mm in diameter and fixed in place using adhesive tape (Figure 25).

Figure 25 – Minicomposite sample preparation. In this step, fibers were being prepared for plasma deposition previous to the slurry infiltration.

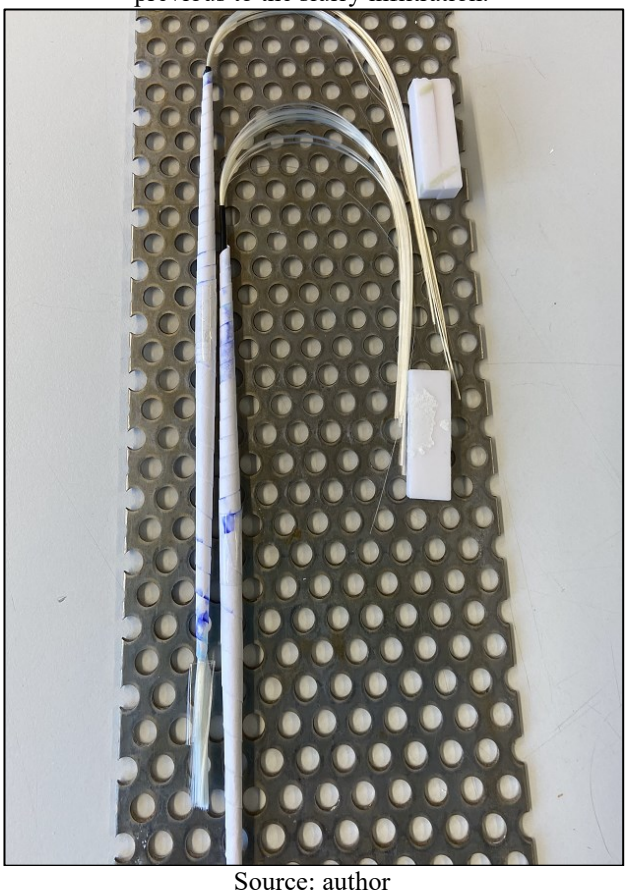

Source: author

Then, fibers were infiltrated over a plastic sheet. The infiltrated fibers were pulled through the paper tube mold so that a cylindrical shape could be acquired. The sample prior to sintering is shown in Figure 26.

Figure 26 – Minicomposite sample before sintering.

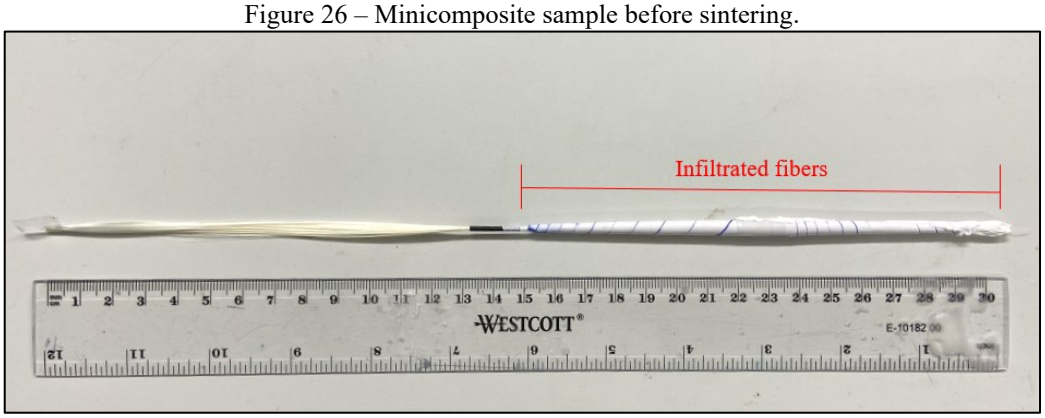

Source: author

After obtaining the sintered samples, the non-infiltrated segment of the composite was cut out using a diamond wire cutting machine model 6234 (Well Diamantdrahtsägen GmbH, Mannheim, Germany). Conical plastic holders were then glued on each end of the sample (Figure 27) to attach the samples to the testing machine. This holder geometry is used so that the sample fails in the area of interest and not on its edges during the mechanical test. The glue used was X60 Schnellklebtoff and the curing time was 60 minutes.

Figure 27 – Minicomposite samples ready for testing

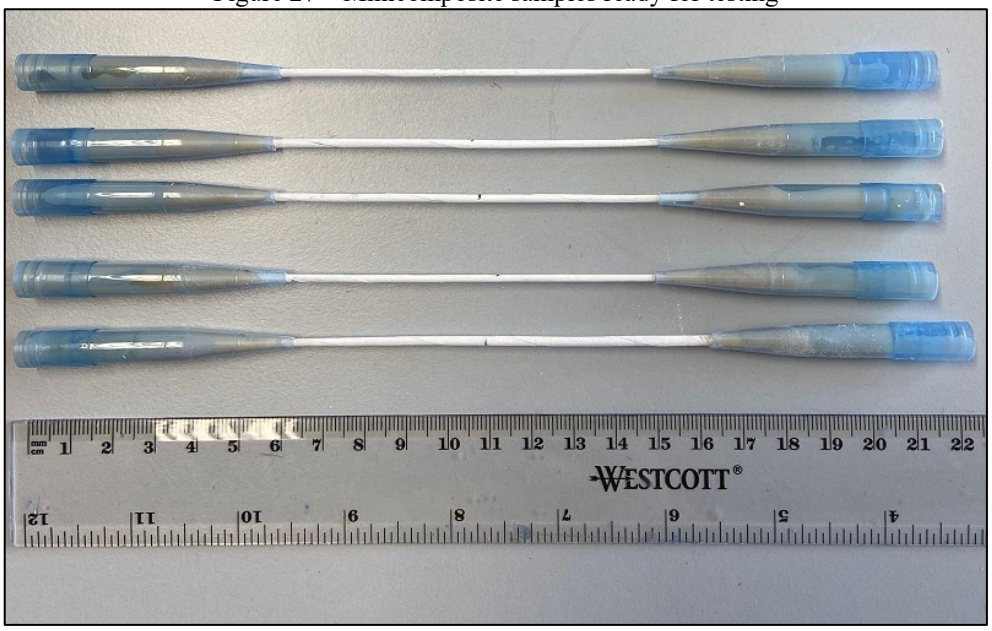

Source: author

Uniaxial tensile tests were performed on the minicomposites samples, because of the orientation of the fibers. Five samples were evaluated. The equipment used was a universal testing machine model Zwick 1474 (ZwickRoell GmbH & Co. KG, Erbach, Germany). The deformation during testing was acquired by a laser extensometer (Fiedler Optoeletktrik GmbH, Lützen, Germany). Two black strips were marked on the samples 25 mm apart lengthwise. For testing, samples were fixed on the equipment along with the acoustic emission sensors (Figure 28). A travel speed of 1 mm/min and a pre-load of 10 N were set.

Figure 28 – Minicomposite tensile test setup.

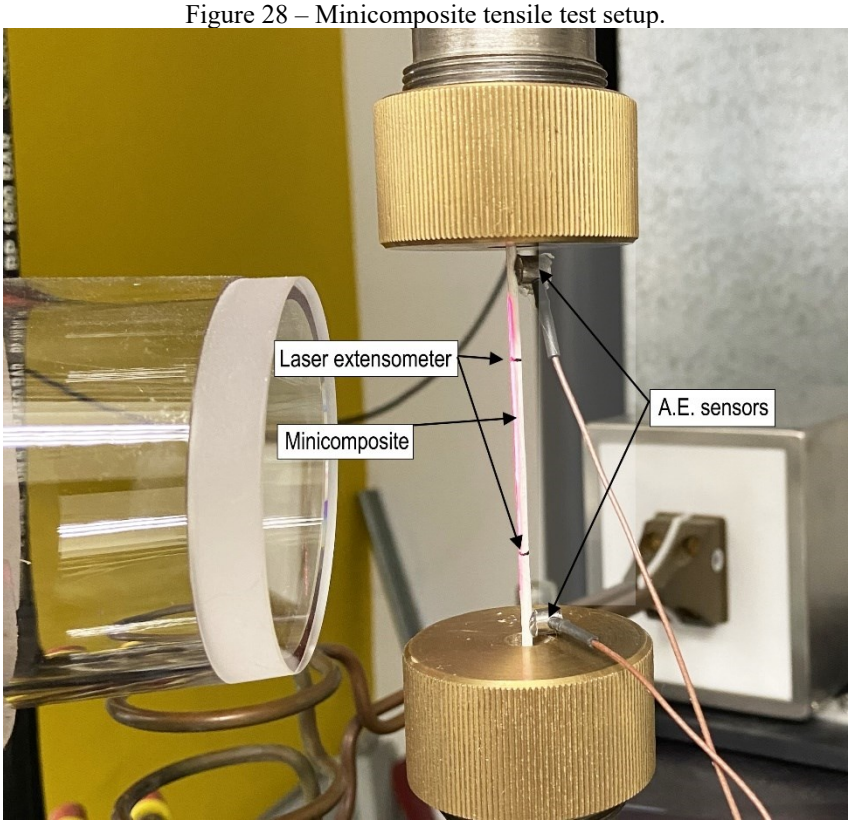

Source: author

The tensile strength of the minicomposites is calculated by dividing the force by the sample area, as follows:

$$\sigma = \frac{F}{A} = \frac{4F}{\pi D^2} \tag{3.13}$$

Where σ is the specific stress, F is the force applied to the sample, A is the initial area of the sample material being tested, and D is the diameter of the sample.

3.2.5. Al_2O_{3f}/Al_2O_3 Composite Plate Samples

For the characterization of composite plates, two different tests were conducted: SBB and 4-point bending tests. The first was used as a pre-test for measuring the interface debonding signals. The second was used for evaluating the ML model, classifying the signals obtained from this test.

For preparing the 2-dimensional fiber-reinforced composite plates, Nextel 610 fiber fabrics DF-11 were used. To obtain the composites, the desized ceramic fabrics, cut with the dimensions of 60 X 90 mm, were infiltrated with slurry over Teflon sheets (Figure 29).

Figure 29 – Infiltration steps done on ceramic fabrics.

Source: author

The Teflon sheets were sealed with tape and rolled between two metallic rolls, making sure that the fabrics were well infiltrated. Next, the sheets were opened, removing the fabrics and stacking them above each other. Twelve and four stacks' samples were produced. The one with a higher number of stacks was destined for the SBB tests, while the other for 4-point bending tests. The number of specimens was 10 for each test.

Sintered samples were cut using a diamond disk saw CUTO 1 (Jean Wirtz, Dusseldorf, Germany). The respective dimensions of the four and twelve stack samples were approximately 70 X 10 X 1.7 mm and 30 X 10 X 5 mm. Both are shown in Figure 30.

Figure 30 – Composite plate samples for 4-point bending tests (left) short-beam bending tests (right).

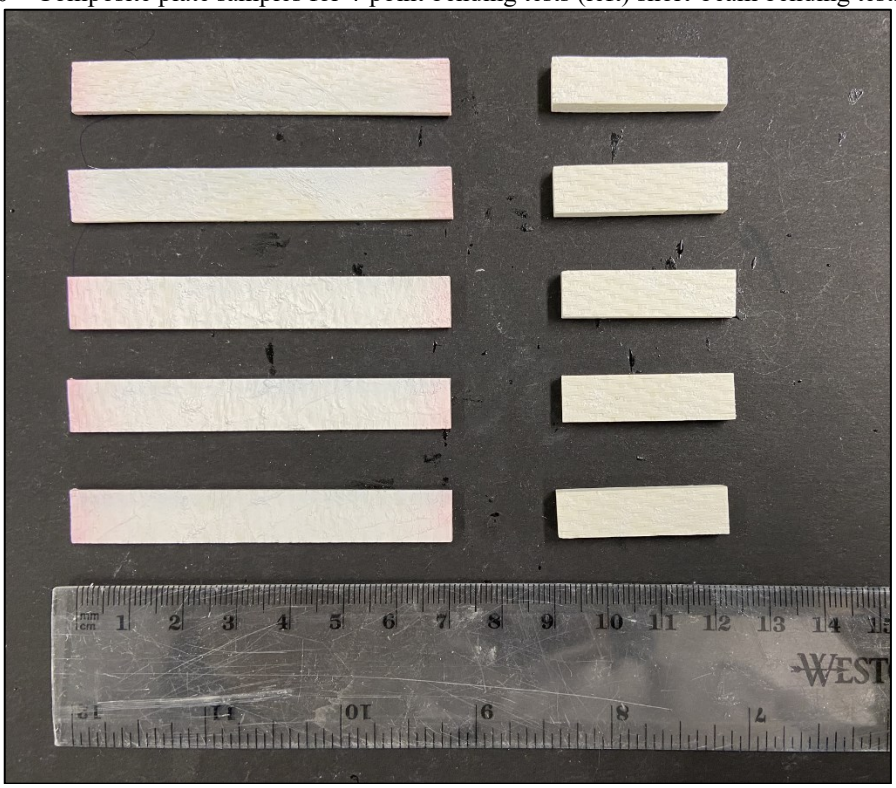

Source: author

Characterization was done differently for each sample. Samples destined for pre-tests had their interlaminar shear strength measured by SBB test configuration (standard DIN EN 658-5, 2002). The tests were performed using an outer span distance of 25 mm. The objective of this test was to promote shear stresses on the sample to delaminate its layers. As a result, interface debonding signals are expected to be recorded by AE monitoring. The bending strength of composite plates, intended to serve as final tests, was measured by a 4-point bending test (standard DIN EN 658-3, 2002). The outer and inner span distances were 60 mm and 20 mm, respectively.

The tests were conducted on the universal testing machine model Zwick Z005, where ten samples were tested for each bending test. The machine setup is shown in Figure 31, where the AE sensors were placed on both ends of the sample. A pre-load of 5 N and a test speed of 0.5 mm/min were used.

Figure 31 – Composite plate test set-up for 4-point bending test (left) and short-beam bending test (right).

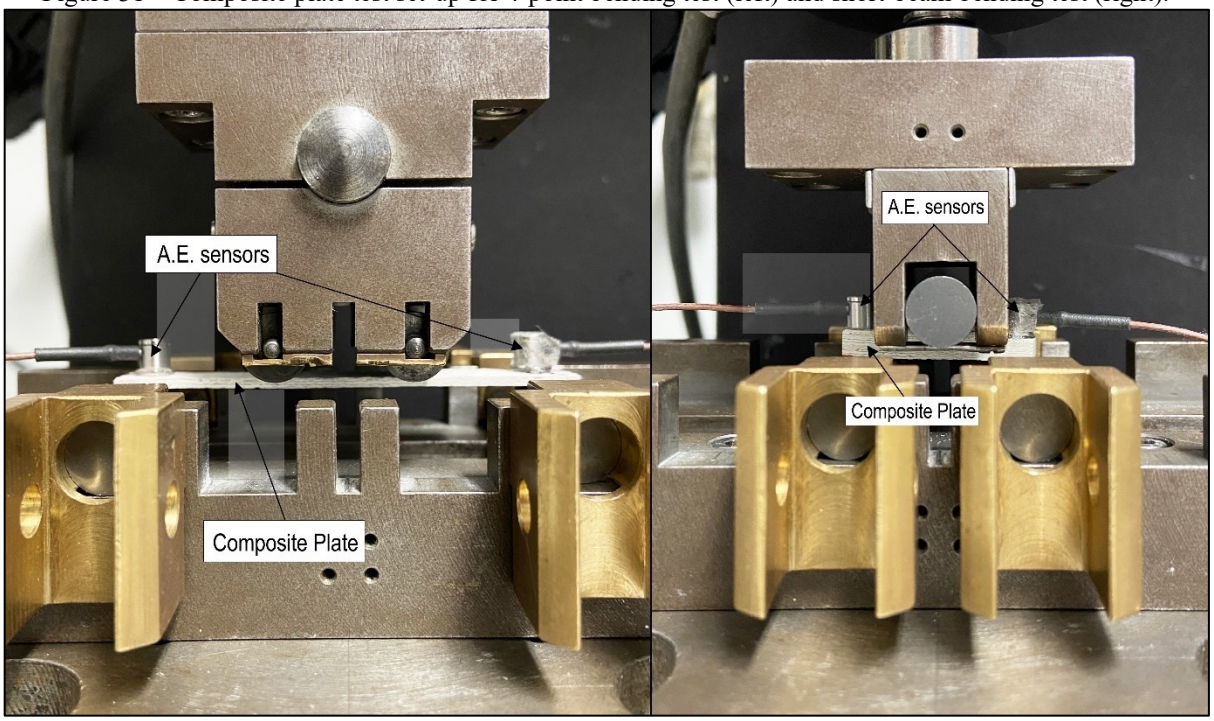

Source: author

For calculating the flexural strength of 4-point bending test samples, equation 3.7 shown in subsection 3.2.2 was used. For the short-beam bending test, the shear stress is calculated accordingly to the following equation:

$$\tau = \frac{3F}{4wb} \tag{3.14}$$

Where F is the break force, w = sample width, and b the sample thickness.

3.2.6. C_f/SiC Composite Plate Samples

The C_f/SiC AE data measured from previous tensile tests from Almeida et al. (2019b) was used for testing the model performance for other CMCs. In specific, the AE data gathered from this previous work was selected because the samples were previously fatigued, and then tensile tested. This enables us to analyze the model performance for different testing conditions, i.e., check for differences in the damage mechanisms classification.

The tensile-fatigue tests were carried out according to the standard ASTM C1360 (2017). The stress of 58.2 MPa was used as the fatigue limit. The samples were analyzed after 200, 10,000, and 2,000,000 fatigue cycles and compared to an as-produced specimen. Because of the material availability when these tests were performed, only one sample could be tested per condition. For better comprehension of microstructural changes after the loading cycles, SEM analysis was performed for as-produced and 2,000,000 samples.

The tensile tests were performed using a servo-hydraulic testing machine Roell-Amsler System Rel 2100 (Zwick Roell Group, Ulm, Germany) with an MTS Flex Test 40 controller. The applied load was measured with a 25 kN load cell of the testing machine. Strain data was measured using a laser extensometer (Fiedler Optoelektronik GmbH, Lützen, Germany) over white marks 25 mm apart. Figure 32 illustrates the 2.5D C_f/SiC sample geometry and testing machine. The tensile strength was calculated using equation 3.1, and the elastic modulus was measured by assessing the stress-strain curve inclination.

Figure 32 – (a) 2.5D C_f/SiC sample geometry and (b) testing machine highlighting AE sensors, sample, and laser extensometer.

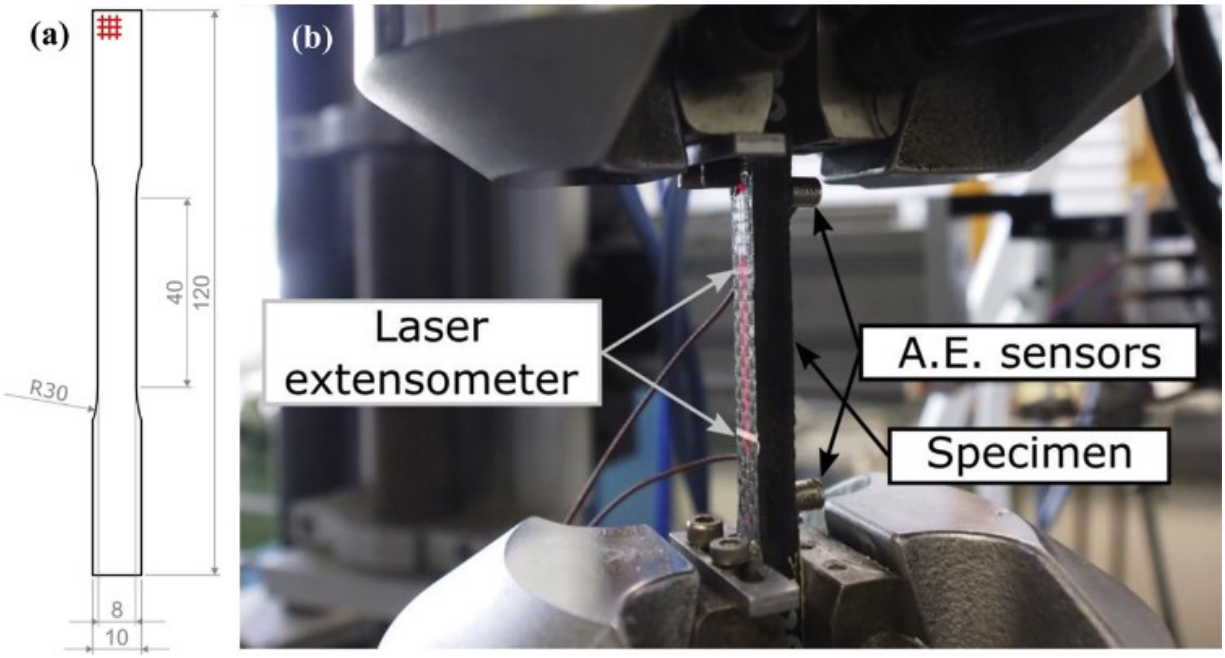

Source: ALMEIDA et al. (2019b, p. 2246)

3.3. ACOUSTIC EMISSION EVALUATION

To measure the damage mechanisms signals of the material during the mechanical tests, an acoustic emission acquisition system Vallen AMSY4-PC was used. The equipment has 2 channels, each one connected to a piezoelectric sensor (VS600-Z2, Vallen Systeme GmbH, Icking, Germany) with a sensitive frequency of 600 kHz. The parameters used for hit definition in the acoustic emission device were chosen according to previous works performed at the institute (ALMEIDA et al., 2016; VOLKMANN et al., 2014). Those parameters are shown in Table 7.

Table 7 – Acoustic emission parameters used.

Parameter	Value
Preamplifier gain	40 dB
Threshold	30 dB
Duration discrimination time (DDT)	50 µs
Rearm Time (RT)	100 µs
Filter	10 Crossing count

Source: author

The sensors were either attached directly to the samples or to the fixtures using hot glue, as mentioned in section 3.2. The mechanical tests were initiated after starting the AE recording. For samples that were tested with a pre-load, AE monitoring started after the set load was achieved. Both devices were stopped when the force signal stabilized, i.e., maintaining its value on a certain range after the maximum force had already been reached and then dropped.

3.4. DATA ANALYSES

Considering that this work's purpose is to analyze the damage mechanisms on CMCs, it concerns a classification problem. Hence, a supervised ML approach was used. For utilizing this method, a previous dataset with labeled inputs (targets) from each type of mechanism is needed, the training set. To this end, the data acquired from pre-tests samples was prepared and used. This dataset was employed on a python script which served to train a

model. The trained model tries to identify each of the features from the data, such as amplitude, rise time, energy, counts, and frequency; and then classifies new unlabeled data on a group by comparison with the training set, based on a classification algorithm. A flowchart is shown in Figure 33, showing the steps to acquire the classification model and their specific procedures. In this flowchart, the first step is the data acquisition. As already briefed, this was done by performing mechanical tests with AE monitoring, which enabled gathering information from distinct signal types. Then, this information was used to formulate the training dataset, responsible for teaching the classification model on how to interpret new data. Together with this step, the features responsible for differentiating one signal from another need to be selected, such as amplitude, average frequency, and energy. The final step before the damage mechanisms classification of unseen data is the model fitting. For this, a classification algorithm needs to be selected. Finally, the model can be used for evaluation, by inserting unseen data as input. To achieve reliable results, some points are crucial and need to be highlighted: the training set; the features; and the algorithm for the data classification. Those points are explained in detail in the following subsections.

Figure 33 – Flowchart of the steps for the model acquisition.

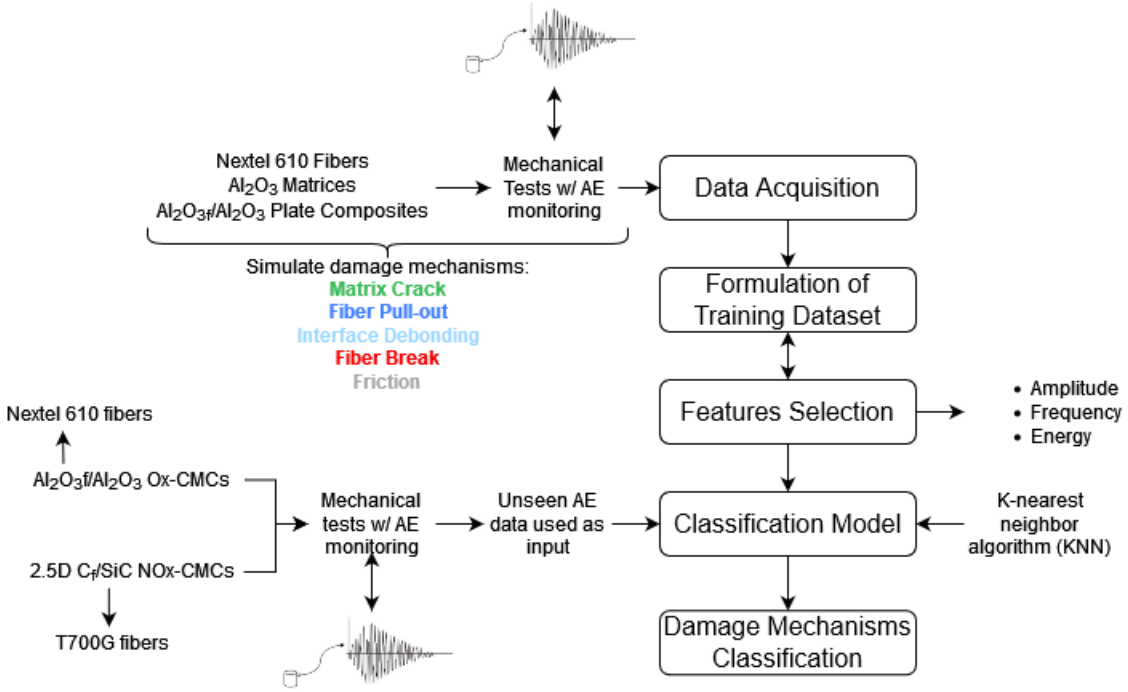

Source: author

3.4.1. Training Set

The training set has the information used to train the model. It includes both input data and the corresponding expected output. Based on this data, the model was capable of learning and producing results when later presented with new unseen data.

To improve the accuracy of the results that will be predicted by the model, detailed labeled data is needed. To this end, pre-test samples were mechanically loaded in a way to narrow the mechanisms acting, restricting the possible damage mechanism signals recorded. The data from each test was then combined to compose the training set. It should be noted that, when composing the training set, fiber break, matrix crack, fiber pull-out, and interface debonding signals were analyzed. However, due to the existence of noise on the machine, as well as friction between the fibers, those needed to be considered on the model.

To label the data and compose the training set, a filter was applied to the signals. Previous works that characterize the damage mechanisms with AE were taken into consideration to filter the signals (GHOLIZADEH et al., 2018; SHIWA et al., 1995). In these works, the authors have analyzed the range of amplitude for each damage mechanism. However, specific ranges are not given. Matrix crack was observed as having lower amplitudes (30~50 dB). As the amplitudes got higher, interface debonding and fiber pull-out were observed (55~65 dB), and finally, fiber break at the highest amplitudes (70~90 dB).

During fiber tensile tests, single filament and ten filament tests were used to determine the minimum amplitude of a fiber break signal. Then, bundle signals were labeled accordingly, separating the signals of fiber friction obtained from the same test and also labeling them. For matrix tests, the signals obtained were assumed to be related to matrix crack and labeled as that. For fiber pull-out and SBB tests, more than one signal type was promoted. Fiber pull-out tensile tests provided information from fiber friction, fiber break, matrix crack, and fiber pull-out. Whereas SBB tests provided all signal types analyzed in this work. Because of that, fiber pull-out and interface debonding were selected and labeled through exclusion, using the signals information acquired from the other tests as guidelines.

Signals with the number of threshold crossing counts equal to 1 were treated as machine noise and excluded from the training set. To obtain the finalized training set, the localization of the signals measured was performed. This is possible because of the use of the two sensors. Only signals located between the two sensors were analyzed. This ensures that the signals

recorded happened in fact due to the vibration that comes from changes in the microstructure during the mechanical tests. Table 8 displays the filter values to label the data from each test and which acquisition test was used to measure these signals.

Table 8 – Filters used for data labeling and assembling of the training set.

Signal Acquired	Amplitude (dB)	Acquisition Method
Fiber Break	> 65	Fiber tensile test
Friction	< 65	Fiber tensile test
Matrix Crack	< 50	4-point bending test and SENB test
Fiber Pull-out	> 40	Fiber pull-out test
Interface Debonding	55 < X < 65	SBB test

Source: author

3.4.2. Features Selection

The feature selection has a huge influence on the performance of the model, where irrelevant features can negatively impact the model design. For this work, a filter method was used for the feature selection. With this method, the training set was filtered through a correlation matrix, which was done using Kendall's Tau correlation. For this correlation, the coefficients have values between -1 and 1. Values closer to 0 imply a weaker correlation and values closer to 1 and -1 imply a stronger correlation (KENDALL, 1938).

The information from the acoustic emission, that is, the features that were taken for testing were amplitude (A), rise time (R), duration (D), threshold crossing counts (TCC), energy (E), and average frequency (F). Two points are emphasized here. First, the energy is measured in eu units, where $1\,eu = 1 \times 10^{-18}\,J$. Second, the latter feature, "F", is the number of threshold crossing counts divided by the hit duration.

3.4.3. Classification Algorithm

The classification algorithm used in this work is the k-nearest neighbor (KNN, scikit-learn library). This algorithm was chosen due to previous works (BANSAL; LAMON, 2015;

SALEM; SINGH, 2017; TRIPATHI et al., 2019) and its practical appliance, making it easier to code. Still, other algorithms were tested (e.g., random forest, SGD, and naive bayes) but not continued in this work. Because this algorithm measures the distance between points, the Euclidian distance was used. In addition, the datapoints for the training set were scaled using a min-max function in python, so that the datapoint all presented values between -1 and 1.

To obtain a reliable prediction model, evaluating the classifier, i.e., testing its accuracy to verify its applicability is especially important. In this work, the k-fold cross validation method was applied. This validation method gives accuracy scores for each of the targets, which in this case are the signal types that were evaluated. This was chosen because of its less biased estimate of the model skill in comparison to other methods, as explained in subsection 2.4. This evaluation method uses a re-sampling approach. The general procedure is as follows (BROWNLEE, 2019).

1. “Shuffle the dataset randomly
2. Split the dataset into “k” groups
    a. For each unique group:
        i. Take the group as a hold-out or test data set
        ii. Take the remaining groups as a training data set
3. Fit a model on the training set and evaluate it on the test set
4. Retain the evaluation score and discard the model
5. Summarize the skill of the model using the sample of model evaluation scores”

Succeeding the model performance score, predictions of the damage mechanisms behavior were accomplished. When new unseen data is used as an input, classification is performed according to what the model has learned from the training set. As an output, the labeled data is acquired. The input data was obtained from the final test characterizations: Al_2O_{3f}/Al_2O_3 minicomposite tensile tests and composite plate 4-point bending tests, and C_f/SiC composite plate tensile tests. For having a better classification, the same way as for the training dataset, signals with TCC equal to 1 were dropped and considered as noise. In addition, localization was also performed to assure that the signals measured were due to structural changes in the composite.

4. RESULTS AND DISCUSSION

The results are divided into three sections and are according to the steps necessary to achieve the objectives of this work. First, a discussion is made concerning the characterization of samples regarded as pre-tests, addressing their mechanical and AE monitoring results. Then, an overview of the training dataset and model accuracy is presented for the supervised classification model created. Lastly, the quantification of the damage mechanisms from Al_2O_{3f}/Al_2O_3 Ox-CMCs and C_f/SiC NOx-CMCs is addressed.

4.1 MECHANICAL ANALYSES AND AE SIGNALS MEASUREMENTS

As mentioned in section 3, the mechanical tests were performed in a way to promote signals specific to a type of damage. Those were matrix cracking, interface debonding, fiber pull-out, and fiber break. For improving the model accuracy, frictional signals were also accounted. The results obtained from these mechanical tests are described in the following subsections. The stress-displacements and stress-strain curves for the pre-test samples are exhibited in Figure A1 and Figure A2 of Annex A respectively.

4.1.1 Al_2O_3 Fibers

For measuring fiber break signals using AE monitoring, tensile tests were conducted on three sorts of fiber samples: single filament; 10-filament; and bundles.

For the single filament tests, it is usual that their fracture data exhibit a significant variation due to inherent flaws with a random distribution. Because of that, the strength of single filament fibers is better represented by a statistical variable, which depends on factors such as stress state, size of test samples, and the number of test samples (BANSAL; LAMON, 2015). Therefore, the results of single filament tensile tests were described using the Weibull's distribution. The Weibull's distribution takes into consideration the weakest link theory (WEIBULL, 1951). Thus, implying that the samples fail at the weakest point. Two parameters can be used to describe the distribution: the Weibull modulus (β) and scale (σ_0) (WOLFENDEN; VAN DER ZWAAG, 1989). The Weibull modulus represents the deviation of the results. For instance, if the strength results measured have a high variation, β is low. In

this situation, more than one strength value better describes the material's strength. For this test, the scale parameter is the characteristic strength (σ_0) of the fibers. It represents the stress at which 63.2 % of the fibers fail.

The failure distributions for the single filament tensile tests are shown in Figure 34 for 25 and 70 mm in length samples. The shape parameter β was similar for both sizes. In other words, different sample sizes did not change the dispersion of results obtained. As for the scale parameter, σ_0, it is important to highlight its relationship with the tested sample length. The higher the volume of the tested material, the higher are the chances of finding a critical flaw that weakens the sample. Therefore, bigger samples presented lower σ_0, meaning that they are expected to fail at lower stresses.

Figure 34 – Weibull's distribution plot for single filament samples for 25 and 70 mm in length. The distribution is described by Weibull's modulus (β) and scale parameters. For this test, the scale parameter is the characteristic strength (σ_0).

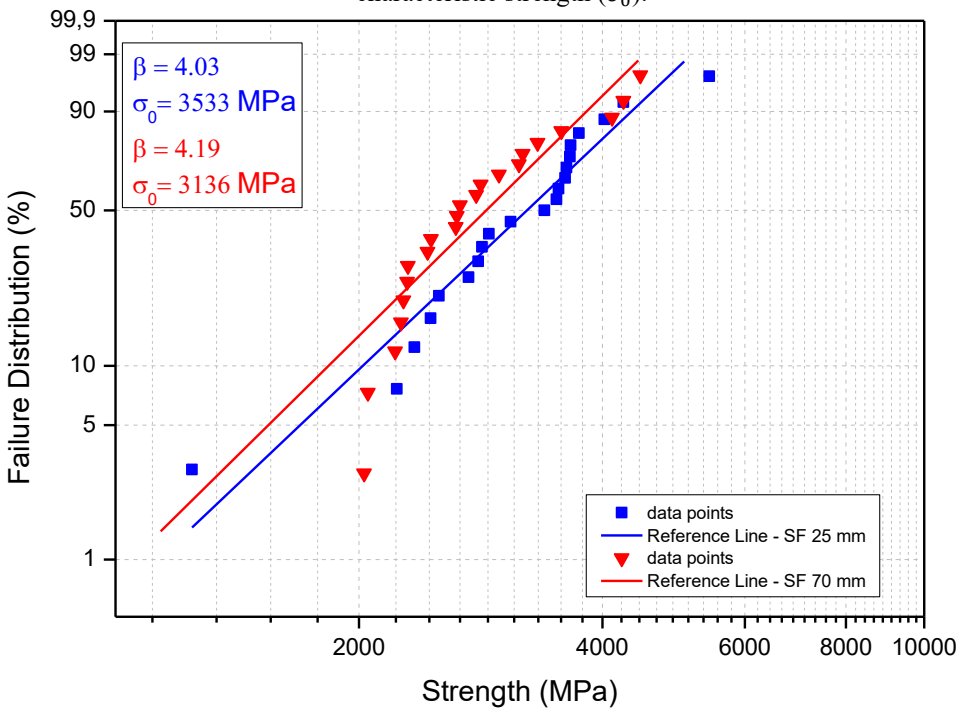

Source: author

After performing the single filament tensile tests, the AE signals recorded were evaluated. The values and standard deviation (SD) for amplitude (A), rise time (R), duration (D), number of counts (TCC), energy (E), and average frequency (F) are shown in Table 9. Regarding the difference in samples' length on the AE signals recorded, no significant

distinction was seen for any samples tested. Thus, the AE signal values are shown only in one table, disregarding the sample size.

The interesting point about this test is that it gives information about a single fiber break. Therefore, single filament testing aids in labeling signals from other tests which have reduced specificity. The AE signals recorded from this test were used as a baseline for recognizing and labeling fiber break signals from fiber bundle tensile tests. The amplitude values were used to do that. Even though both amplitude and average frequency did not present a high variation, the amplitude was still chosen for comparison with other signals, as it was already used in other works to describe damage mechanisms (GHOLIZADEH et al., 2018; SHIWA et al., 1995). As exhibited in Table 9, other AE parameters presented a higher variation. Hence, were not used as a baseline for labeling.

Table 9 – Fiber break acoustic emission parameters recorded from single filament tensile tests. A, amplitude; R, rise time; D, duration; TCC, threshold crossing counts; E, energy; F, average frequency; SD, standard deviation.

	A (dB)	R (µs)	D (µs)	TCC	E (eu)	F (MHz)
Average value	75.03	30.44	2256.26	950.04	700.71	0.424
SD	7.27	28.43	847.36	340.39	506.72	0.043

Source: author

For analyzing the strength of the 10-filament and fiber bundle tensile tests, the apparent strength was measured, shown in Figure 35 for 10-filament and fiber bundle samples. The apparent strength represents the maximum stress sustained by the bundle while considering only the initial bundle area. Analyzing the measured apparent strength for 10-filament and fiber bundle samples, it is noted that the values are much lower than what was seen for single filament tensile tests. Nevertheless, these values are not comparable. As stated before, the apparent strength considers the initial sample area. When the maximum load is achieved, several fibers have already failed beforehand. If the instant area would be considered, the calculated strength would be higher. In addition, the values presented deviations because fibers characterization can be a complicated thing to do. Handling and processing can create flaws in the material (NAWY, 2008), affecting the fiber's apparent strength. Regarding the differences in sample size, as aforementioned, testing a higher volume of material increases the probability of finding more flaws. Thus, longer samples were measured to have lower apparent strengths.

Figure 35 – Apparent strength of 10-filament (10F) and bundle samples with 25 and 70 mm in length sizes.

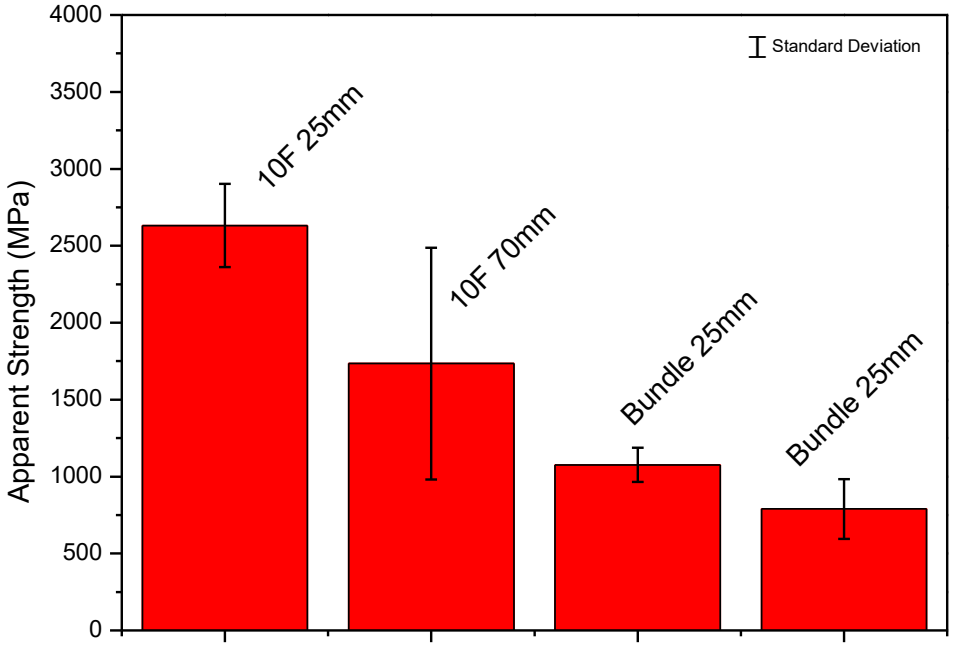

Source: author

The AE signals recorded from the 10-filament tensile tests are illustrated in Table 10. Both values of A and F are similar to what was measured from single filament tests. However, differences with other parameters are caused by the greater number of filaments being tested. This ensures that a wider range of values describing this type of signal – fiber break – can be obtained, so that the model is able to recognize this type of signal more easily. The same applies to fiber bundle tests.

Table 10 – Fiber break acoustic emission parameters recorded from 10-filament tensile tests. A, amplitude; R, rise time; D, duration; TCC, threshold crossing counts; E, energy; F, average frequency; SD, standard deviation.

	A (dB)	R (µs)	D (µs)	TCC	E (eu)	F (MHz)
Average Values	77	55.32	2905.71	1230.24	844.46	0.423
SD	2.16	16.02	185.29	76.54	112.56	0.005

Source: author

Regarding the AE signals from bundle tensile tests, the increased amount of fibers makes it susceptible to signals that do not correspond to fiber break to be measured. Those signals are possibly related to friction between fibers. To label all the signals required for the training dataset, single filament and 10-filament tests were used as a guideline. Table 8 in

subsection 3.4.1 illustrates the filters to perform that. Table 11 shows the AE parameters values for fiber break and fiber friction signals measured during fiber bundle tests.

Table 11 – Fiber break and fiber friction acoustic emission parameters recorded from fiber bundle tensile tests. A, amplitude; R, rise time; D, duration; TCC, threshold crossing counts; E, energy; F, average frequency; SD, standard deviation.

	A (dB)	R (μs)	D (μs)	TCC	E (eu)	F (MHz)
Fiber Break						
Average Values	72.77	34.34	1699.85	683.62	391.96	0.405
SD	5.19	164.44	786.42	313.06	376.90	0.034
Friction						
Average Values	46.86	23.55	333.52	108.85	19.44	0.251
SD	10.313	35.561	369.85	144.96	32.41	0.125

Source: author

4.1.2 Al_2O_3 Matrices

The alumina matrices were subjected to bending tests. The tests were performed on notched and unnotched samples, aiming to record matrix cracking AE signals.

For evaluating the unnotched samples, the different sized matrices (45 and 70 mm) were subjected to 4-point bending tests. The flexural strength obtained was fit in a Weibull distribution (Figure 36). Both the modulus (β) and scale (σ_0) parameters were obtained. The first thing to notice is the difference between the slope of each curve, related to the modulus parameter. While samples with 45 mm in length presented β value of 6.64, the samples with 70 mm presented a lower value, equal to 3.45. In other words, the strength values are narrower for smaller samples. This behavior is related with the inherent defects that are present on the matrices, e.g., pores. Because the matrices produced are rather porous and not necessarily well distributed, these defects act as weak points to nucleate a crack and begin a brittle failure process. Since the longer samples have a higher probability of having defects, a wider distribution of strength values is expected, justifying their lower β. Similarly, 70 mm samples have a lower characteristic strength (σ_0=31.31 MPa) if compared to the 45 mm samples (σ_0=37.22 MPa).

Figure 36 – Weibull's distribution plot for Al_2O_3 matrices 45 and 70 mm in length sizes. The distribution is described by Weibull's modulus (β) and scale parameters. For this test, the scale parameter is the characteristic strength (σ_0).

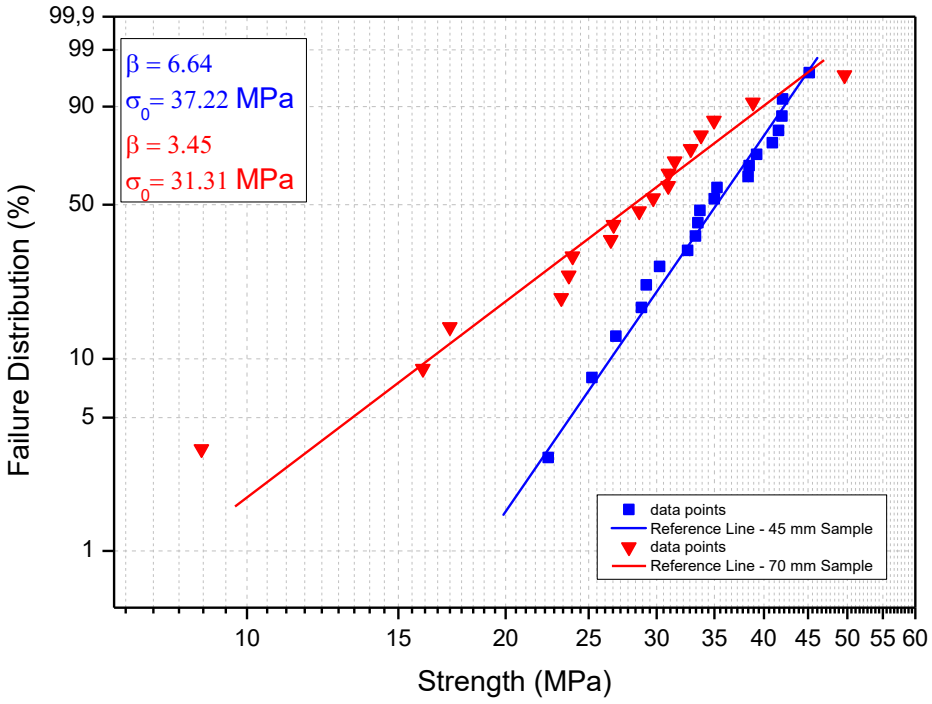

Source: author

Regarding the notched matrices, SENB tests were performed. Hence, the fracture toughness (K_{IC}) was measured. The average values of K_{IC} for 45 and 70 mm samples are exhibited in Figure 37. The fracture toughness values measured are rather low if compared with the usual values obtained for Al_2O_3 ceramics. The usual range for these materials is 3~5 MPa$\sqrt{m}$ (AUERKARI, 1996). Nevertheless, these ranges are related to dense matrices. For simulating the damage mechanisms in this work, the Al_2O_3 matrices were aimed to be porous. It is a necessary criterion for enabling crack deflection using the weak matrix concept, as explained in section 2.2. Because of that, the samples K_{IC} values were around 1 MPa$\sqrt{m}$ for both sample lengths.

Figure 37 – Fracture toughness of notched Al_2O_3 matrices.

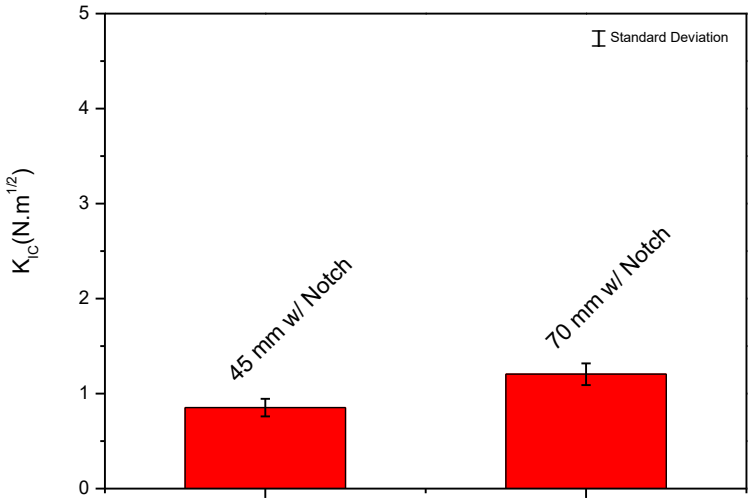

Source: author

The AE signals measured to simulate matrix cracking from both tests performed, 4-point bending and SENB tests are shown in Table 12. As explained in subsection 3.2.2, notched samples had the purpose to simulate crack propagation, while unnotched aimed to simulate crack initiation and propagation. After analyzing the values measured for both samples, A and F presented similar values, while other parameters had a higher deviation. From the amplitude and frequency values, we can say that both initiation and propagation have the same nature (matrix cracking), explaining the reason for approximate values. However, the acoustic energy associated with each mechanism is probably different. It is observed that the notched matrices have lower AE energy. This occurs because the notch makes it easier for the crack to propagate, contrary to unnotched samples where more mechanical energy is necessary for crack initiation and propagation. In addition, because the crack length for notched samples is smaller, other parameters also exhibited a lower mean value and deviation in comparison with unnotched matrices.

Table 12 – Matrix crack acoustic emission parameters recorded from matrices bending tests. A, amplitude; R, rise time; D, duration; TCC, threshold crossing counts; E, energy; F, average frequency; SD, standard deviation.

	A (dB)	R (µs)	D (µs)	TCC	E (eu)	F (MHz)
Unnotched Samples						
Average Value	37.09	112,98	356,52	65,55	8.06	0.144
SD	4.80	301.84	789.58	184.48	20.16	0.109
Notched Samples						
Average Value	36.53	82.00	242.77	37.15	5.09	0.126
SD	4.38	196.48	367.99	79.67	8.86	0.095

Source: author

4.1.3 Al_2O_3 Fiber Pull-out Samples

Fiber pull-out tensile tests were conducted to acquire signals corresponding to a fiber being pulled from the matrix. In this test, the pull-out shear strength was measured. As described in subsection 3.2.3, these values should only be used as a reference. Since the actual height and amount of fibers inserted inside the matrix could not be measured, the shear strength is relatively low and presented a high deviation, with a value of $0.34 \pm 0{,}17$ MPa.

Even though the samples were prepared to trigger specific signals (in this case fiber pull-out), the AE signals acquired during this test cannot be directly isolated as well as fiber and matrix tests. Other signals may be recorded at a smaller degree, such as fiber break, fiber friction, and matrix crack. For filtering the desired signal – fiber pull-out – the information from the previous tests was used. After filtering, the signal values corresponding to pull-out are shown in Table 13.

Table 13 – Fiber pull-out acoustic emission parameters recorded from fiber pull-out tensile tests. A, amplitude; R, rise time; D, duration; TCC, threshold crossing counts; E, energy; F, average frequency.

	A (dB)	R (µs)	D (µs)	TCC	E (eu)	F (MHz)
Average Values	62.92	21.8	1304.13	481.44	208.86	0.351
SD	10.79	62.32	593.13	256.24	237.33	0.066

Source: author

4.1.4 Al_2O_3 Composite Plates

The last samples categorized as pre-test were the Al_2O_3 composite plates. These samples had the purpose to measure AE signals associated with interfacial debonding. The test performed was the SBB test, in which the stress to delaminate the layers was measured. The shear strength values presented a high deviation from the mean value, which was measured to be 7.89 ± 2.28 MPa. This can be related to defects within the material structure, such as porosity or defects caused by samples manufacturing. Because the composite plates are produced manually, differences during steps of stacking and pressing the layers can affect the shear strength between samples. Since the aim of this work is to simulate the damage mechanisms and quantify them, possible differences in strength are not further discussed.

It is emphasized that both fiber pull-out and SBB tests measure the strength of the fiber/matrix interface. Considering that there are defects between the composite plate layers, it would be expected that their strength results would be lower than the real pull-out shear strength. Since the shear strength of pull-out samples was just used as a reference value, this was not observed.

Because a composite is being tested, interface debonding signals cannot be isolated from other signals during the SBB tests. Thus, the AE signals need to be filtered in order to isolate the interface debonding data. For this, the information obtained from the previous pre-tests was used again. The order that the tests were performed should be emphasized. This enabled the labeling of the signals accordingly to each specific damage mechanism and obtain a reliable training dataset.

To better analyze the SBB test signals and isolate ones corresponding to interface debonding, a histogram dividing the signals in a range of amplitudes was made, shown in Figure 38.

Figure 38 – Amplitude values measured from composite plates during short-beam bending test.

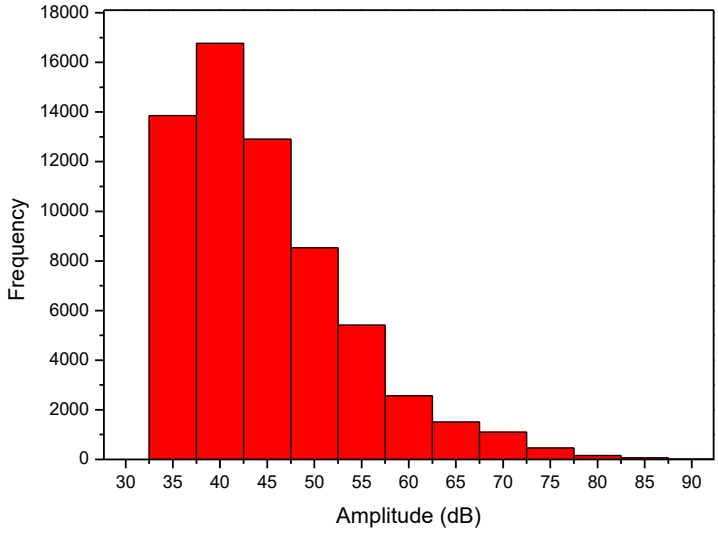

Source: author

Considering the amplitude values from other pre-tests, amplitudes between 35 and 50 dB were related to matrix crack and fiber friction. Therefore, signals in the range of 55 to 65 dB were treated as being related to interface debonding, while higher amplitude signals to fiber break. Concerning fiber pull-out signals, it is important to note that it is a similar mechanism with interface debonding. Both are related to the fiber/matrix interface (KIM; ZHOU; MAI, 1993) but are distinguished by the measuring method. In the case of fiber pull-out tensile tests, the interface is the main aspect for measuring it. As for SBB tests, the shear strength between layers is being tested. Therefore, it is not only dependent on the fiber/matrix interface, but also on the defects present in between layers. Because of this similarity, interface debonding and fiber pull-out signals could not be distinguished on SBB tests. Since the test performed induces shear stress to delaminate the composite plate layers, interface debonding signals were assumed to be recorded instead of fiber pull-out. Table 14 exhibits the parameter values for interface debonding signals after filtering.

Table 14 – Interface debonding acoustic emission parameters recorded from short-beam bending tests. A, amplitude; R, rise time; D, duration; TCC, threshold crossing counts; E, energy; F, average frequency; SD, standard deviation.

	A (dB)	R (µs)	D (µs)	TCC	E (eu)	F (MHz)
Values	58.98	64.79	679.64	206.00	46.83	0.311
SD	2.84	126.21	321.48	99.54	25.58	0.059

Source: author

4.2 SUPERVISED CLASSIFICATION MODEL

This section covers the results concerning the assembling of the training dataset, model creation, and evaluation.

First, the acoustic emission signals measured from pre-tests were labeled accordingly to their respective damage mechanisms and then arranged in a single .csv file. For creating the classification model, first the features and algorithm need to be selected. To select the features, i.e., the identifiers responsible to distinguish signals from another, a correlation matrix based on Kendall's Tau correlation was used. The correlation is illustrated as a heatmap in Figure 39. This enables to view the relationship between the AE features with the target column, the damage mechanism.

Figure 39 – Kendall's Tau correlation heatmap used for features selection, where the AE features were correlated with the variable "Damage Mechanisms". The features are Amplitude (A), rise time (R), duration (D), threshold crossing counts (TCC), energy (E), and average frequency (F).

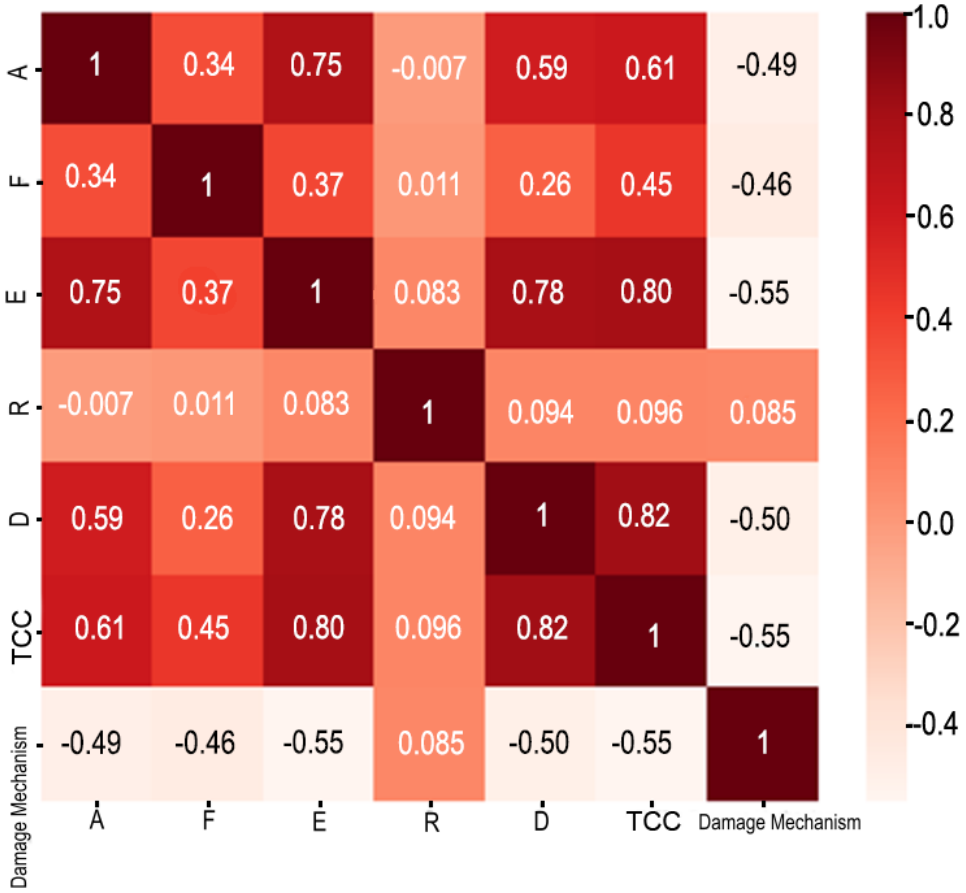

Source: author

In this correlation, the closer the values are to 1 or -1, the stronger is the relationship between the variables. As explained in subsection 3.4.2, the average frequency (F) is a combination of the number of threshold crossing counts (TCC) and duration (D). If variables are highly correlated with each other, teaching the model the same thing twice could lead to biases and overfitting. Therefore, TCC and D were dropped, keeping F as it gives the essential information of both while being a unique feature. The rise time (R) was also disregarded due to its low correlation with the target.

Ultimately, A, E, and F were the chosen features for obtaining the training dataset. The range of values for each signal type is summarized in Table 15. These values are represented in Figure 40, illustrating the amplitude values in function of the frequency and energy.

Table 15 – Values of amplitude, energy, and average frequency for each signal on the training dataset along their standard deviation.

Signal	A (dB)	E (eu)	F (MHz)
Fiber Break	72.14 ± 6.46	390.55 ± 411.38	0.41 ± 0.04
Friction	34.12 ± 1.76	1.26 ± 0.63	0.29 ± 0.54
Fiber Pull-out	62.35 ± 5.64	122.43 ± 79.87	0.35 ± 0.05
Interface Debonding	59.36 ± 2.86	47.35 ± 25.68	0.32 ± 0.06
Matrix Crack	41.96 ± 7.18	15.14 ± 37.23	0.22 ± 0.11

Source: author

Figure 40 – Disposition of amplitude, frequency, and energy for each signal type.

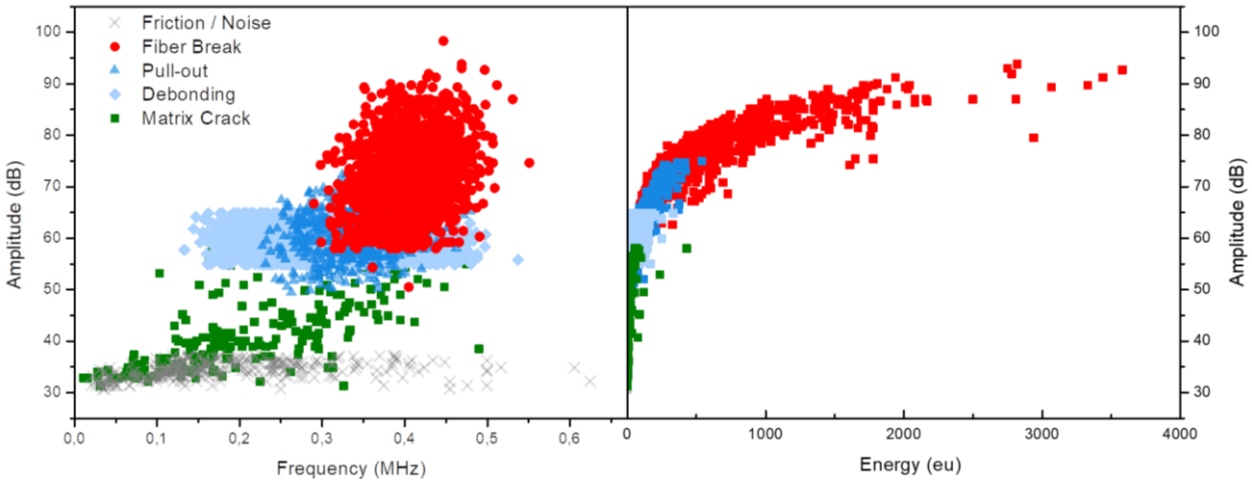

Source: author

For the amplitude values, fiber break is associated with higher values (70~90 dB). Interfacial mechanisms are observed in the mid-range (50~70 dB), and lower

amplitudes (30~50 dB) are related to matrix cracking and fiber friction. Examining Figure 40, it should be noted that some signals are either similar or have a higher range. This is the case for matrix crack and fiber friction, as well as interface debonding and fiber pull-out. As discussed previously, the latter are mechanisms that are related to the fiber/matrix interface. Hence, both present similar AE signals. Concerning matrix crack and fiber friction, even though both are not comparative phenomena, their signals have similar values. This is justified by how matrix cracking acts in the material. Because the matrix is the weakest part of the composite, matrix crack signals are events characterized by low amplitudes, as the accumulated energy to trigger them is also low. In the case of fiber friction, this signal is simply the friction in between fibers, hence the acoustic wave that is recorded from this phenomenon also presents low amplitudes. Because of the similarity between these signals, the model might confuse them when the classification of composite data is performed. By combining multiple sets of identifiers – A, E, and F – it is possible to minimize this obstacle. This assists in obtaining a robust model, even with overlapping and smaller training datasets.

After assembling the training dataset, it was used to create the supervised ML model in which the KNN algorithm was applied. The KNN algorithm was chosen because of its simple application and fit. The score corresponds to how accurate the model can predict and classify unseen data, based on what it has learned from the training set. The precision for each independent signal and the average k-fold score are shown in Table 16.

Table 16 – Model precision using the k-fold cross validation method.

Signal	Precision (%)
Fiber Break	84
Friction	96
Fiber Pull-out	34
Interface Debonding	97
Matrix Crack	59
Average k-fold score	88

Source: author

The average score is equal to 88%. This means that the model can recognize and differentiate signals and doesn’t seem to have obstacles such as overfitting and underfitting.

Analyzing the precision values, it should be pointed that fiber pull-out presented a lower precision. One of the reasons this could be happening is because of the similarity with interface debonding, as pointed earlier. While it seems to have a good performance for recognizing interface debonding, pull-out values might be more difficult. Similar behavior is seen for matrix cracking and friction. However, the model is still able to distinguish between these two. An important result is that the frictional signals exhibited exceptional performance. This makes the model more reliable for discerning frictional signals from structural changes, lessening misclassifications.

In addition to these observations, the number of datapoints from the training dataset needs to be addressed. A larger quantity of one signal compared to another may result in a better performance for the signal present in a higher amount. This happens because there is more information the model can learn from. Due to the way the mechanical tests were conducted for assembling the dataset, less information is measured for some signals. This is the case for matrix cracking. As a result, their precision can be affected.

4.3 DAMAGE MECHANISM QUANTIFICATION

The following section covers the analyses of samples designated as “final tests”. The damage mechanisms quantification will be discussed for three types of samples: Al_2O_{3f}/Al_2O_3 minicomposites and composite plates, and C_f/SiC composite plates.

For performing the quantification, the samples were subjected to mechanical tests jointly with acoustic emission monitoring. Then, the AE signals recorded were used as input on the supervised ML model created. The output data (i.e., the classification information) was used to illustrate three main sorts of plots that are going to be discussed. First, the cumulative hit count (CHIT) respective to each type of signal was plotted against the correspondent mechanical test used to measure the AE signals. The CHIT is simply the number of hits for a specific AE event. This is a simple way to visualize the damage development. The other two plot types are bar graphs corresponding to the total CHIT percentages, and total energy dissipated. This permits quantifying which mechanisms are mostly happening, and which dissipates more energy for crack deflection. Because several samples were manufactured, only

selected ones are illustrated here. Additional sample plots are illustrated in Figure A3 and Figure A4 of Annex A for minicomposites and composite plates respectively.

4.3.1 Al_2O_{3f}/Al_2O_3 Minicomposites

For collecting AE data associated with damage mechanisms being triggered in a composite, the minicomposites were subjected to tensile tests. The average tensile strength measured during the test was 116 ± 34 MPa. After performing the mechanical test simultaneously to acoustic emission monitoring, the data that was recorded was used as an input on the supervised ML model constructed. The output – i.e., the signals post-classification – are seen in Figure 41 for a minicomposite sample. This plot illustrates the damage development as load and time progress.

As the load increased, signals associated with matrix cracking, debonding, and friction were observed. Towards higher loads, around ~100 MPa there is a sudden increase in signals followed by pull-out and fiber break, indicating the composite failure. For evaluating the damage development behavior, first it is necessary to assess what is likely to happen. According to the literature (EVANS; ZOK, 1994; ZOK; LEVI, 2001), because the matrix is the weakest link of the composite, matrix cracking is expected to be the first damage mechanism to act. The cracks propagate through the matrix and are deflected in the fiber/matrix interface. So, interface debonding follows, facilitating pull-out. When the load is high enough, fiber break occurs, leading the composite to its failure. It must be emphasized that the onset of a specific mechanism does not exclude the occurrence of others. Both act to continue energy dissipation. Regarding friction between fibers, no other similar works were found in the literature. What is assumed is that when the fiber/matrix interface is damaged, friction is facilitated, and increases when fibers break at higher loads.

Comparing the observed behavior with the literature, while there are a few inconsistencies, the performance is close to what is expected. Frictional signals were recognized at the test beginning. As pointed earlier, it may be caused because of the similarity with matrix cracking feature values, resulting in some misclassifications. However, considering the high classification precision for frictional signals, a hypothesis is that friction is not exclusive to fibers, which were the main source for assembling the dataset. As the composite is loaded,

friction between the fiber/matrix interface can also occur. Hence, if these two frictional signals were to have similar values, it would justify it being recognized at the test beginning.

Continuing the load increase, matrix cracking and interface debonding are observed. Both mechanisms were recognized first at similar loads (61~70 MPa), increasing towards the composite failure. This can be explained because, while the crack propagates in the matrix, it is deflected in the interface, promoting debonding. Thus, they might occur at similar times, as observed for this sample. Finally, signals identified as fiber pull-out and fiber break presented the expected behavior. These signals initiated at around ~87 MPa. As commented earlier, there is an increase in both pull-out and fiber break at ~100 MPa, preceding the composite failure. Still, few fiber break and pull-out events were recognized at lower stresses. This might be related to flaws in the fibers. As a result, these fibers are weakened and fail prematurely, facilitating pull-out and fiber break.

Figure 41 – Damage development of Al_2O_{3f}/ Al_2O_3 minicomposite tensile test, illustrating the test stress, and cumulative hit count (CHIT) increase for each signal.

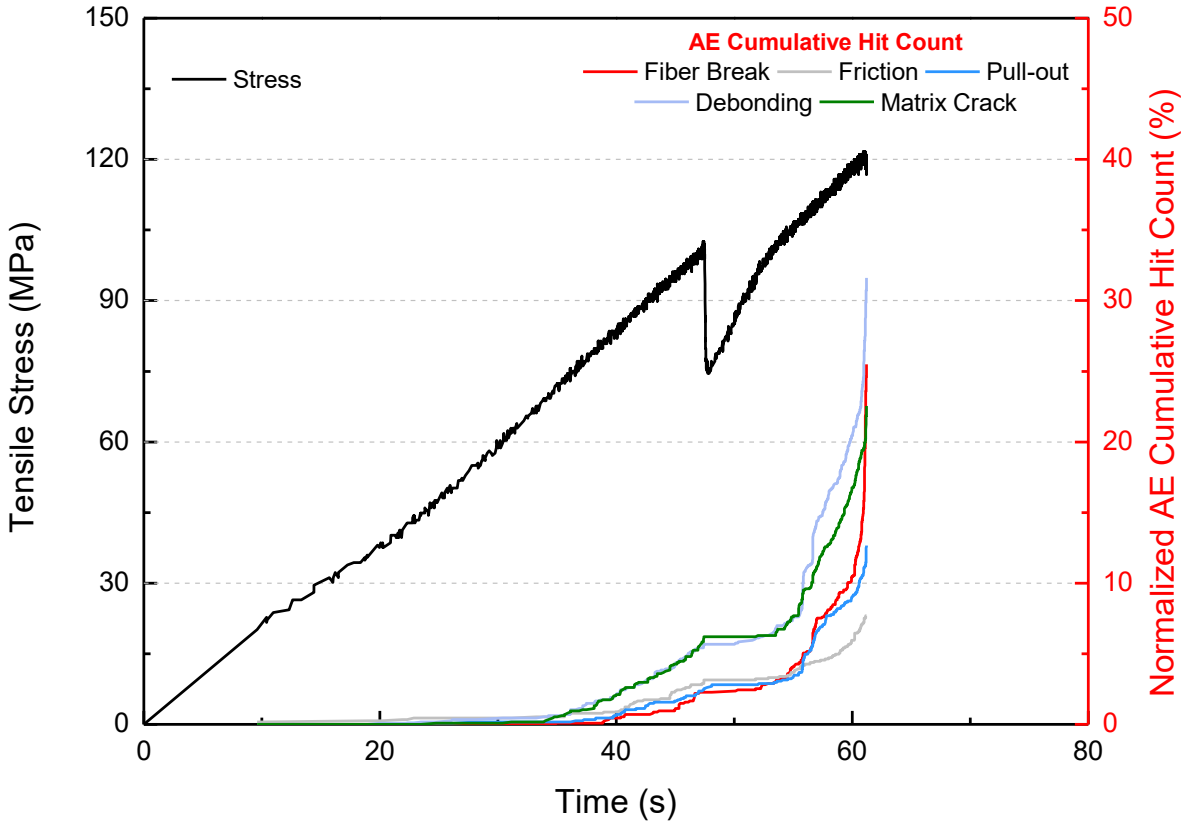

Source: author

Figure 42 shows the CHIT amount in percentages for each signal, corresponding to the minicomposite tensile test presented in Figure 41.

Observing the percentage values and considering only crack deflection mechanisms, interface debonding takes place more frequently, followed by matrix cracking and fiber pull-out. Considering that the matrix is the weakest link, the crack propagates and is deflected, enabling debonding. Thus, the first and second mechanisms are easier to occur, explaining the higher percentages. The lower amount of fiber pull-out is related to the composite failure development. Since it is dependent on the shear stress necessary to damage the fiber/matrix interface, it is facilitated when debonding and fiber break already took place. Because fiber break mainly occurs towards the test end, there are fewer opportunities for fiber pull-out to happen.

Figure 42 – Quantification of cumulative hit count (CHIT) for Al_2O_{3f}/Al_2O_3 minicomposite measured during tensile test. The signals that were quantified are fiber friction, fiber break, fiber pull-out, interface debonding, and matrix crack.

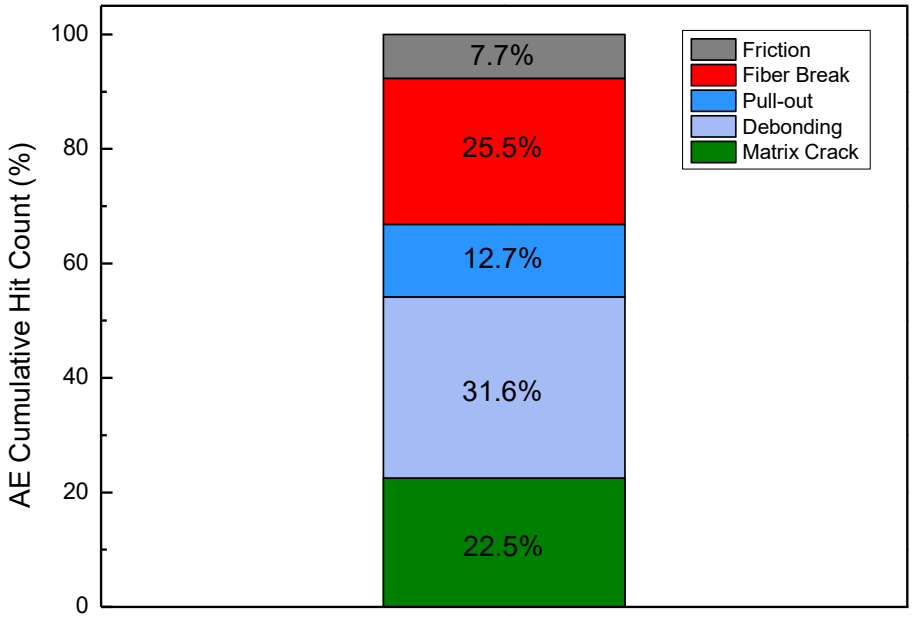

Source: author

In Figure 43, the total energy sum – i.e., the energy dissipated – is shown for each signal that was evaluated, in respect to the sample exhibited in Figure 41. As seen in the total number of hits, fiber break is responsible for 25.5 % of the acoustic emission hit counts. Even so, the energy for this signal is much higher (86.1 % of the total) in comparison with others. To

understand that it should be remembered that AE monitoring relies on the recording of transient elastic waves, resulting from a sudden strain energy release within a material due to the occurrence of microstructural changes. On these lines, the energy parameter is essentially the measurement of this stored strain energy that was released. Because the fiber acts as the composite reinforcement, it withstands the loads and stores the energy in the form of strain. When the fiber breaks (indicating that the composite is starting to fail), a high amount of energy is released. The same does not happen for other signals, such as matrix crack, which fails at lower stresses. As a result, matrix crack signals exhibit smaller energies.

The energy that is dissipated can be correlated with how crack deflection works. As the Al_2O_{3f}/Al_2O_3 composites utilize the WMC concept (section 2.2), the cracks propagate through the pores of the matrix, dissipating energy. When the matrix cracks reach the fibers, deflection takes place at the interface. This leads to interface debonding and fiber pull-out, providing higher toughness (BEN RAMDANE et al., 2017). Then, it is implied that for crack deflection to happen, the energy needs to be dissipated gradually by the damage mechanisms. If the energy was to be released all at once, the crack would propagate through the matrix and not be deflected, leading to a brittle fracture (as illustrated by the boundary curve according to He and Hutchinson, Figure 2). As seen in the training dataset values in Table 15, debonding and pull-out may have misclassifications because of their similarities. Then, from the crack deflection mechanisms, it can be concluded that the interfacial mechanisms have a major role in crack deflection, as it dissipates more energy.

Figure 43 – Quantification of energy dissipated for Al_2O_{3f}/Al_2O_3 minicomposite measured during tensile test. The signals that were quantified are fiber friction, fiber break, pull-out, interface debonding, and matrix crack.

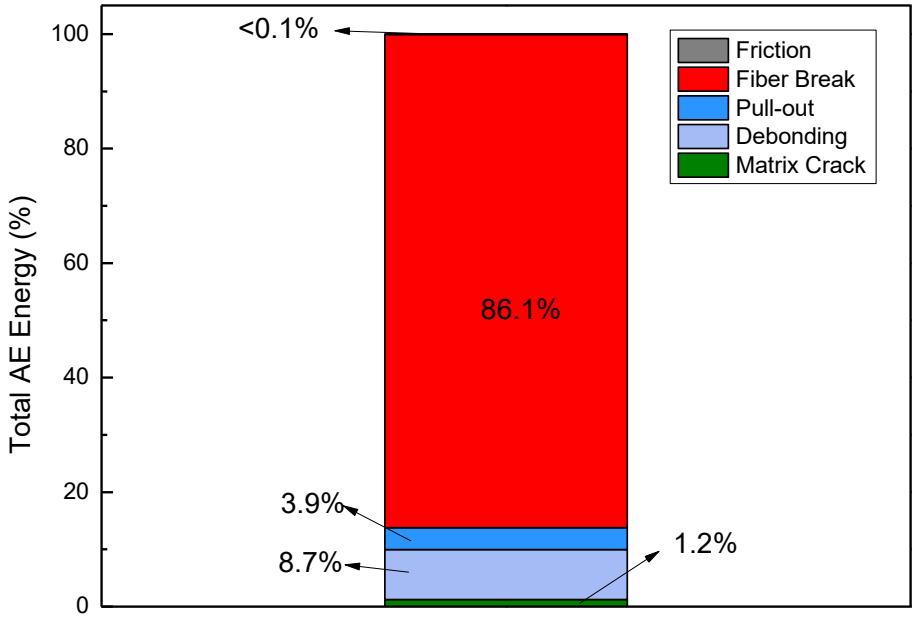

Source: author

4.3.2 Al_2O_{3f}/Al_2O_3 Composite Plates

The Al_2O_{3f}/Al_2O_3 composite plates were tested by 4-point bending tests. The average flexural strength was calculated to be 136±18 MPa. The damage development for a selected sample is exhibited in Figure 44.

Since these composites were subjected to 4-point bending tests; the lower part of the sample is under tensile stresses, while the upper part is under compression. This is different from the tensile tests previously analyzed. Since the materials are stronger under compression stresses (CHAWLA, 1993), the part which is under traction fails first. As the sample is being bent, the lower layer of the composite starts cracking. The crack front propagates until it reaches the next layer. Crack deflection occurs and other layers delaminate or fail, leading to fiber break and pull-out. Because the composite plate is under different stress states, fiber break may happen during different stages. Hence, it should be emphasized that these tests were expected to give a different classification behavior from the Al_2O_3 minicomposites.

In Figure 44, the first signals recognized were matrix crack and fiber break, along with smaller quantities of debonding, pull-out, and friction. It is assumed that the steady-like rate that fiber break was recognized is due to the stress state of the sample, occurring at various

moments as the composite is loaded. As the sample was loaded, it can be observed that the stress exhibited phases of increments and drops. This is related to fibers failure while the crack is deflected and propagated, resulting in a non-brittle behavior.

After the first drop in load, around 136 MPa, all signals excluding fiber break had a sudden increase in their relative occurrence rate through test time. For comparison, 8995 signals were measured by the AE monitoring device before this point, and 45365 after. Considering that the signals recognition performed well, this was caused by subsequent layers of the composite plate that started to fail at a faster rate. Consequently, a greater number of signals were recorded in a shorter amount of time, most of them associated with matrix cracking.

One thing that should be noted is that according to the literature, fiber break and pull-out are supposed to happen after matrix cracking and interface debonding. One of the explanations given to fiber break observed since the test beginning is the difference in stress states on the different layers of the composite. In addition, there could be flaws in some fibers, resulting in premature failure. However, fiber pull-out has an increase after the first load drop instead of presenting the same behavior as fiber break. One of the possibilities is that interface debonding enabled fiber pull-out to occur more frequently. Still, considering the similarity between debonding and pull-out (Table 15) and the precision values (Table 16), misclassifications between debonding and pull-out should also be weighted in this behavior.

Figure 44 – Damage development of Al_2O_{3f}/ Al_2O_3 composite plate 4-point bending test, illustrating the test stress, and cumulative hit count (CHIT) increase for each signal.

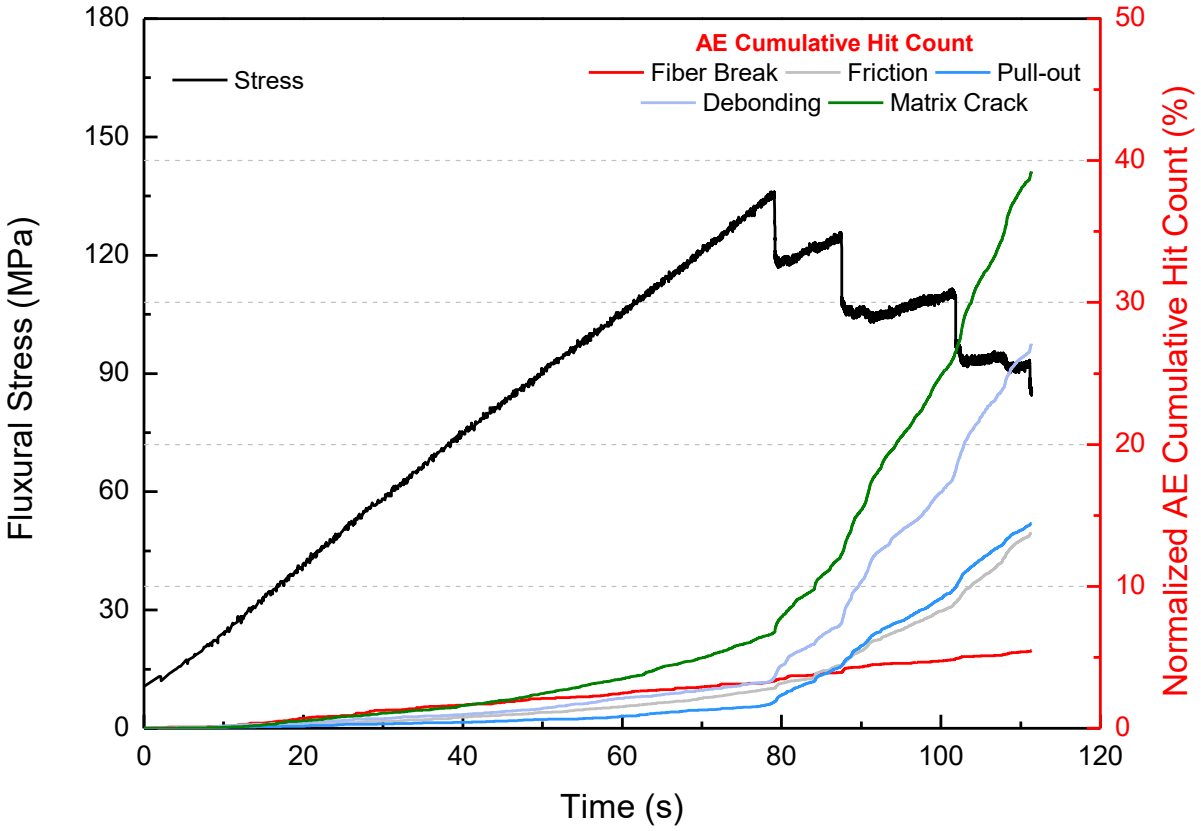

Source: author

The CHIT percentages associated with each signal are illustrated in Figure 45. In agreement with what was observed for minicomposites, a greater quantity of the signals measured is associated with matrix cracking and interface debonding. Still, an even higher number of signals related to matrix crack and fiber friction were observed for composite plates. This difference relies on the fact that the tensile stresses in the lower layers can cause more cracks to initiate and propagate in this region. Then, several matrix crack signals may be triggered. Concerning the quantity of frictional signals, as discussed earlier, friction might not be exclusive to fibers. Thus, more than one sort of friction signal may be recorded, such as friction between the composite layers that are failing.

Regarding the smaller percentages of fiber break in comparison with the previous test, this is assumed to be related to the way the composites were tested. Minicomposites were subjected to tensile tests. As so, more fibers are anticipated to break because the entire sample is under traction. However, the compression stresses on the composite plates delay the failure.

As a result, more opportunities for matrix crack and debond signals exist, minimizing fiber break.

Figure 45 – Quantification of cumulative hit count (CHIT) for Al_2O_{3f}/Al_2O_3 composite plate measured during 4-point bending test. The signals that were quantified are fiber friction, fiber break, pull-out, interface debonding, and matrix crack.

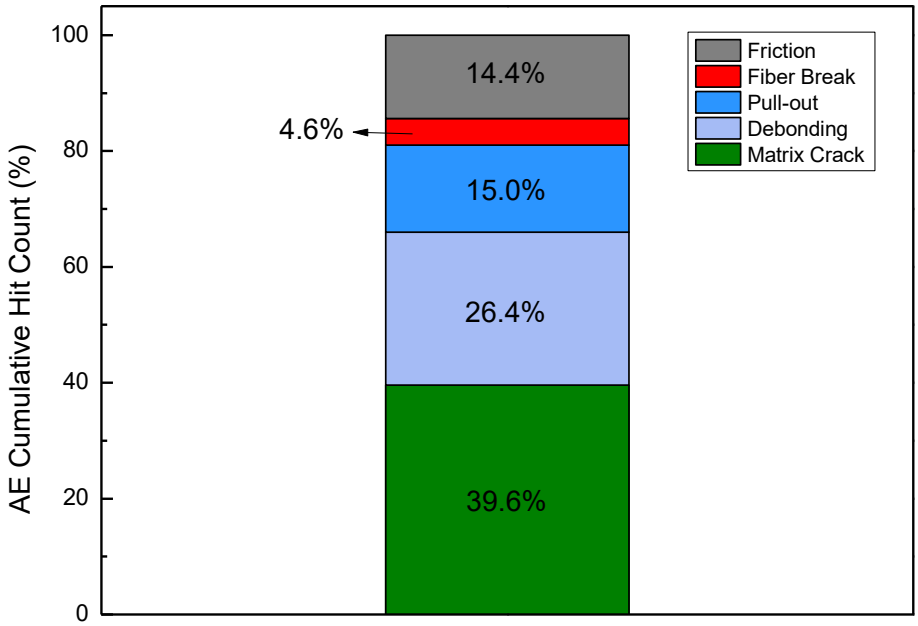

Source: author

Analyzing the dissipated energy in Figure 46, a behavior analogous to the one seen for minicomposites in Figure 43 was observed. The main differences occurred because more matrix cracking, and less fiber break signals were measured for composite plates. Thus, the distribution of energy dissipated is altered because of the change in these sources. Due to the reduced percentage of fiber break events, debonding is responsible for dissipating 35.2% of the total energy. From the crack deflection mechanisms, matrix crack dissipates the least amount, followed by fiber pull-out and interface debonding. Hence, in comparison with the minicomposites a greater portion of the energy dissipated is attributed to the deflection mechanisms, adding up to 57%, and not fiber break which is responsible for 42.7% of the total energy dissipated.

Figure 46 – Quantification of energy dissipated for Al_2O_{3f}/Al_2O_3 composite plate measured during 4-point bending test. The signals that were quantified are fiber friction, fiber break, pull-out, interface debonding, and matrix crack.

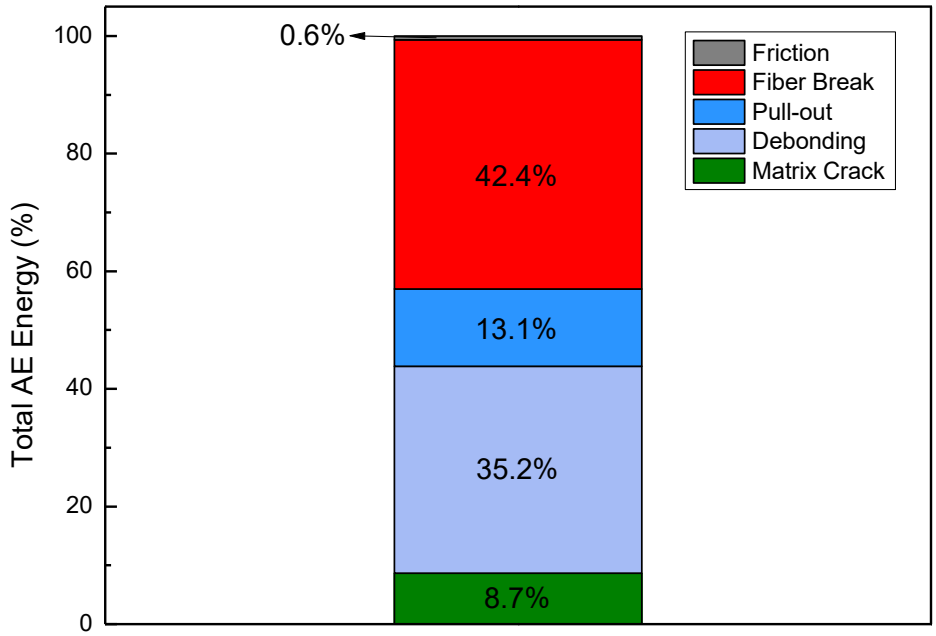

Source: author

4.3.3 C_f/SiC Composite Plates

This subsection concerns the damage mechanisms evaluation for C_f/SiC composites. The focus here is on the damage development recognition, as well as comparison with previous results from Almeida et al. (2019b). The comparison aims to provide further verification of the model performance, as well as to elucidate improvements that can be made.

The C_f/SiC composite plates were first subjected to fatigue tests. The number of fatigue cycles was 200, 10,000, and 2,000,000. Then, the samples were tensile tested until failure. The tensile tests were performed in conjunction with AE monitoring. An as-produced sample (not subjected to fatigue) was also tested for comparison. Only the data gathered during the tensile tests was analyzed. This permits the assessment of microstructure changes due to the number of fatigue cycles, which in retrospect results in changes in the damage development and AE signals measured.

For better comprehension of the damage evolution, the tensile strength and elastic modulus measured for each test condition are illustrated in Table 17. The AE signals measured were plotted against the tensile test data and are exhibited in Figure 47 for all testing conditions.

It should be emphasized that because of the scarce number of samples, differences in the composite preparation and structure should be considered as one of the reasons for the results measured.

Observing the tensile strength and elastic modulus values, excluding the sample loaded for 200 cycles, the tensile strength increases with the number of fatigue cycles. In contrast, the elastic modulus decreases, maintaining a mean value of 25 GPa after 10,000 cycles. The reason for this is that increasing the number of loading cycles may trigger lower energy microstructure changes. Hence, these changes – e.g., matrix cracking; fiber displacement – are believed to be related to a relief of internal stress caused by the damage onset during loading cycles. While a higher tensile strength is achieved, a reduced elastic modulus is obtained due to already sustained damage (MEI; CHENG, 2011).

Regarding the elastic modulus plateau after 10,000 cycles, it is associated with the sample fatigue behavior. As the number of cycles progresses, further damage only occurs at a higher level of stress. Therefore, a saturation level of damage must exist, where new damage is slowly generated during the loading cycles until a stable state – saturation – is reached. For these experiments, the stable state is after 10,000 cycles (ALMEIDA et al., 2019b). The outcome of this behavior can be perceived in Figure 47. For this reason, the AE signals from fatigued composite plates are measured later during the tensile test and at higher stresses.

Table 17 – Mechanical properties measured during C_f/SiC tensile tests.

Sample	Tensile Strength (MPa)	Elastic Modulus (GPa)
As-produced	75.4	35.6
200 cycles	69.7	27.4
10,000 cycles	84.0	24.9
2,000,000 cycles	99.4	25.1

Source: Adapted from ALMEIDA et al. (2019b, p. 2247)

Figure 47 – Damage development of C_f/SiC composite plate tensile test, illustrating the test stress, and normalized cumulative hit count (CHIT) increase for each signal. Four samples are Illustrated, (a) as-produced; (b) 200 cycles; (c) 10,000 cycles; and 2,000,000 cycles.

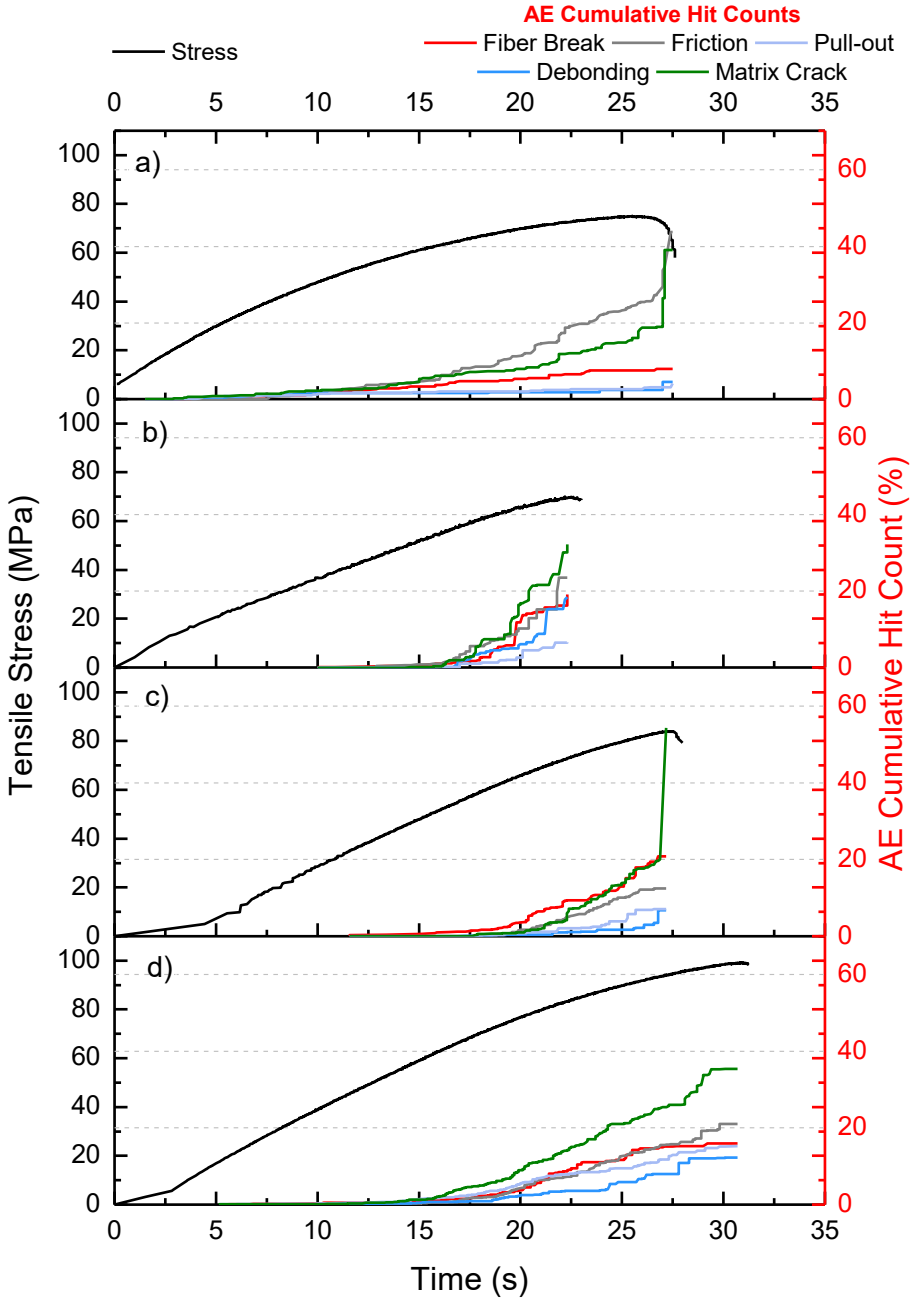

Source: author

For evaluating the damage evolution, it is important to consider the C_f/SiC composite plate structure. Because of the fiber reinforcement complexity (Figure 16), the assessment of damage is challenging to understand through conventional methods alone, such as SEM. By combining AE monitoring with the supervised ML model, it is possible to identify the damage. This can be used to complement other methods. On these lines, all stress curves showed a non-

linear (quasi-plastic) behavior as a consequence of crack deflection mechanisms. Starting with the as-produced sample, most of the signals measured are associated with matrix cracking and fiber friction. Since this composite was not previously fatigued, cracking is more prone to happen. In addition, the higher amount of fiber friction in comparison with the other samples is assumed to be related to the lack of stress relief. To support that, the fracture surface of the as-produced sample is shown (Figure 48a). According to Almeida et al. (2019b), the fracture surface consisted mainly of clustered fibers and little sign of fiber debonding. Thus, the damage recognition and quantification results obtained using the ML model agree with what was observed back then, where only raw data of AE monitoring and SEM analysis was available. The clustered fibers result in a smaller number of individual fiber break, pull-out, and debonding. Consequently, the AE signals are mostly from matrix cracking and friction between the interfaces.

Comparing the behavior of the as-produced sample with the fatigued composites, the latter presented a rather different damage development. Considering the fiber reinforcement complexity, a clear behavior cannot be inferred and compared to the literature. Nevertheless, because the samples were already pre-damaged due to the loading cycles with a threshold of 58.2 MPa, more fiber break, pull-out, and debonding are expected here due to the weaker interfacial bonding. Observing the CHIT for each signal in Figure 47, it is noticed that while matrix cracking is still prevalent, there is a decrease in frictional signals for post-fatigue samples, while the others increase. This is believed to be related to the relief of internal stress introduced earlier, as well as a reduction of the fiber/matrix interface strength because of the fatigue cycles. The pre-sustained damage allows fiber break, pull-out, and debonding at a higher degree. This is supported by Figure 48b, exhibiting the fracture surface for the 2,000,000 cycles sample. The fiber/matrix friction during the fatigue tests most likely caused interface deterioration. This facilitates the activity of interfacial mechanisms and individual fiber break. Then, a fracture composed of clustered and individual fibers was possible, opposite to the as-produced sample.

Figure 48 – SEM images illustrating the fracture surface of Cf/SiC composite plate (a) as-produced – virgin – and (b) post-fatigue after 2,000,000 cycles. Fiber clusters and single fiber fractures are highlighted.

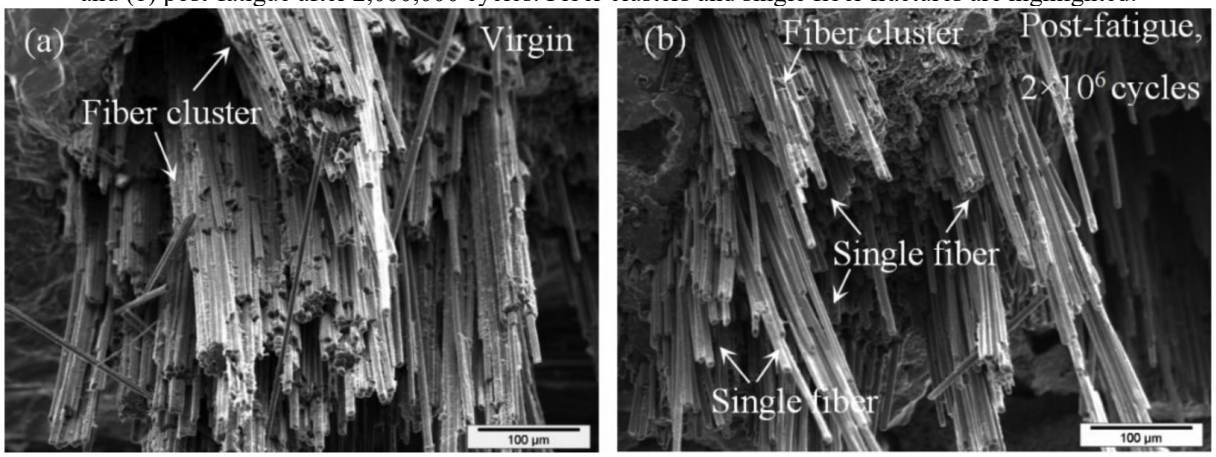

Source: ALMEIDA et al (2019b, p. 2248)

Further information on the damage can be obtained by analyzing the bar graphs presented in Figure 49 and Figure 50, showing the percentages of AE CHIT and energy for all testing conditions. As previously discussed, the fatigued samples exhibited a decrease in frictional signals, corresponding to 43.8% to a range of 11.4 ~ 22.9% depending on the number of loading cycles. The decrease is accompanied by an overall increase in fiber break and pull-out, and less apparent debonding, which is assumed to be a result of interface deterioration. The interface deterioration facilitates the activity of this type of damage.

Considering the damage development of the fatigued specimens, the behavior of the 10,000 cycles sample needs to be pointed. There is a sudden increase in the matrix crack CHIT close to the failure stress. In specific, this is due to a cascaded hit – when one hit generates other hits – that was probably triggered due to the higher stresses. Because no more data with the same test condition was available for further assessment, this behavior was treated as an outlier. Thus, the higher percentage value of matrix cracking for the 10,000 cycles sample is associated with the cascaded hit that was triggered.

Figure 49 – Quantification of CHIT for C_f/SiC composite plates measured during tensile tests. The signals that were quantified are fiber friction, fiber break, pull-out, interface debonding, and matrix crack. Four test conditions are illustrated: as-produced, and pre-fatigued for 200, 10,000, and 2,000,000 loading cycles.

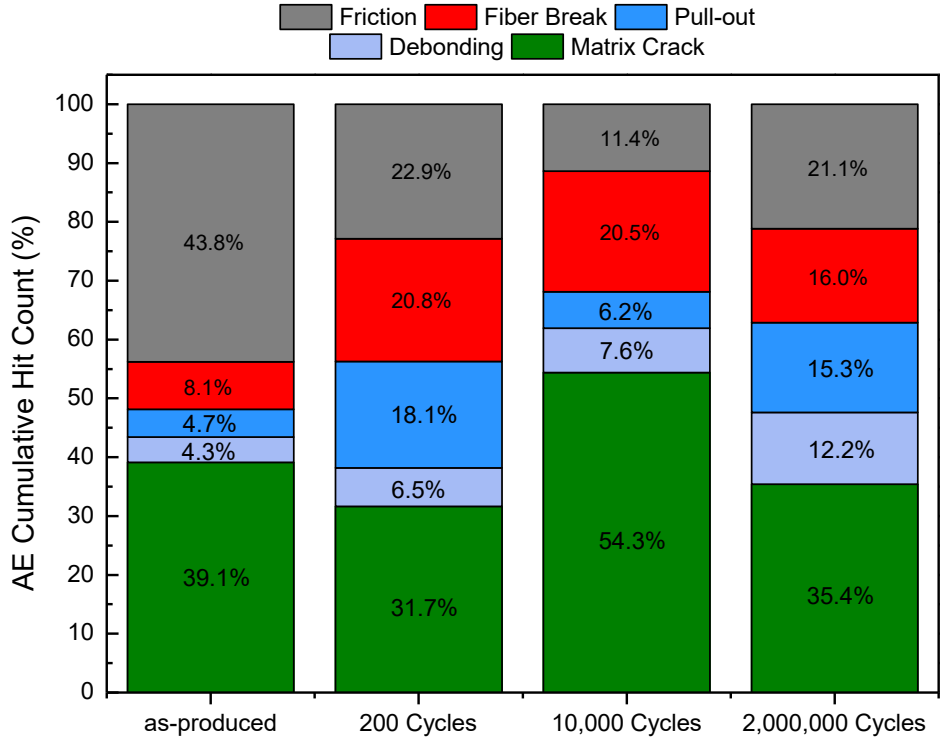

Source: author

Observing the total energy dissipated results (Figure 50), it is different from what was observed for the Al_2O_{3f}/Al_2O_3 composites. While the alumina composites seemed to dissipate more energy with fiber/matrix interface mechanisms, the C_f/SiC composite plates exhibited more energy dissipated as matrix cracking, with an increase in pull-out and debonding for 200 and 2,000,000 cycles samples. Considering that the results remained different even for samples that underwent fatigue tests, these differences are attributed to the distinct structures of the Al_2O_{3f}/Al_2O_3 and C_f/SiC composites. While the Al_2O_{3f}/Al_2O_3 composites were composed of longitudinal fibers (minicomposites) and 2D reinforced 0/90 degrees fibers (composite plates), the C_f/SiC were composed of a 2.5D fiber preform, made of needle-punched short fiber webs and 0/90 degrees fiber cloths (Figure 16). Therefore, the damage development changes, as well as how the energy is dissipated. In respect to the sample tensile tested post 10,000 fatigue cycles, most of the energy (57.9%) is related to matrix cracking. This was caused by the consecutive matrix cracking hits recognized near the test end, resulting in more energy dissipation.

Figure 50 – Quantification of energy dissipated for C_f/SiC composite plates measured during tensile tests. The signals that were quantified are fiber friction, fiber break, pull-out, interface debonding, and matrix crack. Four test conditions are illustrated: as-produced, and pre-fatigued for 200, 10,000, and 2,000,000 loading cycles.

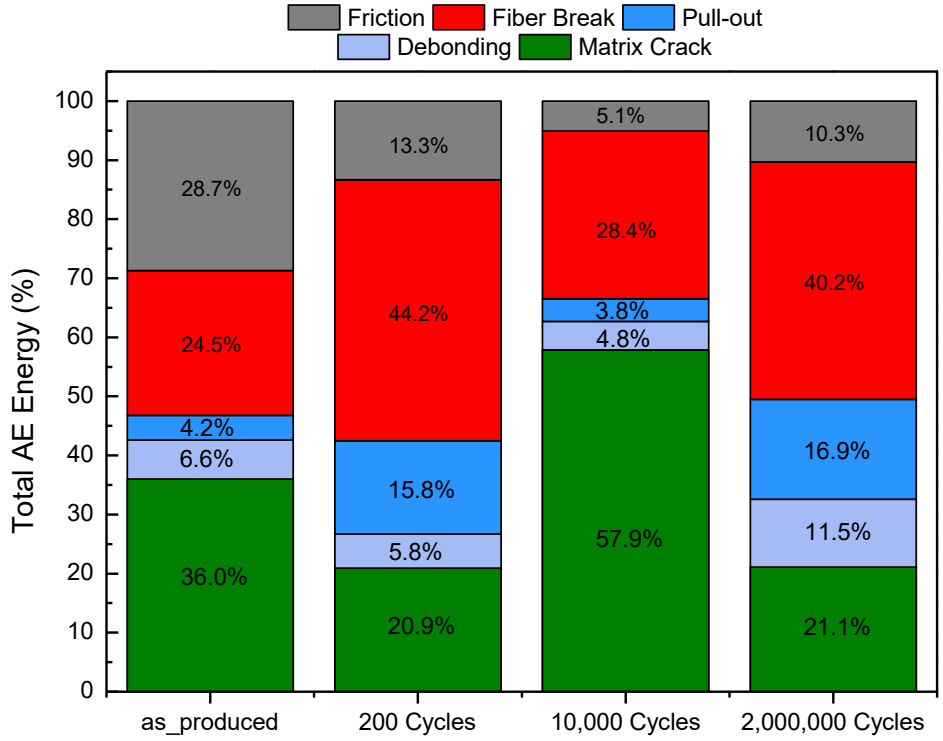

Source: author

Through the analysis of the AE data complemented by a supervised ML model, it was possible to quantify which mechanisms are acting during the damage evolution. The above results are in accordance with what was observed in Almeida et al. (2019b). In this previous work, the applied methods allowed primarily a qualitative viewing of the damage mechanisms. The AE signals were assumed to be related mostly to matrix cracking and fiber friction, with an increase of interface-related mechanisms for samples that had undergone fatigue tests. In addition, the results were supported by the SEM images. With the application of a supervised ML model, quantitative-oriented results were possible, and this approach proves fruitful for quantifying the damage mechanisms. Nevertheless, evaluating the training dataset and the results obtained, misclassifications between interfacial mechanisms, and between matrix cracking and friction need to be considered.

5. CONCLUSION

Contemplating the objective of this work, three main points were proposed: The analysis of each damage mechanism separately; the obtention of a supervised ML model; and the damage quantification and assessment in Al_2O_{3f}/Al_2O_3 and C_f/SiC CMCs. The results presented in the previously brings up the following conclusions:

- The procedure to isolate the signals associated with each damage mechanism was successful and enabled the obtention of a training dataset. Fiber break, matrix cracking, and friction signals were simple to label. However, fiber pull-out and interface debonding signals were generated together with other mechanisms. Hence, information from previous tests was used for filtering the wanted signals;
- Similarities between the AE parameters affected the precision scores for matrix cracking and pull-out. Still, an average k-fold cross validation score of 88% was obtained, meaning that the model can discern between the AE signals but is prone to misclassifications among lower precision damage sources;
- Regarding the model performance:
    - For Al_2O_{3f}/Al_2O_3 composites the classification results was close to what was expected from the literature. The damage on-set started with matrix cracking and interface debonding. With the load increase, fiber break and pull-out were facilitated, leading to the composite failure. Divergences to the literature were assumed to be related to flaws present in the material microstructure, as well as misclassifications. Frictional events were observed during various testing times and loads. The conclusion was that friction was caused between fiber/fiber and fiber/matrix interfaces, and both presented similar AE signal values.
    - For Al_2O_{3f}/Al_2O_3 minicomposites, considering that the stress state was completely tensile, more fiber break was observed in the classification. Consequently, a greater portion of energy dissipation was associated with fiber break.
    - The Al_2O_{3f}/Al_2O_3 composite plates undergone 4-point bending tests. Because of the differences in stress state in comparison with the minicomposites, a greater portion of energy dissipation is conferred to crack deflection mechanisms

(matrix cracking, debonding and pull-out). Additionally, the stress state subjected triggered the failure of few layers early. This resulted in fiber break being recognized at various load stages.

- The classification of the AE signals from C_f/SiC composite plates permitted the behavior comparison with previous works, in which the results obtained here supported the past observations. More events associated with matrix cracking and debonding happened due to the complex composite structure. The decrease in friction signals post-fatigue tests is assumed to be caused by a relief of internal stress that occurred during the fatigue cycles. In addition, a greater quantity of debonding, pull-out, and fiber break events were observed when compared with the as-produced sample. This is related to interface deterioration that took place during the loading cycles.

As a concluding remark, the advancements in ML set up the path for novel techniques to aid the understanding of damage mechanisms in composites. By combining these techniques with AE monitoring, it is possible to assess the damage initiation and evolution as a composite is loaded. This can shed light on which mechanism has higher importance for achieving crack deflection, and thus perform structure adjustments based on these observations. This thesis aims to show the prospective of how broad these techniques for materials characterization are. Still, some improvements need to be taken care of. Suggestions for future works are:

- Investigate other mechanical tests for isolating interface debonding and fiber pull-out signals;
- Compare the damage mechanism quantification between an unsupervised and a supervised machine learning model; or assess the classification performance using different techniques, such as neural networks;
- Perform an in-depth analysis of the classification, complementing the quantification results with image techniques such as CT and SEM to observe the damage.

6. REFERENCES

3M COMPANY. **Ceramic Fibers and Textiles Ceramic Fibers and Textiles: Technical Reference Guide**. St. Paul, MN: [s.n.].

ADDIN, O. et al. A Naïve-Bayes classifier for damage detection in engineering materials. **Materials and Design**, v. 28, n. 8, p. 2379–2386, 2007.

AHN, B. K. et al. Criteria for crack deflection/penetration criteria for fiber-reinforced ceramic matrix composites. **Composites Science and Technology**, 1998.

AL-MASRI, A. **What Are Overfitting and Underfitting in Machine Learning?** Disponível em: <https://towardsdatascience.com/what-are-overfitting-and-underfitting-in-machine-learning-a96b30864690>. Acesso em: 25 nov. 2021.

ALMEIDA, R. S. M. et al. Thermal Exposure Effects on the Strength and Microstructure of a Novel Mullite Fiber. **Journal of the American Ceramic Society**, v. 99, n. 5, p. 1709–1716, maio 2016.

ALMEIDA, R. S. M. et al. Obtaining complex-shaped oxide ceramic composites via ionotropic gelation. **Journal of the American Ceramic Society**, v. 102, n. 1, p. 53–57, jan. 2019a.

ALMEIDA, R. S. M. et al. Damage analysis of 2.5D C/C-SiC composites subjected to fatigue loadings. **Journal of the European Ceramic Society**, v. 39, n. 7, p. 2244–2250, 1 jul. 2019b.

ALPAYDIN, E. Combining Pattern Classifiers: Methods and Algorithms (Kuncheva, L.I.; 2004) [book review]. **IEEE Transactions on Neural Networks**, v. 18, n. 3, p. 964–964, maio 2007.

ASM INTERNATIONAL HANDBOOK COMMITTEE. **ASM Handbook, Volume 21**. Ohio: Materials Park: ASM International, 2001. v. 21

ASTM C1360-17. Standard Practice for Constant-Amplitude, Axial, Tension-Tension Cyclic Fatigue of Continuous Fiber-Reinforced Advanced Ceramics at Ambient Temperatures. 2017.

AUERKARI, P. Mechanical and physical properties of engineering alumina ceramics. **VTT Tiedotteita - Valtion Teknillinen Tutkimuskeskus**, n. 1792, 1996.

BANSAL, N. P.; LAMON, J. **Ceramic Matrix Composites: Materials, Modeling and Technology**. 1. ed. Hoboken, New Jersey: Wiley-American Ceramic Society, 2015.

BEN RAMDANE, C. et al. Microstructure and mechanical behavior of a Nextel^{TM}610/alumina weak matrix composite subjected to tensile and compressive loadings. **Journal of the European Ceramic Society**, v. 37, n. 8, p. 2919–2932, 2017.

BRIGANTE, D. **New Composite Materials**. Cham: Springer International Publishing, 2014. v. 1

BROWNLEE, J. **Statistical Methods for Machine Learning Discover how to Transform Data into Knowledge with Python**. [s.l: s.n.].

CAMPBELL, F. C. **Manufacturing Processes for Advanced Composites**. 1. ed. [s.l.] Elsevier Science, 2004.

CHAWLA, K. K. **Ceramic matrix composites. Ceramic matrix materials.** 1. ed. [s.l.] Springer, 1993.

CHAWLA, K. K. Interface Engineering in Oxide Fiber/Oxide Matrix Composites. **International Materials Review**, v. 45, n. May 2000, p. 165–189, 2000.

DICARLO, J. A.; VAN ROODE, M. **Ceramic Composite Development for Gas Turbine Engine Hot Section Components**. Volume 2: Aircraft Engine; Ceramics; Coal, Biomass and Alternative Fuels; Controls, Diagnostics, and Instrumentation; Environmental and Regulatory Affairs. **Anais**. ASMEDC, jan. 2006.

DICARLO, J. A.; YUN, H.-M. Non-oxide (Silicon Carbide) Fibers. In: **Handbook of Ceramic Composites**. [s.l.] Springer US, 2005. p. 33–52.

DIN EN 658-3. Mechanische Eigenschaften von keramischen Verbundwerkstoffen bei Raumtemperatur - Teil 3: Bestimmung der Biegefestigkeit. 2002.

DIN EN 658-5. Mechanische Eigenschaften von keramischen Verbundwerkstoffen bei Raumtemperatur - Teil 5: Bestimmung der Scherfestigkeit im Drei-Punkt-Biegeversuch mit kurzem Auflagerabstand. 2005.

DIN EN 843-1. Mechanische Eigenschaften monolithischer Keramik bei Raumtemperatur - Teil 1: Bestimmung der Biegefestigkeit. 2008.

DIN EN 1007-4. Verfahren zur Prüfung der Faserverstärkungen - Teil 4: Bestimmung der Zugeigenschaften von Fasern bei Raumtemperatur. 2004.

DIN EN 1007-5. Verfahren zur Prüfung der Faserverstärkungen - Teil 5: Bestimmung der Verteilung von Zugfestigkeit und Zugdehnung von Fasern im Faserbündel bei Raumtemperatur. 2003.

DIN EN ISO 15732. Prüfverfahren zur Bestimmung der Bruchzähigkeit monolithischer Keramik bei Raumtemperatur an einseitig gekerbten Biegeproben (SEPB-Verfahren). 2004.

EGGERT, B. G. F. **EVALUATION OF DIFFERENT TESTING TECHNIQUES ON THE MECHANICAL PROPERTIES OF NOVEL OXIDE FIBERS**. Florianópolis, 2014. Trabalho de Conclusão de Curso (Não publicado), Universidade Federal de Santa Catarina.

EVANS, A. G.; ZOK, F. W. The physics and mechanics of fibre-reinforced brittle matrix composites. **Journal of Materials Science**, v. 29, n. 15, p. 3857–3896, 1994.

GHOLIZADEH, S. et al. Acoustic emission analysis for characterization of damage mechanisms in glass fiber reinforced polyester composite. **Australian Journal of Mechanical Engineering**, v. 16, n. 1, p. 11–20, 2018.

GIURGIUTIU, V. Impact and Acoustic Emission Monitoring for Aerospace Composites SHM. In: **Structural Health Monitoring of Aerospace Composites**. [s.l.] Elsevier, 2016. p. 317–394.

GOODFELLOW, I.; BENGIO, Y.; COURVILLE, A. **Deep Learning**. [s.l.] MIT Press, 2016.

HALVERSON, H. G.; CURTIN, W. A. Stress rupture in ceramic-matrix composites: Theory and experiment. **Journal of the American Ceramic Society**, v. 85, n. 6, p. 1350–1365, 2002.

HE, M. Y.; HUTCHINSON, J. W. **Kinking of a crack out of an interface Journal of Applied Mechanics, Transactions ASME**, 1989.

HONG, Y. et al. **Machine learning and artificial neural network accelerated computational discoveries in materials science. Wiley Interdisciplinary Reviews: Computational Molecular Science.** Blackwell Publishing Inc., 1 maio 2020.

KELLER, K. A.; JEFFERSON, G.; KERANS, R. J. Oxide-Oxide composites. In: **Handbook of Ceramic Composites**. [s.l.] Springer US, 2005. p. 377–421.

KENDALL, M. G. A NEW MEASURE OF RANK CORRELATION. **Biometrika**, v. 30, n. 1–2, p. 81–93, 1 jun. 1938.

KIM, J. K.; ZHOU, L. M.; MAI, Y. W. Interfacial debonding and fibre pull-out stresses - Part III Interfacial properties of cement matrix composites. **Journal of Materials Science**, v. 28, n. 14, p. 3923–3930, 1993.

KOCH, D. et al. Evaluation of Mechanical Properties and Comprehensive Modeling of CMC with Stiff and Weak Matrices. **Advances in Science and Technology**, v. 45, p. 1435–1443, 2006.

KOCH, D.; TUSHTEV, K.; GRATHWOHL, G. Ceramic fiber composites: Experimental analysis and modeling of mechanical properties. **Composites Science and Technology**, v. 68, n. 5, p. 1165–1172, 2008.

KOSTOPOULOS, V. et al. On the identification of the failure mechanisms in oxide/oxide composites using acoustic emission. **NDT and E International**, v. 36, n. 8, p. 571–580, 2003.

KOSTOPOULOS, V.; LOUTAS, T.; DASSIOS, K. Fracture behavior and damage mechanisms identification of SiC/glass ceramic composites using AE monitoring. **Composites Science and Technology**, v. 67, n. 7–8, p. 1740–1746, 2007.

KRENKEL, W. **Ceramic Matrix Composites**. [s.l.] Wiley, 2008.

LAMON, J. Properties and Characteristics of SiC and SiC/SiC Composites. In: **Comprehensive Nuclear Materials**. [s.l.] Elsevier, 2012. v. 2p. 323–338.

LI, L. et al. Cluster analysis of acoustic emission signals for 2D and 3D woven glass/epoxy composites. **Composite Structures**, v. 116, n. 1, p. 286–299, 2014.

MAILLET, E. et al. Combining in-situ synchrotron X-ray microtomography and acoustic emission to characterize damage evolution in ceramic matrix composites. **Journal of the European Ceramic Society**, v. 39, n. 13, p. 3546–3556, 2019.

MATHEWS, F. L.; RAWLINGS, R. D. **Composite materials: Engineering and science**. [s.l.] CRC Press, 1994. v. 16

MEI, H.; CHENG, L. Stress-dependence and time-dependence of the post-fatigue tensile behavior of carbon fiber reinforced SiC matrix composites. **Composites Science and Technology**, v. 71, n. 11, p. 1404–1409, 28 jul. 2011.

MOEVUS, M. et al. Analysis of damage mechanisms and associated acoustic emission in two SiCf/[Si-B-C] composites exhibiting different tensile behaviors. Part II: Unsupervised acoustic emission data clustering. **Composites Science and Technology**, v. 68, n. 6, p. 1258–1265, 2008a.

MOEVUS, M. et al. Analysis of damage mechanisms and associated acoustic emission in two SiC/[Si-B-C] composites exhibiting different tensile behaviors. Part I: Damage patterns and acoustic emission activity. **Composites Science and Technology**, v. 68, n. 6, p. 1250–1257, 2008b.

MOMSON, J. A.; KAUTH, K. M. Design and Analysis of a CMC Turbine Blade Tip Seal for a Land-Based Power Turbine. In: **Ceramic Engineering and Science Proceedings**. [s.l: s.n.]. v. 19p. 249–256.

MORSCHER, G. N.; PARTHASARATHY, T. A.; CINIBULK, M. K. 5.6 Mechanical Behavior of Non-Oxide Fiber-Reinforced CMCs at Elevated Temperature: Environmental Effects. In: **Comprehensive Composite Materials II**. [s.l.] Elsevier, 2018. v. 8p. 158–173.

MOULOODI, S. et al. What can artificial intelligence and machine learning tell us? A review of applications to equine biomechanical research. **Journal of the Mechanical Behavior of Biomedical Materials**, v. 123, 1 nov. 2021.

MOURITZ, A. P. Nondestructive inspection and structural health monitoring of aerospace materials. In: **Introduction to Aerospace Materials**. [s.l.] Elsevier, 2012. p. 534–557.

MUIR, C. et al. A machine learning framework for damage mechanism identification from acoustic emissions in unidirectional SiC/SiC composites. **npj Computational Materials**, v. 7, n. 1, p. 146, 13 dez. 2021.

NAWY, E. Fiber-Reinforced Composites. In: **Concrete Construction Engineering Handbook**. [s.l.] CRC Press, 2008. p. 616.

ONO, K. Acoustic Emission in Materials Research-a Review. **Journal of acoustic emission**, v. 29, p. 284–309, 2011.

PAPPAS, Y. Z.; MARKOPOULOS, Y. P.; KOSTOPOULOS, V. Failure mechanisms analysis of 2D carbon/carbon using acoustic emission monitoring. **NDT and E International**, v. 31, n. 3, p. 157–163, 1998.

PARK, S.-J.; SEO, M.-K. Types of Composites. In: **Interface Science and Composites**. [s.l.] Academic Pre, 2011. v. 18p. 501–629.

PARLIER, M.; RITTI, M.-H.; JANKOWIAK, A. Potential and Perspectives for Oxide / Oxide Composites. **Journal AerospaceLab**, n. 3, p. 1–12, 2011.

PEDREGOSA, F. et al. Scikit-learn: Machine Learning in Python. **Journal of Machine Learning Research**, v. 12, n. 1, p. 2825–2830, 2011.

RAMPRASAD, R. et al. **Machine learning in materials informatics: Recent applications and prospects npj Computational Materials,** Nature Publishing Group, 1 dez. 2017.

RÜDINGER, A.; NÖTH, A.; PRITZKOW, W. E. C. Oxide Ceramic Matrix Composites – Manufacturing, Machining, Properties and Industrial Applications. **Ceramic Applications**, v. 3, n. September, p. 48–54, 2015.

SALEM, J.; SINGH, D. **Mechanical Properties and Performance of Engineering Ceramics and Composites XI**. Hoboken, NJ, USA: John Wiley & Sons, Inc., 2017.

SAUSE, M. G. R. Identification of failure mechanisms in fiber reinforced composites by acoustic emission analysis. **Safety, Reliability, Risk and Life-Cycle Performance of Structures and Infrastructures - Proceedings of the 11th International Conference on Structural Safety and Reliability, ICOSSAR 2013**, n. August, p. 347–354, 2013.

SHEHADEH, M.; STEEL, J. A.; REUBEN, R. L. Acoustic Emission Source Location for Steel Pipe and Pipeline Applications: The Role of Arrival Time Estimation. **Proceedings of the Institution of Mechanical Engineers, Part E: Journal of Process Mechanical Engineering**, v. 220, n. 2, p. 121–133, 12 maio 2006.

SHINAVSKI, R. J. 5.2 Non-Oxide/Non-Oxide Ceramic Matrix Composites – Composite Design for Tough Behavior. In: **Comprehensive Composite Materials II**. [s.l.] Elsevier, 2018. v. 8p. 19–40.

SHIWA, M. et al. **Fracture Mechanisms in Unnotched and Notched SiC/SiC Composites Studied by Acoustic Emission Analysis,** Materials Transactions, 1995.

STEIBEL, J. Ceramic matrix composites taking flight at GE Aviation. **American Ceramic Society Bulletin**, v. 98, p. 30–33, 2019.

SUZUKI, H. et al. Wavelet transform of acoustic emission signals. **J. Acoust. Emiss.**, v. 14, p. 69–84, 1996.

SZWEDA, A. et al. **Development and Evaluation of Hybrid Oxide/Oxide Ceramic Matrix Composite Combustor Liners**. Volume 1: Turbo Expo 2005. **Anais**...ASMEDC, 1 jan. 2005.

TORAY INDUSTRIES. **T700G STANDARD MODULUS CARBON FIBER**.

TRIPATHI, G. et al. Classification of micro-damage in piezoelectric ceramics using machine learning of ultrasound signals. **Sensors (Switzerland)**, v. 19, n. 19, 2019.

TUSHTEV, K.; MARTIN ALMEIDA, R. SAINT. 5.5 Oxide/Oxide CMCs – Porous Matrix Composite Systems; Composites with Interface Coatings. In: **Comprehensive Composite Materials II**. [s.l.] Elsevier, 2018. v. 8p. 130–157.

UNNORSSON, R. Hit Detection and Determination in AE Bursts. **Acoustic Emission - Research and Applications**, p. 1–20, 2013.

VAN STEEN, C. et al. Localization and characterization of corrosion damage in reinforced concrete by means of acoustic emission and X-ray computed tomography. **Construction and Building Materials**, v. 197, p. 21–29, 10 fev. 2019.

VOLKMANN, E. et al. Influence of heat treatment and fiber orientation on the damage threshold and the fracture behavior of Nextel fiber-reinforced Mullite-SiOC matrix composites analysed by acoustic emission monitoring. **Journal of Materials Science**, v. 49, n. 22, p. 7890–7899, 2014.

VOLKMANN, E. et al. Assessment of three oxide/oxide ceramic matrix composites: Mechanical performance and effects of heat treatments. **Composites Part A: Applied Science and Manufacturing**, v. 68, p. 19–28, 2015.

WANG, Y. et al. Mechanical Properties of 2D C/SIC Composites with Two Different Carbon Tows. **Advanced Composites Letters**, v. 17, n. 2, p. 096369350801700, 1 mar. 2008.

WEIBULL, W. Wide applicability. **Journal of applied mechanics**, v. 103, p. 293–297, 1951.

WOLFENDEN, A.; VAN DER ZWAAG, S. The Concept of Filament Strength and the Weibull Modulus. **Journal of Testing and Evaluation**, v. 17, n. 5, p. 292, 1989.

XU, D. et al. Damage mode identification of adhesive composite joints under hygrothermal environment using acoustic emission and machine learning. **Composite Structures**, v. 211, p. 351–363, 1 mar. 2019.

ZHANG, L. et al. Real-time monitoring of welding process using air-coupled ultrasonics and acoustic emission. **The International Journal of Advanced Manufacturing Technology**, v. 101, n. 5–8, p. 1623–1634, 23 abr. 2018.

ZOK, F. W.; LEVI, C. G. Mechanical Properties of Porous-Matrix Ceramic Composites. **Advanced Engineering Materials**, v. 3, n. 1–2, p. 15–23, 2001.

ANNEX A – ADDITIONAL PRE-TEST AND FINAL TEST PLOTS

Figure A1 – Selected stress-displacement for pre-test samples: single and ten filament, fiber bundle, and fiber pull-out.

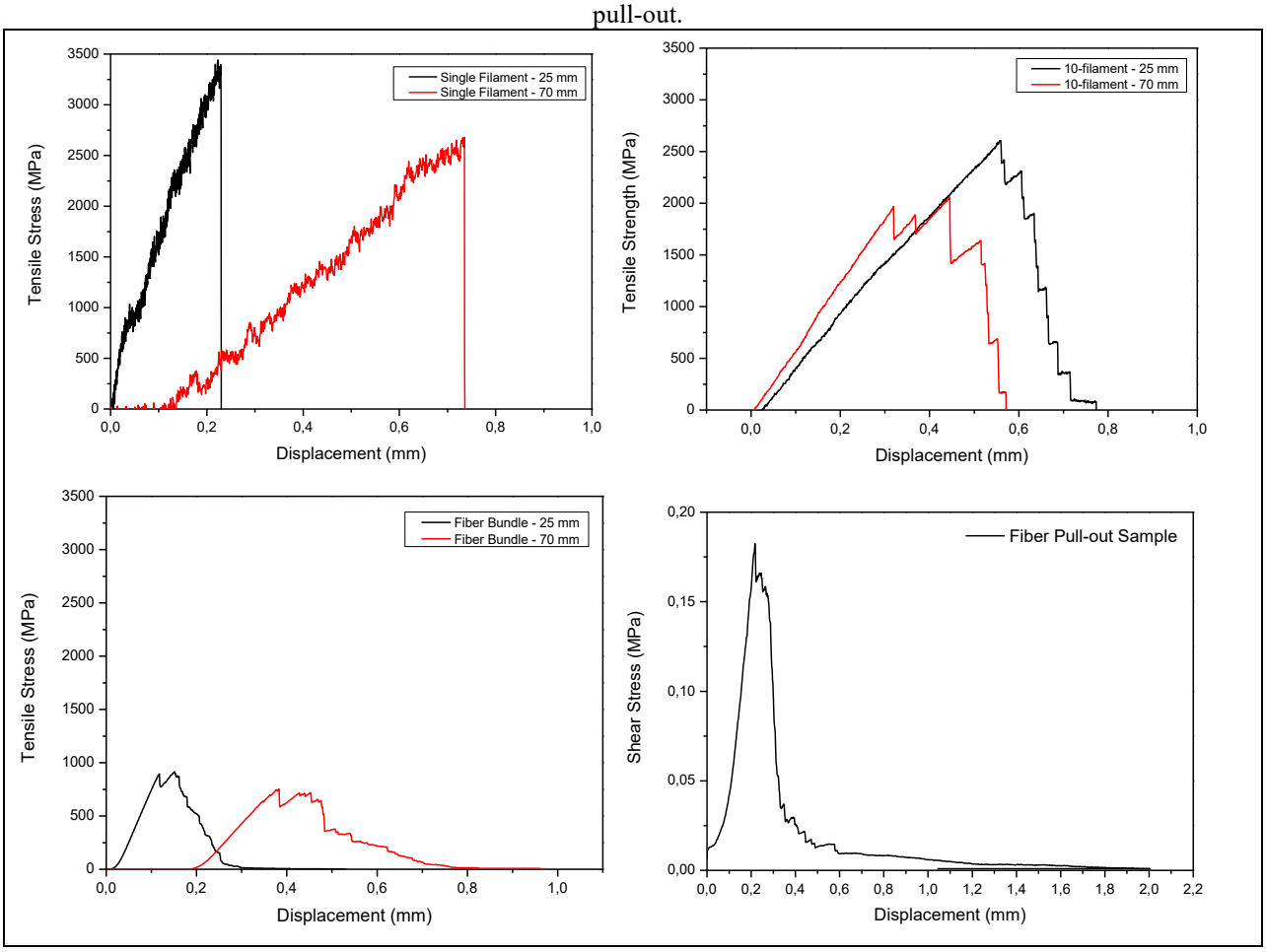

Source: author

Figure A2 – Selected stress-strain curves for pre-test samples: matrix and composite plate.

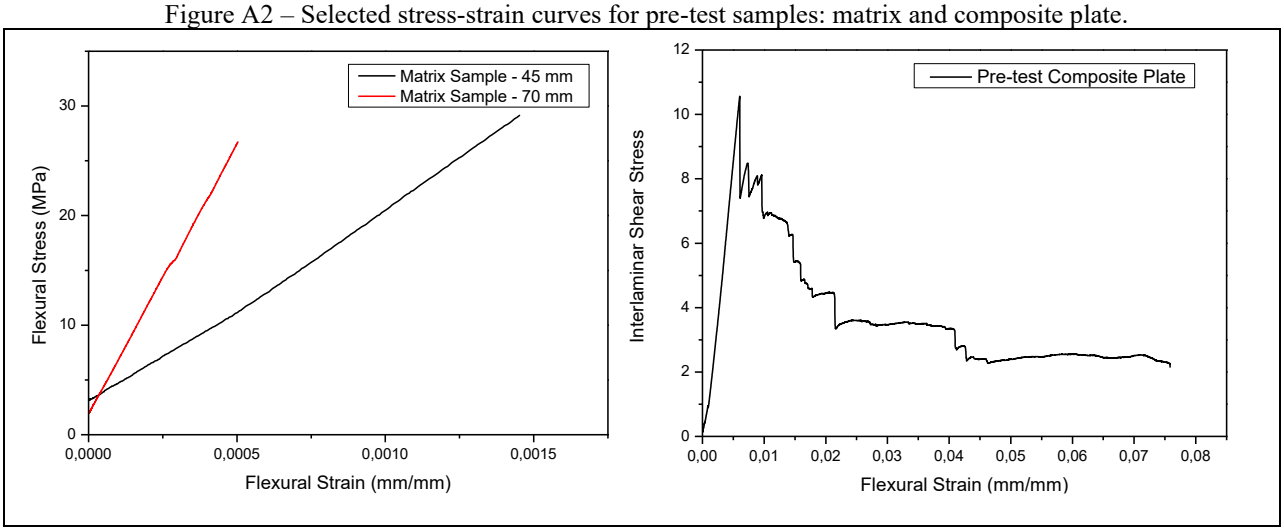

Source: author

Figure A3 – Selected Al_2O_{3f}/ Al_2O_3 minicomposite plots, exhibited in the following order: Damage evolution, CHIT, and energy quantification for each signal.

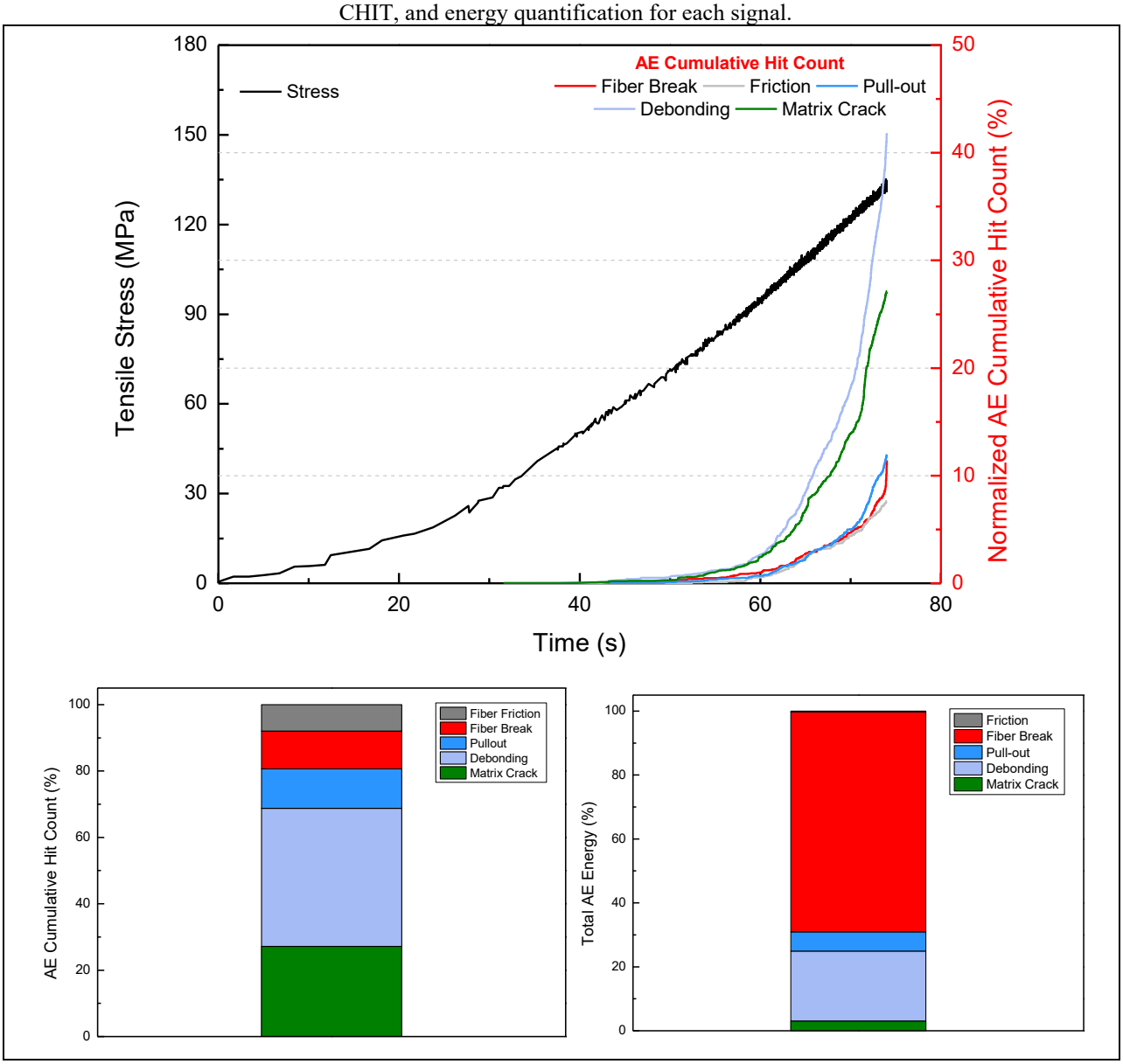

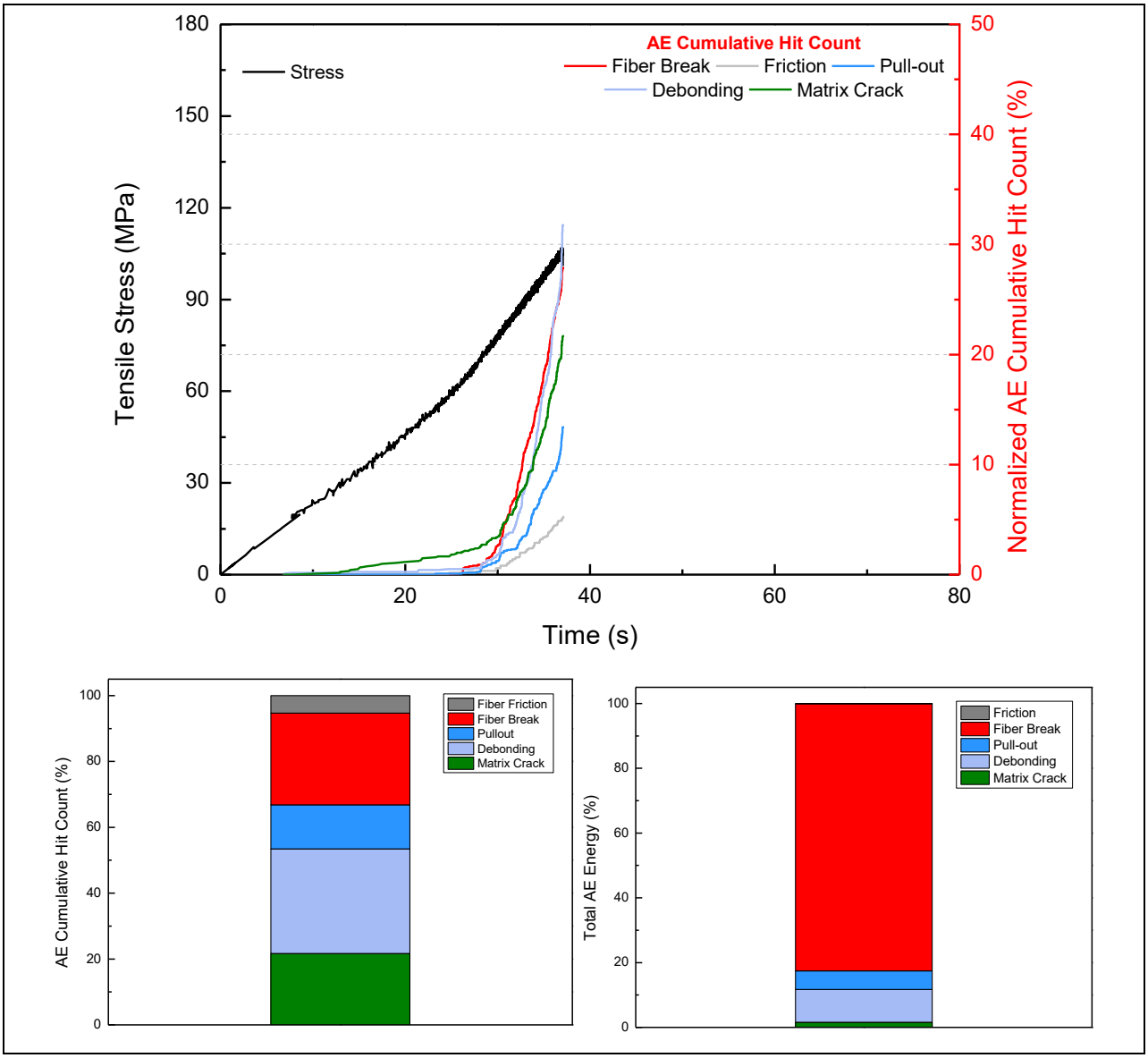
Stress
AE Cumulative Hit Count
Fiber Break
Friction
Pull-out
Debonding
Matrix Crack
Tensile Stress (MPa)
Normalized AE Cumulative Hit Count (%)
Time (s)
0
30
60
90
120
150
180
0
10
20
30
40
50
0
20
40
60
80
AE Cumulative Hit Count (%)
Fiber Friction
Fiber Break
Pullout
Debonding
Matrix Crack
Total AE Energy (%)
Friction
Fiber Break
Pull-out
Debonding
Matrix Crack

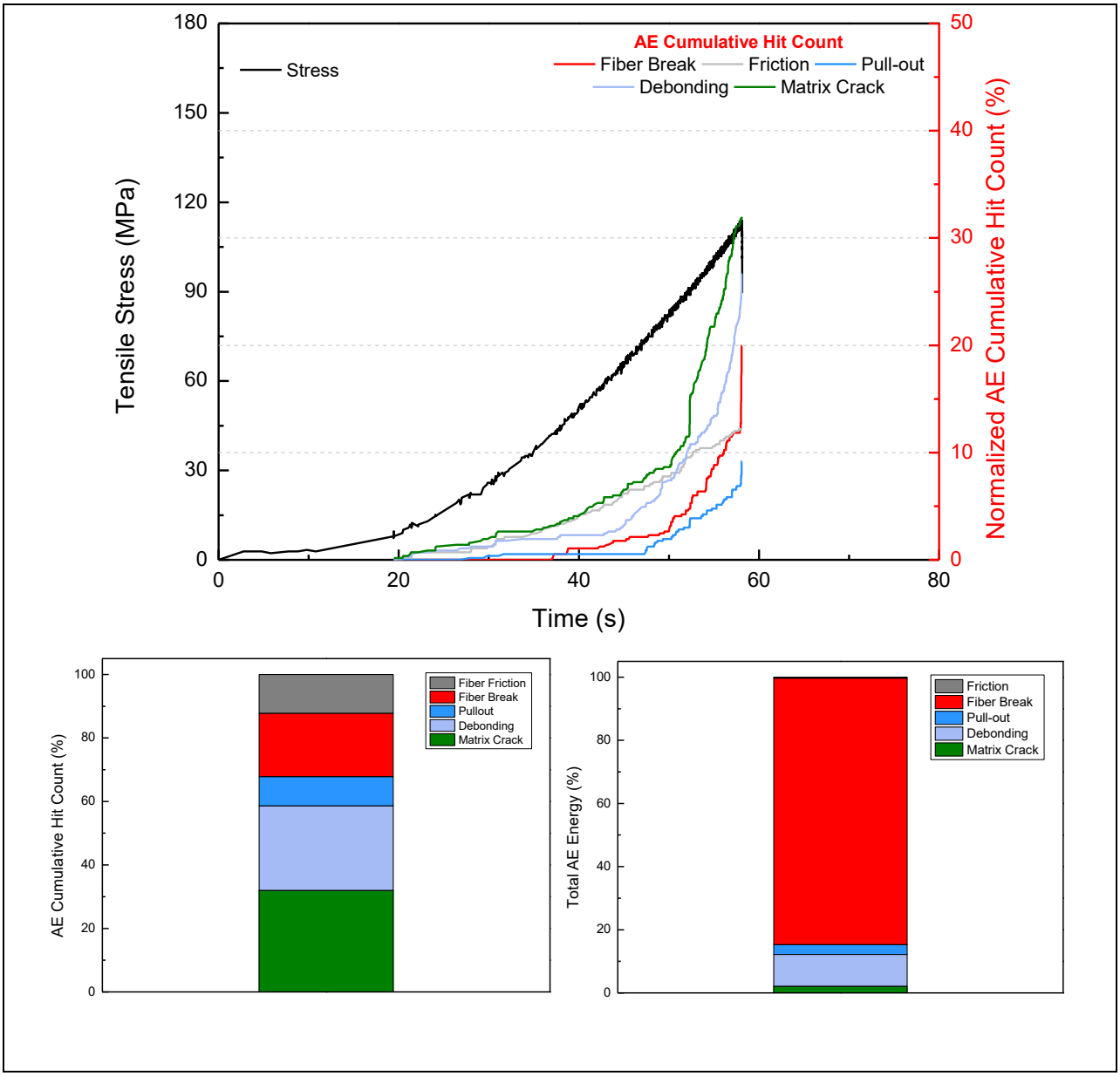
Stress
AE Cumulative Hit Count
Fiber Break
Friction
Pull-out
Debonding
Matrix Crack
Tensile Stress (MPa)
Normalized AE Cumulative Hit Count (%)
Time (s)
0
30
60
90
120
150
180
0
10
20
30
40
50
0
20
40
60
80
AE Cumulative Hit Count (%)
Fiber Friction
Fiber Break
Pullout
Debonding
Matrix Crack
Total AE Energy (%)
Friction
Fiber Break
Pull-out
Debonding
Matrix Crack

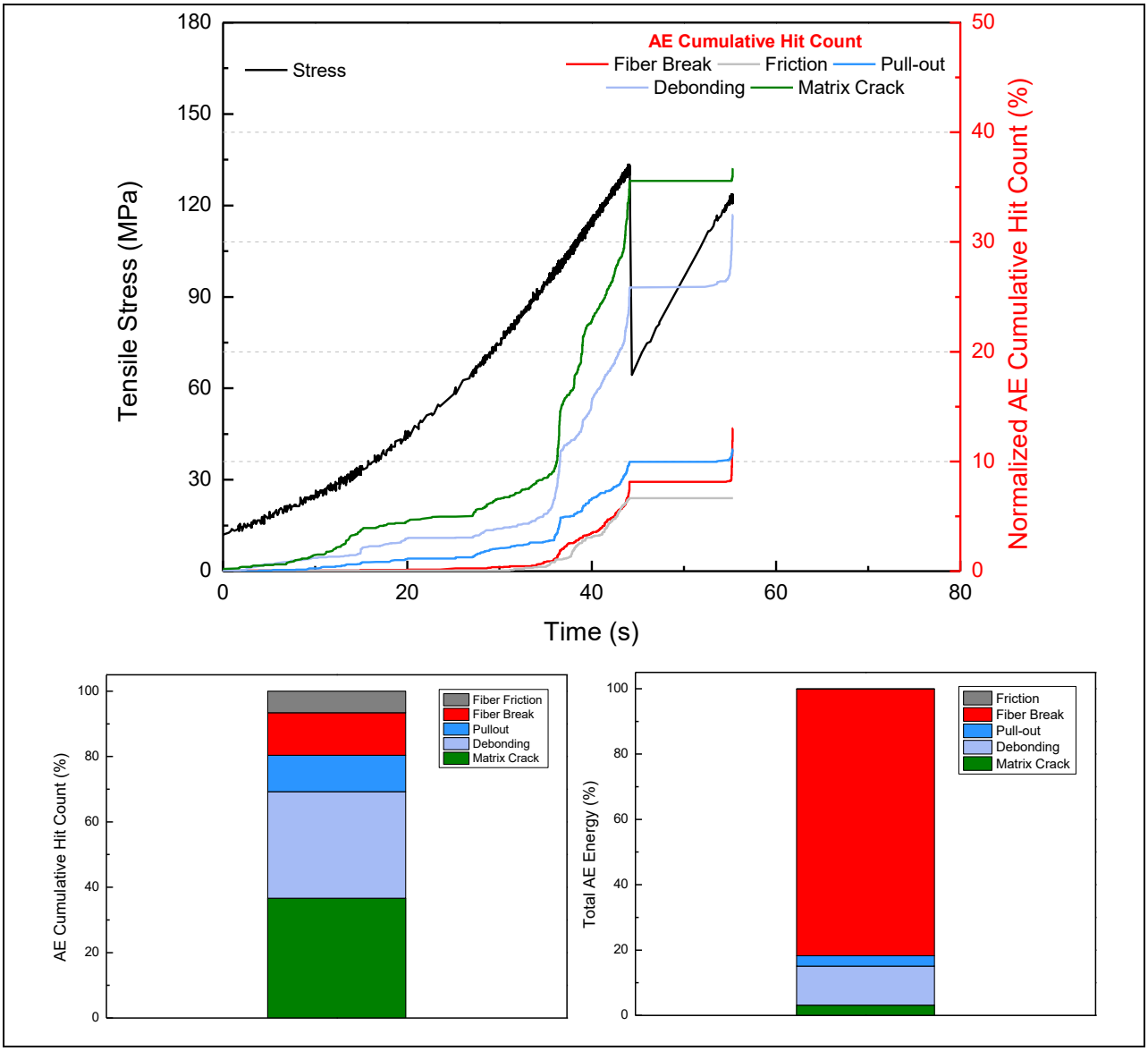

Source: author

Figure A4 – Selected Al_2O_{3f}/ Al_2O_3 composite plate plots, exhibited in the following order: Damage evolution, CHIT, and energy quantification for each signal.

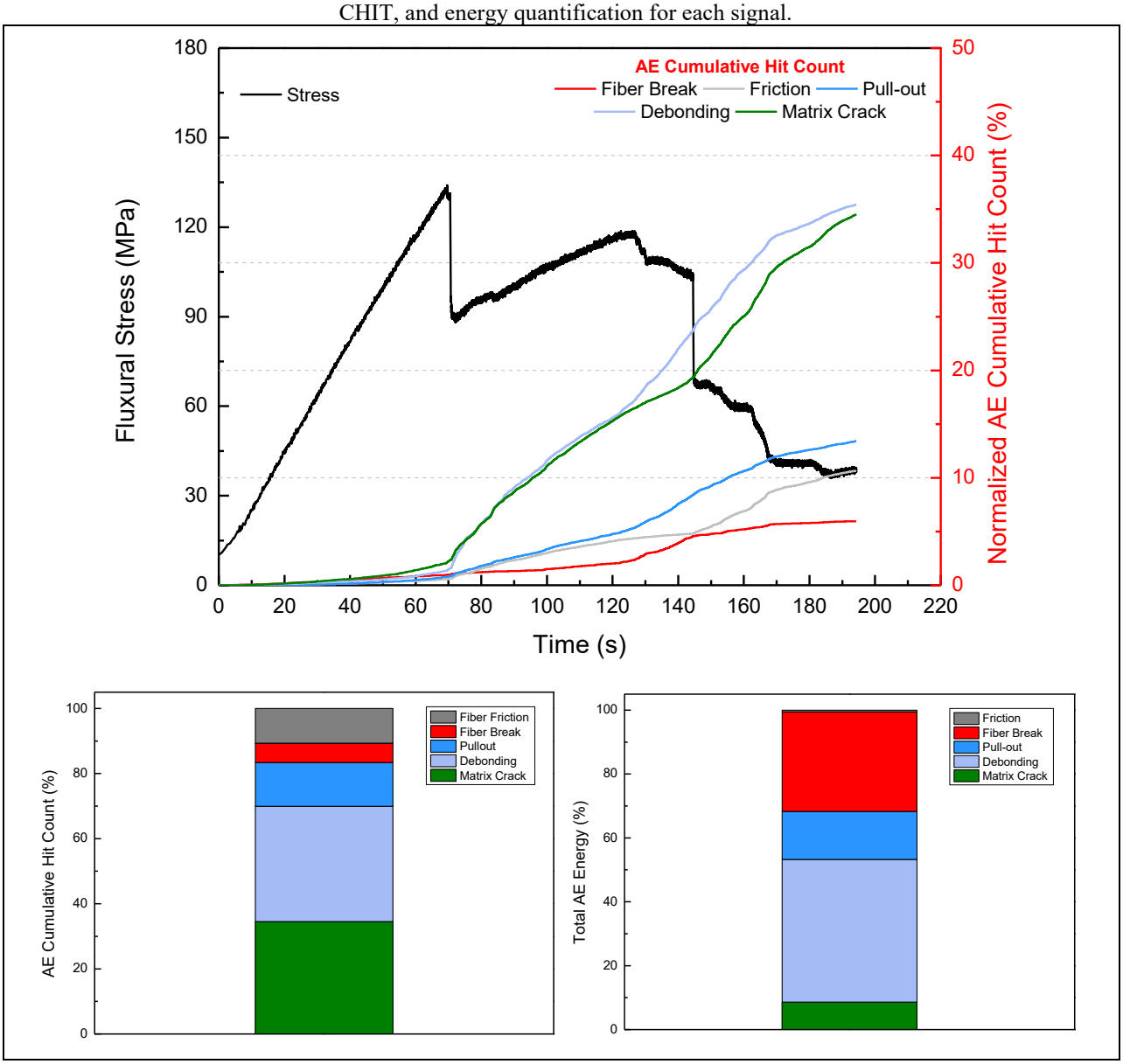

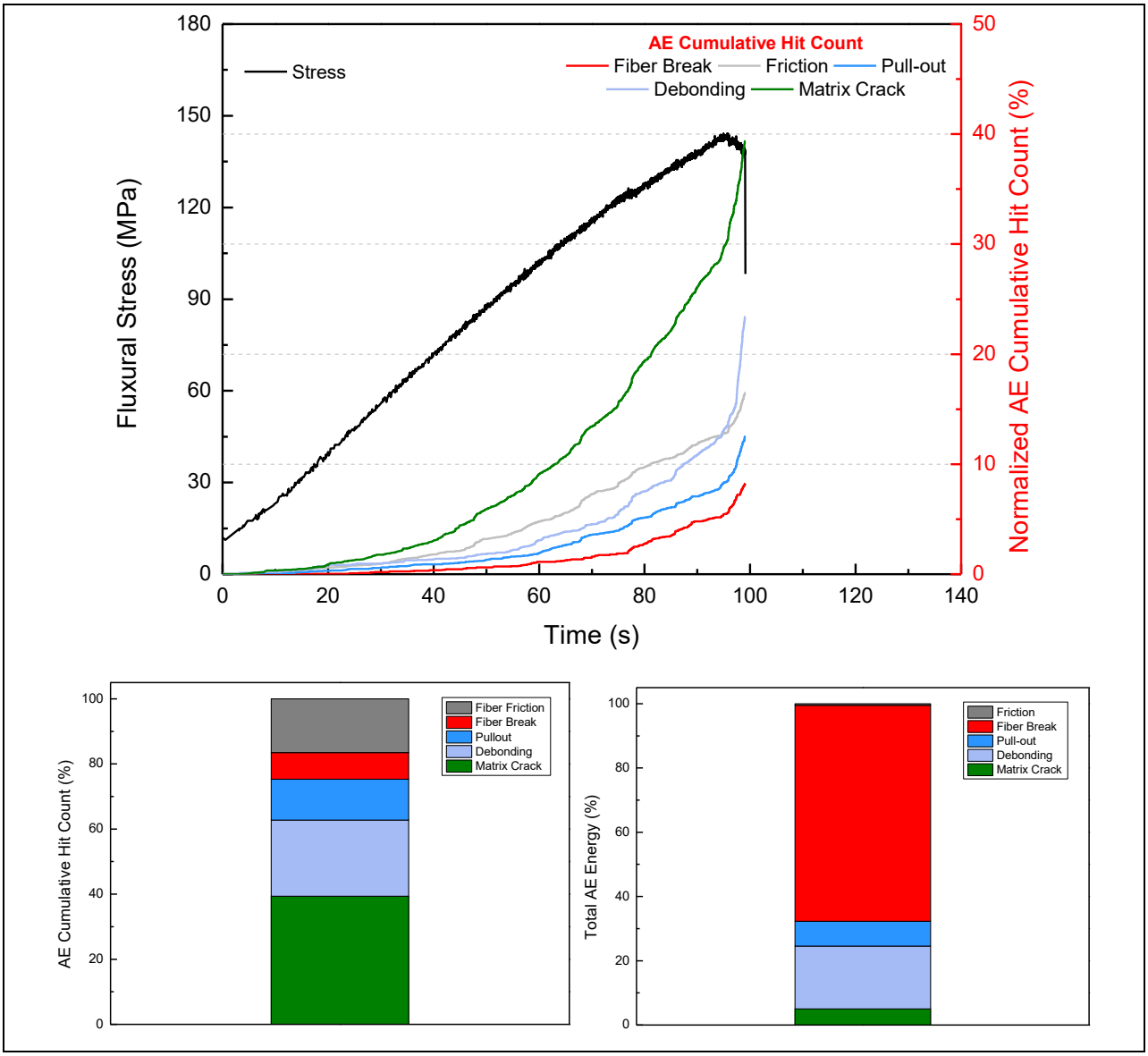
Fluxural Stress (MPa)
Normalized AE Cumulative Hit Count (%)
Time (s)
Stress
AE Cumulative Hit Count
Fiber Break
Friction
Pull-out
Debonding
Matrix Crack
AE Cumulative Hit Count (%)
Fiber Friction
Fiber Break
Pullout
Debonding
Matrix Crack
Total AE Energy (%)
Friction
Fiber Break
Pull-out
Debonding
Matrix Crack

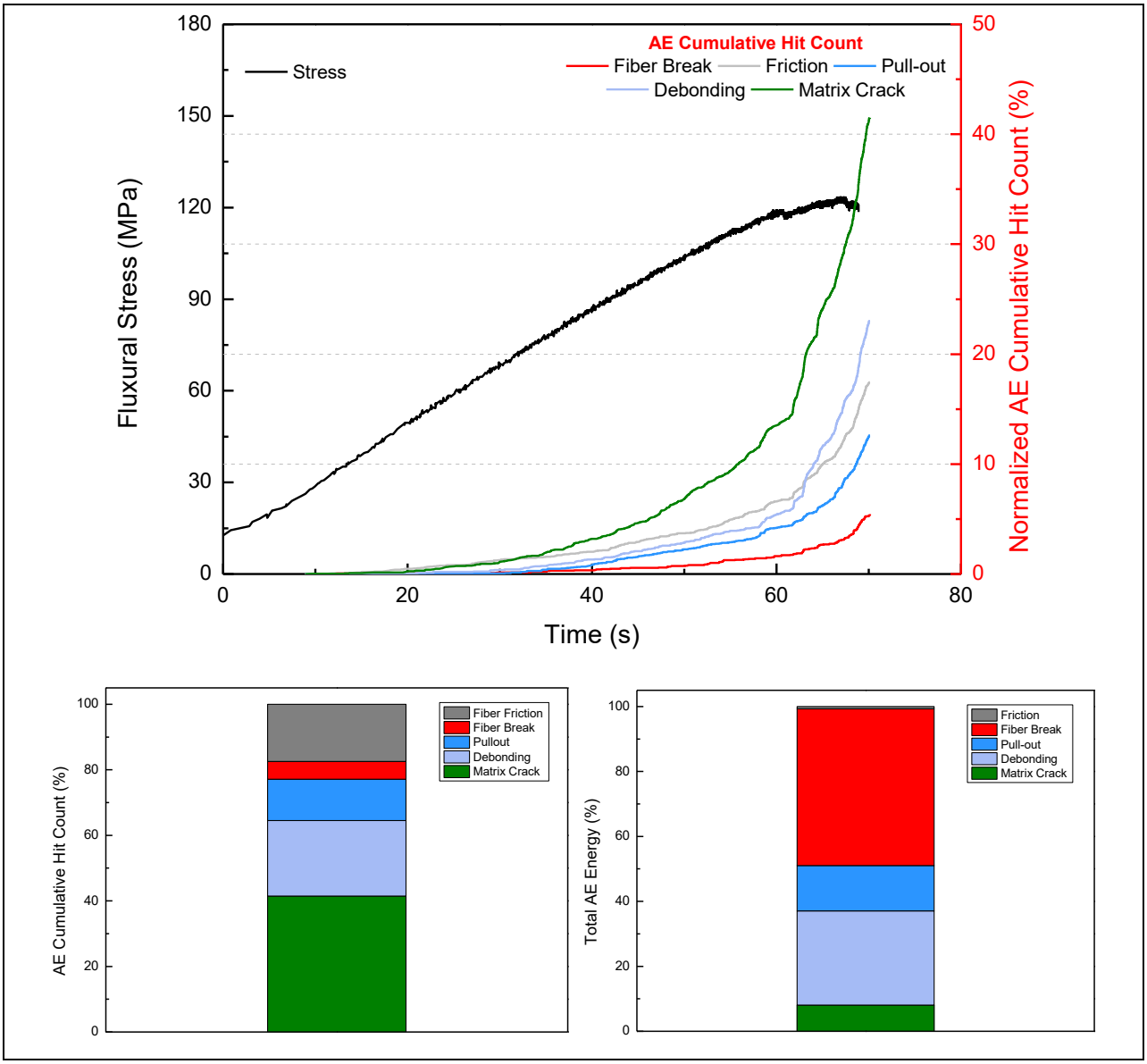
Stress
AE Cumulative Hit Count
Fiber Break
Friction
Pull-out
Debonding
Matrix Crack
Fluxural Stress (MPa)
Normalized AE Cumulative Hit Count (%)
Time (s)
0
30
60
90
120
150
180
0
10
20
30
40
50
0
20
40
60
80
AE Cumulative Hit Count (%)
Fiber Friction
Fiber Break
Pullout
Debonding
Matrix Crack
Total AE Energy (%)
Friction
Fiber Break
Pull-out
Debonding
Matrix Crack

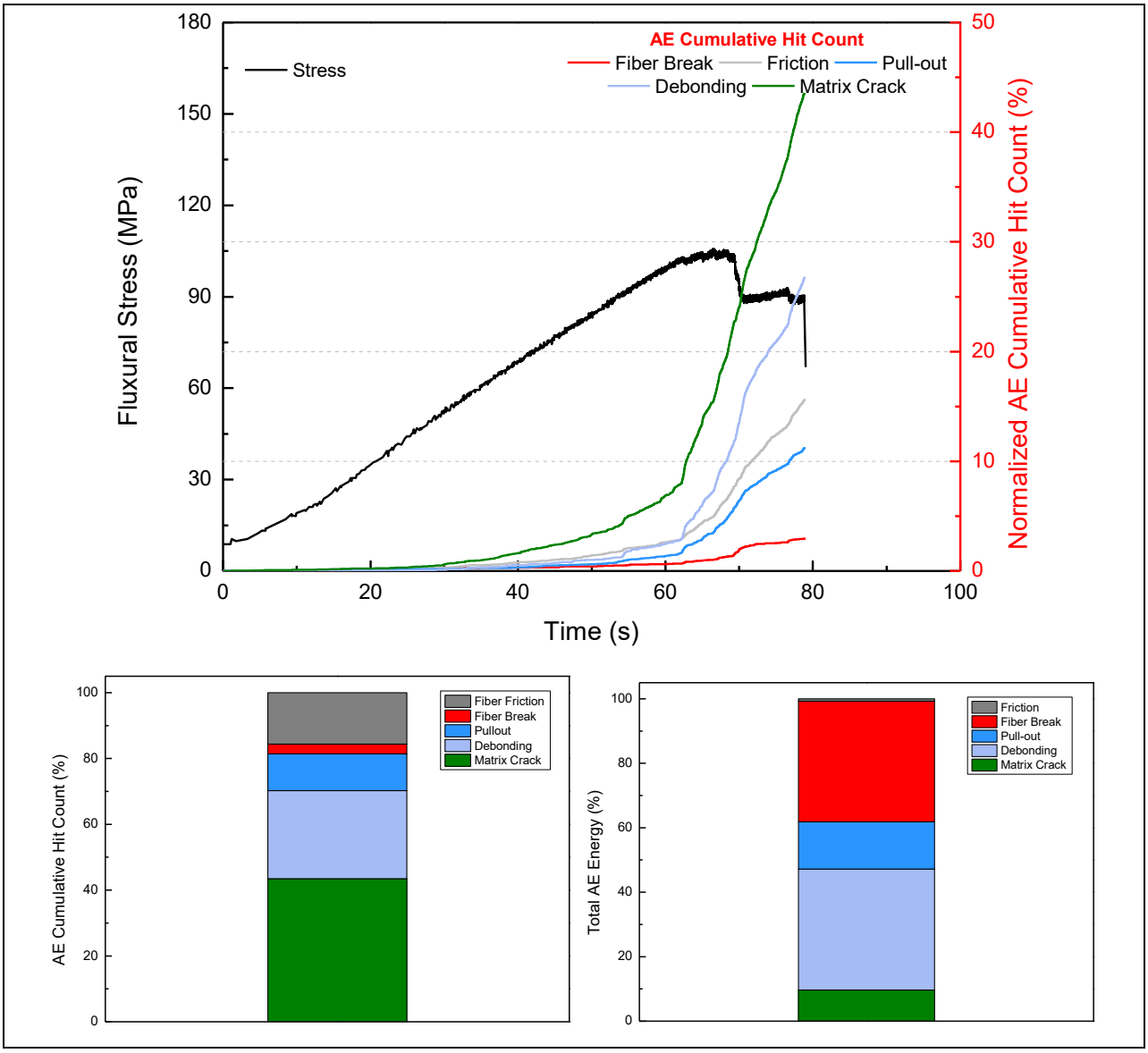

Source: author